Bio- and Environmental Sensing Based on Organic Optoelectronics

Dissertation

for the degree of Doctor of Engineering
(Dr.-Ing.)

Faculty of Engineering
Kiel University

by
Igor Titov

October 17, 2023

1st Referee: Prof. Dr.-Ing. Martina Gerken
2nd Referee: Prof. Dr.-Ing. Jan Trieschmann

Date of oral examination: September 6, 2023

Publications

I. Titov, N. Rutschke, F. A. Kraft, M. Köpke, E. Nebling, and M. Gerken, "Detection of fluorescence-labeled DNA with in-plane organic optoelectronic devices," Biomedical Optics Express, vol. 13, no. 12, p. 6300, Dec. 2022, doi: 10.1364/BOE.475358.

I. Titov, M. Köpke, and M. Gerken, "Monolithic Integrated OLED-OPD Unit for Point-of-Need Nitrite Sensing," Sensors, vol. 22, no. 3, p. 910, Jan. 2022, doi: 10.3390/s22030910.

I. Titov, M. Köpke, N. C. Schneidewind, J. Buhl, Y. Murat, and M. Gerken, "OLED-OPD Matrix for Sensing on a Single Flexible Substrate," IEEE Sensors Journal, vol. 20, no. 14, pp. 7540-7547, Jul. 2020, doi: 10.1109/JSEN.2020.-2986051.

S. Böckmann, I. Titov, and M. Gerken, "Extraction of Soil Solution into a Microfluidic Chip," AgriEngineering, 2021, doi: 10.3390/agriengineering3040049.

L. Holtorf, I. Titov, F. Daschner and M. Gerken, "UAV-Based Wireless Data Collection from Underground Sensor Nodes for Precision Agriculture," AgriEngineering, 2023, doi: 10.3390/agriengineering5010022.

I. Titov, M. Köpke, and M. Gerken, "Monolithic Integrated OLED-OPD Unit for Point-of-Need Nitrate Sensing," in Optical Sensors and Sensing Congress 2022 (AIS, LACSEA, Sensors, ES), Technical Digest Series (Optica Publishing Group, 2022), paper EW1G.1.

I. Titov, L. Holtorf, F. Daschner and M. Gerken, "Drone as LoRa Repeater for Readout of Low-power Sensor Nodes in Precision Agriculture," EASS 2022; 11th GMM-Symposium, 2022, pp. 1-3.

I. Titov, M. Köpke and M. Gerken, "Refractive Index Measurement with a Flexible OLED-OPD Detection Unit," 2020 IEEE International Conference on Flexible and Printable Sensors and Systems (FLEPS), 2020, pp. 1-3, doi:10.1109/FLEPS49123.2020.9239472.

Submitted Patent

M. Gerken, I. Titov, S. Böckmann, "Vorrichtung und Verfahren zur Extraktion von Wasser aus einer Bodenprobe", Priority 13.08.2021, German Patent submission DE102021121165A1 (13.08.2021).

Supervised Theses

Bachelor Thesis: "Optical pH-Sensor Based on a Fluorescence Dye in a Sol-Gel-Matrix", Thore Brüning, 2020.

Bachelor Thesis: "Automated System for Extracting Water from Soil into a Microfluidic", Sönke Böckmann, 2020.

Bachelor Thesis: "Fluorescence-Based Oxygen Measurement with an OLED-OPD Measurement System", Nicolas Alexander Lahl, 2022.

Master Thesis: "Light Guiding Plastic Substrate for Fluorescence Excitation with a Laser Diode", Lukas Gernoth, 2021.

Master Thesis: "Time-Resolved Fluorescence Detection of Europium(Eu) -Labelled Biomedical Substances Using Organic Photodetectors", Emre Abit Ficicilar, 2022.

Master Thesis: "Integrated, magnet-actuated valves for microfluidic sensor systems", Sönke Böckmann, 2023.

Master Thesis: "Modelling the wireless communication signal strength in an underground sensor network", Wajid Ali, 2023.

Acknowledgements

I would like to thank my doctoral supervisor Prof. Dr.-Ing. Martina Gerken, who helped me to find my path in the scientific world. Thank you for your excellent guidance, support and inspiration.

Special thank goes also to every single person of the Integrated Systems and Photonics group for numerous discussions, lunch- and coffee breaks, the enjoyable working atmosphere and many unforgettable memories.

My heartfelt thanks to my friends and my family - especially my parents - for their never ending support, love and sacrifices.

Finally, my deepest thanks to my sweetheart Vanessa for encouraging and supporting me in all phases of my life. Thank you for your patience during the long lean periods. I could not have done this without you!

We live in a society exquisitely dependent on science and technology, in which hardly anyone knows anything about science and technology. - Carl Sagan

Abstract

The integration of organic light emitting diodes (OLEDs) and organic photodetectors (OPDs) promises compact and low-cost hybrid integrated sensors for optical detection. The thermal evaporation-based device fabrication technique allows for all optical sensing elements being permanently aligned with a high degree of miniaturization, creating more portable, energy-efficient and multiplexing-capable devices; these may be easily combined with microfluidic units resulting in a minimal sample and reagent volume demand of the sensor. This dissertation deals in particular with the system design, development, characterization and deployment of a monolithic integrated sensor unit with 8 OLED and 8 OPD pixel pairs for different applications. The following work provides an extensive study of the system efficiency via ray tracing simulations, investigating crucial boundary conditions for efficient analyte detection. The proposed sensing unit contains OLED and OPD devices with an individual pixel size of 0.5 mm × 0.5 mm fabricated on a 12.5 mm × 12.5 mm glass substrate. The developed sensor system was successfully characterized and applied in a biosensing application by detecting fluorescence labelled single-stranded DNA (ssDNA) after forming the Förster resonance energy transfer (FRET) upon the hybridization of two ssDNA strands. This optoelectronic sensor has the potential to enable compact and low-cost fluorescence point-of-care (POC) devices for decentralised multiplex biomedical testing. Additionally, this sensing platform was deployed in environmental and agricultural applications to detect nutrients such as nitrite and nitrate. In this colorimetric application the popular Griess reaction was utilized to form the nitrite concentration dependent amount of azo dye, which absorbs light around 540 nm. The device shows a low limit of detection of 46 µg L^{-1} (1.0 µmol L^{-1}) and a linearity of 99%. To push the technology towards an optical microfluidic analysis system for in-situ chemical detection of nutrients in soil solution, a soil solution extraction unit was developed. This microfluidic unit presents the missing link between optical microfluidic analysis systems and the soil, and serves as the fundamental step towards resource-efficient and environmentally sustainable smart agriculture.

Zusammenfassung

Die hybride Integration von organischen Leuchtdioden (OLEDs) und organischen Photodetektoren (OPDs) ist vielversprechend für die Entwicklung einer kompakten und kostengünstigen Detektionseinheit für viele Anwendungsfelder. Die optoelektronischen Elemente werden mit Hilfe der thermischen Verdampfungstechnik hergestellt und erlauben aufgrund der permanenten Ausrichtung ein hohes Maß an Miniaturisierung und der Möglichkeit energieeffiziente Multiplex-Systeme zu entwickeln, die mit Mikrofluidikeinheiten kombiniert werden können. Diese Dissertation beschäftigt sich maßgeblich mit dem Systemdesign, Entwicklung, Charakterisierung und dem Einsatz der optischen Sensoren basierend auf monolithisch integrierten 8 OLED-OPD Pixelpaaren in mehreren Anwendungsgebieten. Das Systemdesign und die Effizienz werden mit Hilfe von Ray Tracing Simulationen untersucht, wobei die Parameter und Randbedingungen aus Literatur und eigenen experimentellen Arbeiten hinzugezogen werden. Die entwickelte Sensoreinheit mit insgesammt 8 OLED-OPD Paaren auf einem Chip wurde auf einem Glassubstrat der Größe $12.5\,\mathrm{mm} \times 12.5\,\mathrm{mm}$ prozessiert. Die einzelnen optoelektronischen Pixel haben dabei eine Größe von $0.5\,\mathrm{mm} \times 0.5\,\mathrm{mm}$. Die Sensoreinheit wurde im Rahmen der Dissertation erfolgreich in einer Biosensoranwendung eingesetzt. Dabei kamen fluoreszenzmarkierte Einzelstränge einer viralen DNA zum Einsatz. Der Nachweis erfolgte mit Hilfe der Hybridisierung des Einzelstranges mit einem Komplementärstrang und des daraus resultierenden Förster-Resonanzenergietransfers, was eine messbare Auslöschung der Fluoreszenz zur Folge hat. Der auf organischen Halbleitern basierte optoelektronische Sensor hat zweifellos das Potenzial, als eine kompakte und kostengünstige Point-of-Care (POC) Sensorplattform dezentrale biomedizische Multiplex-Tests zu ermöglichen. Der Sensor fand darüberhinaus auch den Einsatz in Umwelt- und Landwirtschaftsanwendungen. Hierbei wurde die bekannte Griess Reaktion für kolorimetrische Messungen von Nitrit und Nitrat eingesetzt. Die Griess Reaktion erzeugt unter Zugabe von Nitrit und weiteren chemischen Komponenten einen Azofarbstoff, der das Licht bei ca. 540 nm absorbiert. Dabei konnte eine Nachweisgrenze von $46\,\mu\mathrm{g\,L^{-1}}$ ($1.0\,\mu\mathrm{mol\,L^{-1}}$) mit einer Linearität von 99% gezeigt werden. Desweiteren wurde im Rahmen der Dissertation an einem mikrofluidischen Bodenlösungsextraktionssystem geforscht, welches das Bindeglied zwischen dem entwickelten OLED-OPD Chip und dem Einsatz auf einem land-

wirtschaftlich genutzen Acker darstellen soll. Es ist ein grundlegender nächster Schritt um den chemischen in-situ Nachweis von Nährstoffen im Boden zu ermöglichen, der das Potential mitbringt die konventionelle Landwirtschaft zu einer ressourcenschonenden und umweltverträglichen Landwirtschaft zu wandeln.

Declaration

I hereby declare that I have written this dissertation entitled

Bio- and Environmental Sensing Based on Organic Optoelectronics

independently and without improper external assistance and that I have identified all quotations of other authors. Furthermore, this thesis has not been, partially or completely, submitted to any other university or institute in the context of an examination procedure. Parts of the content of the work have already been published in my scientific publications and are stated accordingly. I declare that the following work has been written in compliance with the rules of good scientific practice established by the German Research Foundation. I also declare that an academic degree has never been withdrawn and no relevant grounds for this are present.

17.10.2023, Kiel

Date, Place

I. Titov

Igor Titov

Contents

Chapter 1

Introduction

1.1 Motivation, Specific Aims and Outline

The world's growing population is one of the major challenges for humanity in the current century. The Department of Economic and Social Affairs of the United Nations recently published a report which estimates the growth of the world's population to 9.7 billion people by 2050 and even 11 billion by the end of the century [1]. This increases dramatically the demand for generally accessible healthcare and biomedical diagnostic devices. Nowadays disease testing can be realised with the immunostaining or polymerase chain reaction (PCR) analysis after a virus isolation or by an enzyme-linked immunosorbent assay (ELISA). However, these pathogen detection techniques suffer from severe disadvantages: they are lab intensive and highly time consuming. To overcome the aforementioned limitations, lab-on-chip (LOC) systems for rapid point-of-care (POC) diagnosis are of particular interest. These are already widely applied in environmental monitoring, human and animal disease monitoring, food control, forensics, drug discovery and biomedical research applications [2, 3]. Probably the most prominent and widely available POC test for personal use is the lateral flow test, as used in pregnancy and SARS-CoV-2 tests. However, the demand for LOC devices is not only limited to human medical applications, but has several emerging trends in veterinary, environmental and agricultural applications as well.

Animal disease test devices for veterinarians have also a rapidly growing market; for example, one of the most pathogenic virus variants for horses is the equid herpesvirus (EHV). The variants have been reported in five types named EHV-1 to 5. They are responsible for neurological and respiratory diseases, abortions as well as equine herpesvirus myeloencephalopathy (EHM) [4]. Early

detection of EHV is hence crucial and can be realised via PCR or ELISA. EHV is transmitted by nose-to-nose contact or fomites. As a consequence, immediate separation of horses and strict quarantine are essential to contain EHV and prevent the closure of equine venues and equestrian farms. Thus, a rapid diagnosis is critical to avoid considerable economic costs to the owner or even the loss of an animal's life .

The aforementioned demand for LOC systems in environmental and agricultural applications is strongly related to the world's growing population as well. To ensure sustenance for all we will need much more efficient agriculture. The arable land will need to become much more profitable than it is today, with the need to increase production for the same amount of land by 60% [1]. To approach this problem farmers are deploying fertilizers on their fields. To give an example, nitrates and nitrites play an essential role for plant growth and root development. They are a major component of inorganic fertilizers, but the exceedance of limit values in ground water due to their high solubility is an urgent problem as it has many negative effects on animal and human health [5]. Thus, the detection of nitrite and nitrate in samples, such as soil solution or ground water, is essential for a resource-efficient and environmentally sustainable agriculture and has been reported by many different research groups [6]. The state of the art analysis of chemical soil parameters is today based on soil or soil solution sampling in the field and a subsequent analysis in the laboratory. However, the storage- and transport-based sample alteration and the time consumption is a great disadvantage. Hence, portable point-of-source (POS) soil-analysis systems are being developed [7–9]. To address the aforementioned problems the development of compact, low-cost and simple-to-fabricate POC/POS sensors is the prominent aim of this work. The hybrid integration of organic light emitting diodes (OLEDs) and organic photodetectors (OPDs) to optical detection units promises great potential for highly integrated biosensors. These detection units are based on the thermal evaporation (particular method of phsyical vapor deposition (PVD)) device fabrication technique, enabling a high degree of miniaturization and permanent alignment of optical elements. Figure 1.1 provides an overview of the work included in this dissertation and illustrates the developed OLED-OPD sensor unit applied to three main research areas: biosensing, environmental sensing and nutrient sensing. The eight OLED and OPD pairs are successfully monolithically integrated and have an individual device size of 0.5 mm × 0.5 mm each. The gap between the devices is 0.9 mm. Due to the monolithic integration and a

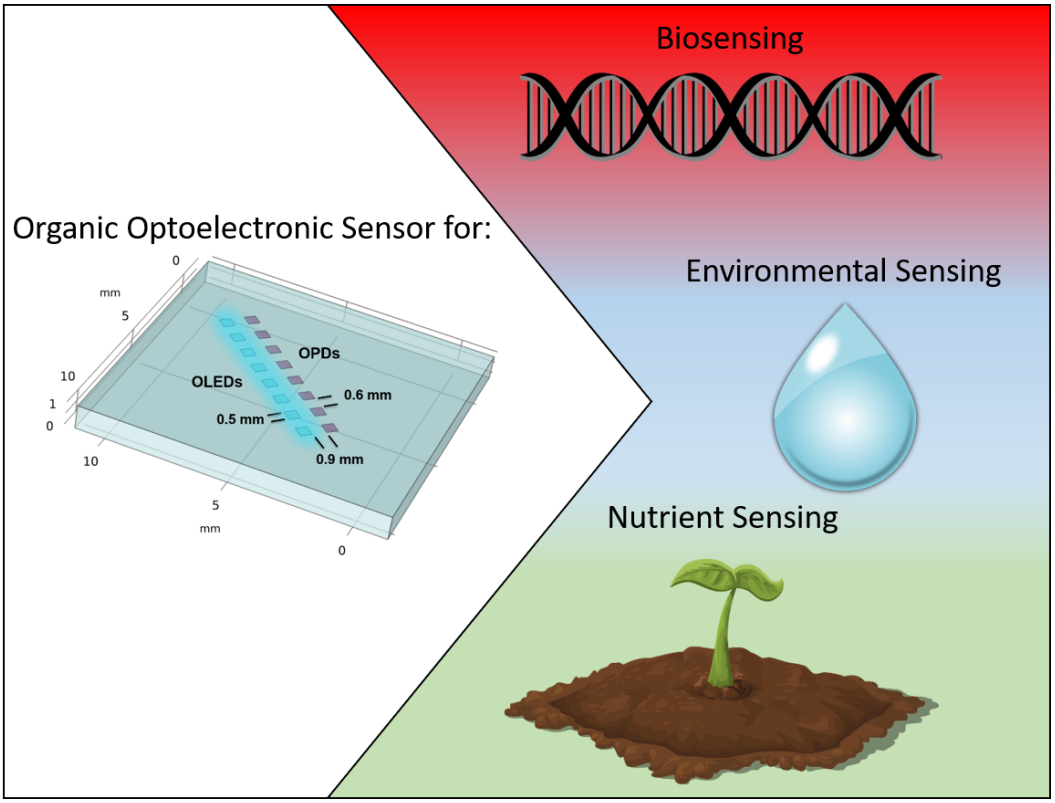

Figure 1.1: Model of the investigated OLED-OPD chip and the promoted applications in this work.

simple fabrication process, the scalability of parallelly fabricated sensor units is promising, leading to low cost and potentially disposable POC systems [10]. In this work two different transducer techniques were applied to obtain the desired signal on the OLED-OPD unit. For the biomedical application part the steady-state fluorescence measurement technique was utilized. For the environmental and nutrients sensing part the absorption measurement technique was applied. To verify the experimental results and propose improvements for future work, the thesis contains an estimation of the OLED-OPD system efficiency by performing ray tracing simulations.

This dissertation is structured as follows. Chapter 1 provides a brief insight into the motivation of the work and addresses emerging needs of POC sensors in biomedical, environmental and agricultural applications. The aim is to guide the reader's attention to these emerging needs considering the world's growing population and the demand for new analytical detection tools. Chapter 2 presents the fundamental theory, which is essential to understand this thesis. Chapter 3 gives an example of optical state-of-the-art sensors based on organic optoelectronic devices. Chapter 4 is the main part of the thesis and consist of four peer-reviewed publications. The first publication deals with an

OLED-OPD detection unit for fluorescence quenching of surface bound fluorescence labeled ssDNA strands used as capture molecules. The paper shows successfully performed DNA hybridization sensing by utilizing Förster Resonance Energy Transfer (FRET). Additionally, the paper contains all relevant information about the fabrication, the characterization and the system efficiency analysis by performing ray tracing simulations with COMSOL Multiphysics. The second paper deals with a similar OLED-OPD unit, but modified OLED emitter materials suitable for POC nitrite sensing. The presented detection method is the popular colorimetric Griess reaction and a subsequent absorption measurement of the OLED light. The third paper presents an OLED-OPD matrix fabricated on a flexible substrate, which has been proposed for wearable applications. The work contains a ray tracing simulation chapter, which was performed to find the optimal geometrical design parameter for the sensing unit and an evaluation of stray light influence for transparent and black absorptive microfluidics. The fourth publication shows a soil solution extraction unit, designed and fabricated for further integration with a sensing unit for measuring of chemical parameters inside the soil. This unit is a combination of a polydimethyldisiloxane (PDMS) fluidic and a highly porous ceramic filter unit in the inlet for soil solution sampling. The results show successfully extracted soil solution, which serves as a promising preliminary work towards a fully integrated and autonomous soil nutrients sensor and presents the missing link between optical microfluidic analysis systems from previous publications and the soil. Finally, chapter 5 summarizes this dissertation and proposes an outlook on future research related to this work.

Chapter 2

Fundamentals

Optical sensors convert electromagnetic radiation into electrical current. These devices can operate within the range between infrared and ultraviolet (UV) wavelengths. Besides electrochemical sensing, optical sensing is the most common technique for the detection of certain parameters in biomedical, healthcare, environmental and agricultural applications [11–13]. These parameters can be e.g. fluorescence labeled biomarkers in animal or human body fluids, pulse-oximeter measurements with wearables, nitrite (NO_2^-) or nitrate (NO_3^-) and other nutrients, which strongly affect plant growth in agricultural applications.

From a technical point of view, the primary function of an optical sensor is to emit light on a transducer and detect the output signal. The most common light sources integrated in state-of-the-art devices are light emitting diodes (LEDs), laser sources and halogen or flash lamps. The light detection can be realised with charge-coupled cameras (CCD), spectrometers, photomultiplier tubes (PMTs) and photodiodes (PDs). In this work organic light-emitting diodes (OLEDs) and organic photodetectors (OPDs) were utilized as a light source and the detector, respectively. The following sections provide information about the fundamentals of optical fluorescence sensors, i.e. the fluorescence phenomenon and the detection strategies, the relevant spectrophotometric transducer techniques, a short introduction in organic optoelectronic devices and provide an insight into the ray tracing modelling algorithm of COMSOL Multiphysics, that form the core matter of this work.

2.1 Principles of Optical Fluorescence Sensors

2.1.1 Fluorescence Phenomenon

Fluorescence detection is one of the most well-established transducer techniques for the analytical detection in medical and environmental applications, such as medical diagnosis, DNA sequencing, oxygen or pH-level measurements, to name a few [14–16]. In the last decades fluorescence spectroscopy and time-resolved fluorescence have emerged as the most common detection methods. In general, fluorescence is a part of luminescence and describes the emission of light from a certain form of matter after the absorption of photons, also called excitation.

The processes of fluorescence can be illustrated by the Jablonski diagram in Figure 2.1(a) according to [17]. The ground, first and second electronic states are shown as S_0, S_1 and S_2, respectively. In these electronic states the electrons can exist on a number of vibrational energy levels, shown as 0, 1, 2, 3, etc. The absorption of a photon results in a transition of an electron from the ground state S_0 to an excited state (S_n with n $>$ 0) corresponding to a higher vibrational energy level. This transition occurs in about 10^{-15} s. Within the next approx. 10^{-12} s or less, the molecule relaxes non-radiatively to the lowest vibrational energy level of S_1. This process is called internal conversion. Finally, the electron returns to the singlet ground state S_0 with a photon emission and thus to a lower energy than initially absorbed for the transition, i.e. the fluorescence has a longer wavelength than the excitation light. Figure 2.1(b) shows the absorption spectrum of an fluorescein derivative dye and the emission spectrum of the fluorescence with a longer wavelength. This effect is called Stokes shift. Molecules can also undergo a spin conversion to the first triplet state T_1, which is referred to as intersystem crossing (ISC). The transition from T_1 to S_0 is forbidden since the electron in the excited orbital has the same spin orientation as the ground-state electron. The emission rate constants are orders of magnitude smaller than for fluorescence and are generally shifted to longer wavelengths compared to fluorescence. This emission from triplet excited states is called phosphorescence.

2.1.2 Förster Resonance Energy Transfer

Förster resonance energy transfer or sometimes also called fluorescence resonance energy transfer is a detection technique, which is widely used in med-

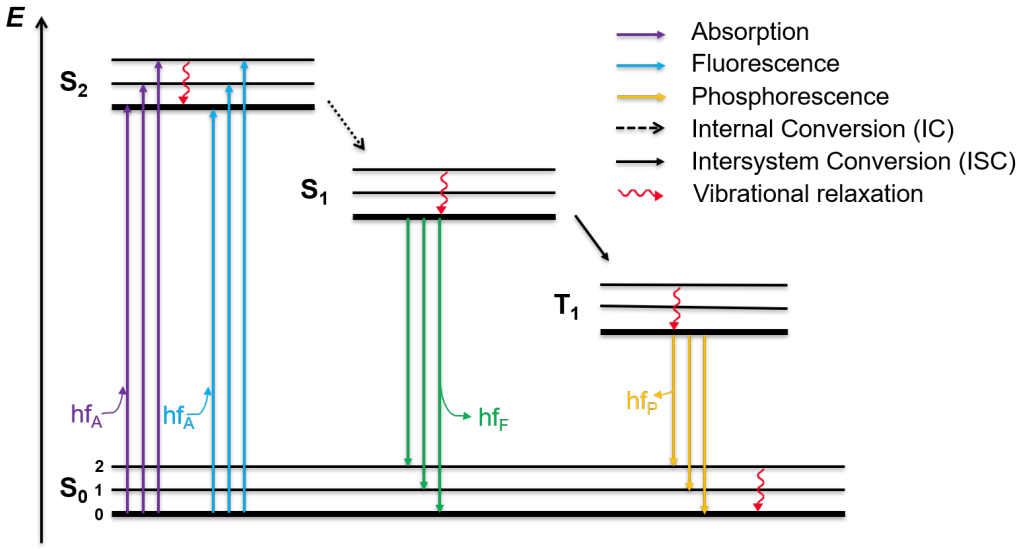

(a) One form of a Jablonski diagram describes the energy transfer between several electronic states of a molecule. The ground, first and second electronic states are shown as S_0, S_1 and S_2, respectively. On each electronic state a number of vibrational energy levels can exist, shown as 0, 1 and 2.

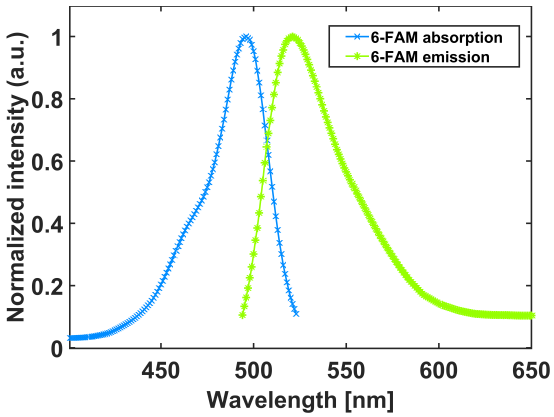

(b) Stokes shift of a fluorescein derivate dye 6-FAM [18].

Figure 2.1: Illustration of the fluorescence process and an example for the Stokes shift phenomenon.

ical diagnosis, DNA analysis and optical imaging. Prof. Joseph R. Lakowicz describes in his book [17] FRET as a phenomenon, where two different fluorophores with an overlap of the emission and excitation spectra undergo an energy transfer without the appearance of a photon. This is a result of long-range dipole-dipole interactions between the donor fluorophore and the acceptor fluorophore. Figure 2.2 shows an example of FRET with the spectra of Cy3 and Cy5 dye. Cy3 acts as the donor fluorophore, absorbing light around 488 nm and emitting around 532 nm. Cy5 has an absorption peak at approx.

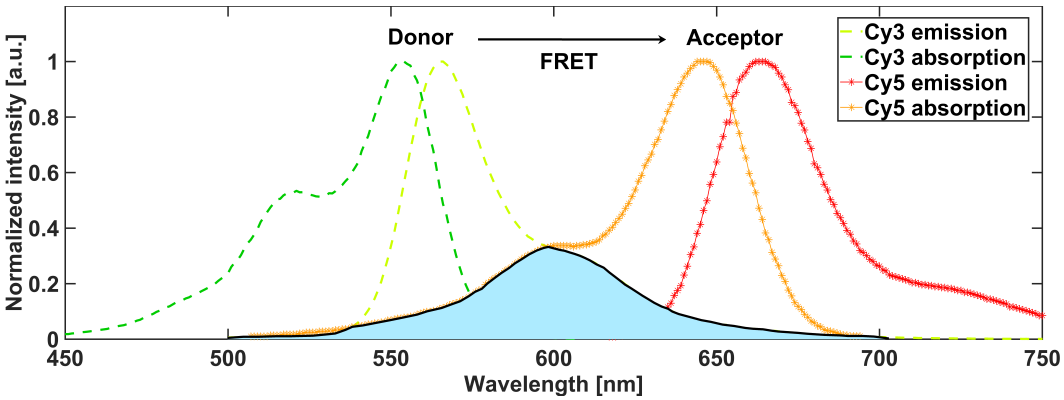

Figure 2.2: Förster Resonance Energy Transfer (FRET) example with Cy3 as the donor and Cy5 as the acceptor fluorophore [18].

633 nm, an emission peak around 647 nm and acts as the acceptor dye. The plot shows the spectral overlap of the Cy3 emission and the Cy5 excitation as the blue filled intersection area, which enables energy transfer between both molecules without a photon emission. The efficiency of FRET is dependent on the spectral properties of the fluorophores, the quantum yield of the donor, the relative orientation of the donor and acceptors transition dipoles and the distance of the donor and acceptor molecule.

The distance at which 50% FRET efficiency can be observed is called the Förster distance and is typically in the range of 2 to 6 nm. This distance is of the order of protein sizes and thus, utilization of FRET is a favorable detection technique for biomedical applications. One of FRET's most common applications is DNA hybridization sensing. Here, two individually labeled complementary ssDNA sequences with donor, respectively acceptor fluorophores are used [3, 19]. The FRET occurs after the hybridization to double-stranded DNA (dsDNA), when fluorophore molecules come into proximity. The effect of molecule distance on the rate of FRET can be described by [17]

$$k_\tau(r) = \frac{1}{\tau_D}\left(\frac{R_0}{r}\right)^6, \tag{2.1}$$

where τ_D is the decay time from the donor fluorophore in the absence of the acceptor, R_0 is the Förster distance and r is the distance between the donor and acceptor molecule. Consequently, the FRET rate coincides with the inverse of the decay time $\frac{1}{\tau_D}$ when the molecule distance equals the FRET distance R_0. The FRET rate strongly depends on the distance and is proportional to r^{-6}.

2.1.3 Steady-State Fluorometry

Steady-state fluorescence measurements are performed with constant illumination and observation. The sample is usually excited with a continuous light beam and the spontaneous emission is recorded simultaneously. Since most fluorescence indicators decay on a nanosecond timescale, the steady-state detection technique is most commonly employed [17]. In addition the decrease or increase of the fluorescence intensity is widely studied and gives information about (bio-)chemical systems. This effect is also called fluorescence quenching and represents a fundamental part of steady-state measurements. Fluorescence quenching can result out of different molecular interactions such as excited-state reactions, molecular rearrangements, energy transfer, ground-state complex formation and collisional quenching. Collisional quenching or dynamic quenching is one of the most popular effects as for example molecular oxygen quenches almost all known fluorophores. The molecular contact between the fluorophore and the quencher molecule results in the return of the fluorophore to the ground state without emission of a photon and thus provides a measurable intensity decrease. The fluorophore is usually embedded in a porous polymer film to immobilize the indicator and protect the dye from leaching, while working with fluids. The porosity of the matrix plays an important role. It controls the diffusion coefficient of the analyte gas and thus determines the sensitivity and response time of the sensor [20,21]. The schematic in Figure 2.3

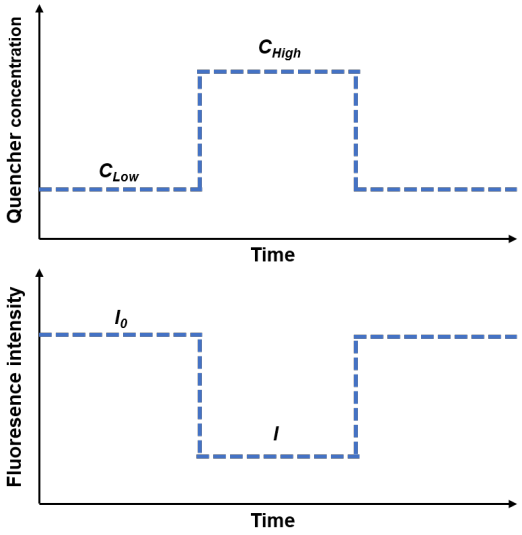

Figure 2.3: Principle of the quencher detection mechanism. The change in fluorescence intensity can be related to the quencher concentration and evaluated as the sensor signal.

shows the principle of fluorescence quenching sensing. The fluorescence signal intensity can be reversibly quenched under exposure of quencher molecules, such as oxygen. It can be seen, that the intensity I_0 decreases to I for a high quencher concentration C_{High} and vice versa. This quenching process is described by the Stern-Volmer Equation [17]:

$$\frac{I_0}{I} = \frac{\tau_0}{\tau} = 1 + K_{SV}[C] = 1 + k_q \tau_0 [C] \tag{2.2}$$

where I_0 and I are the intensities in the absence and presence of the quencher, respectively, τ_0 and τ the decay time in the absence and presence of the quencher, K_{SV} is the Stern-Volmer constant, C is the quencher concentration and k_q is the bimolecular quenching constant, which is related to the gas diffusion coefficient in the polymer matrix [22].

2.1.4 Time-Resolved Fluorometry

Time-resolved fluorometry can be divided in two different classes: the time domain (or pulse modulation) and frequency domain (or phase modulation) fluorometry. Both are widely used in fluorescence spectroscopy studies of bi-

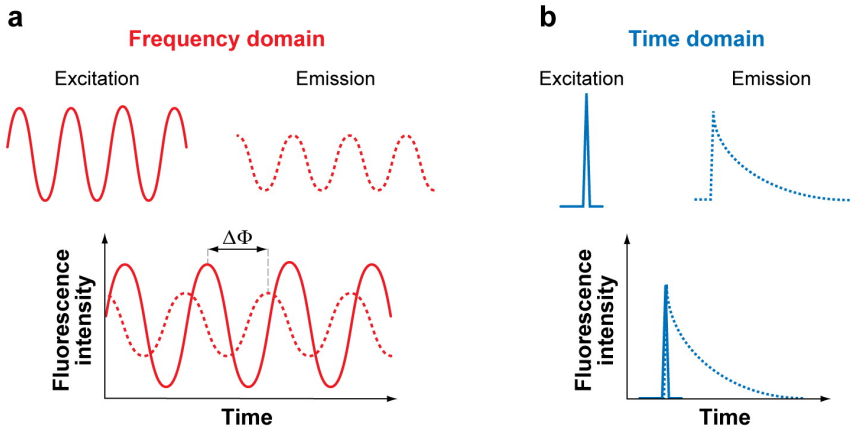

Wang Y, et al. 2008.
Annu. Rev. Biomed. Eng. 10:1–38.

Figure 2.4: Principles of fluorescence lifetime measurement. (a) Frequency domain or phase modulation: The phase-shift between the sinusoidal modulated excitation and emission light is used to calculate the lifetime of the fluorescence probe. (b) Time domain or pulse modulation: The captured decay time of the fluorescence emission after the excitation with a short light pulse is used to calculate the decay time. Reproduced with permission. [23] Copyright 2008, Annual Review of Biomedical Engineering.

ological macro-molecules or cellular imaging. One of the major advantages of

time-resolved measurements over the steady-state approach is the ability to distinguish excitation and emission spectra with a spectral overlap or a very small wavelength shift. The time-resolved data may reveal two decay times, which can be assigned to the excitation and the emission source, respectively. Figure 2.4 (a,b) shows both modulation techniques. The frequency domain method uses typically a sine-wave modulation of the excitation light. Due to the longer lifetime of the fluorophores emission, the signal appears to be delayed in time relative to the excitation and results as a phase shift $\Delta\Phi$, which can be employed for the calculation of the decay time. Additionally, the modulation information of the wave can also be used. In summary, the decay times can be calculated according to [24]

$$\tau_\Phi = \frac{\tan(\Phi)}{\omega} \qquad \text{and} \qquad \tau_m = \frac{1}{\omega}\left[\frac{1}{m^2} - 1\right]^{1/2}, \tag{2.3}$$

where m is the demodulation factor and ω the angular frequency. The pulse modulation uses a short light pulse for the excitation of a fluorophore, followed by a subsequent measurement of the emission decay time τ. The intensity of the fluorescence emission decreases to $1/e$ at $t = 0$. The exponential decay can be written with the expression

$$I(t) = I_0 \exp(-t/\tau) \tag{2.4}$$

where $I(0)$ is the intensity at time 0, τ is the fluorescence lifetime corresponding to inverse of the total decay rate of the excited-state, $\Gamma + k_{nr}$, with the emissive rate Γ and the non-radiative decay rate k_{nr} [17, 24].

2.2 Spectrophotometric Detection Technique

2.2.1 Lambert-Beer Law

Absorption followed by a radiative or non-radiative process, is a fundamental aspect of optical spectroscopy. The measurement of light absorption is also widely used for gas sensing (particularly infrared spectra), medical diagnosis or environmental sensing. The Lambert-Beer law can predict the optical density of matter and is given by [26]

$$\text{optical density } (OD) = \log \frac{I_0}{I} = \epsilon c d, \tag{2.5}$$

where I_0 is the intensity of the excitation light, I the intensity of the transmitted light, ϵ the decadic molar extinction coefficient (M^{-1} cm^{-1}), c the molar

concentration and d length of the optical path trough the sample. The optical density (OD) is equal to the absorbance (A) of a material in the absence of turbidity and is related to the transmission (T) as described in [26]

$$A = \log \frac{1}{T} = \log \frac{I_0}{I} = \epsilon c d. \tag{2.6}$$

Hence, A is directly proportional to the concentration of the absorbing medium. One of the most common errors in fluorescence spectroscopy is a too highly concentrated sample, where the excitation light gets mostly absorbed at the surface facing the light source and the right-angle measurements have a very low signal. Also the impurity of the sample or the turbidity of biological samples may cause light scattering proportional to $\frac{1}{\lambda^4}$ (Rayleigh scattering). This background absorption significantly increases with decreasing wavelength [17, 25, 26].

2.2.2 Sensing of Nitrite and Nitrate

The most prevalent techniques for detecting ions in liquid samples are electrochemical methods (voltametric, potentiometric and impedimetric electrodes), spectrophotometry, spectrofluorometry and ion chromatography [27–31]. Spectrophotometry is the most common method for nitrite and nitrate detection due to its simple procedure, low detection limits, high selectivity and low cost. In this work the popular Griess method [32] was utilized to form an azo dye after the reaction of reagents with nitrite ions, which strongly absorbs light around 540 nm [33].

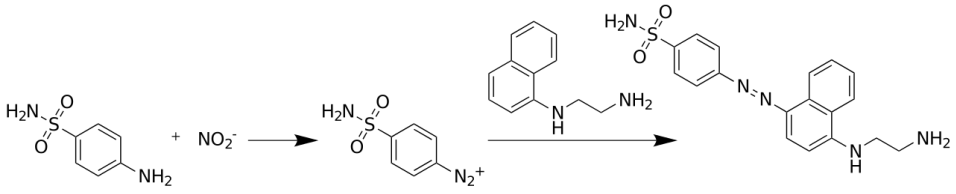

Figure 2.5: Schematic of the Griess reaction for spectrophotometric quantification of nitrite concentration.

Figure 2.5 shows the chemical transformation of sulfanilamide and N-(1-naphthyl)ethylenediamine dihydrochloride (NED) in an acidic solution. Sulfanilamide reacts in the first step with nitrite ion and forms diazonium salt. The azo dye formation occurs in the second step after the addition of NED. The resulting absorbance around 540 nm strongly depends on the initial nitrite concentration [10]. The detection of nitrate can be also implemented by

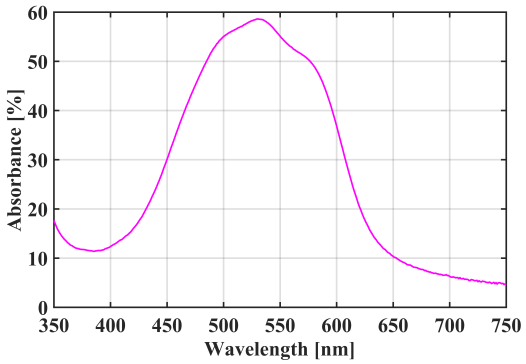

(a) Absorption spectrum of the azo dye.

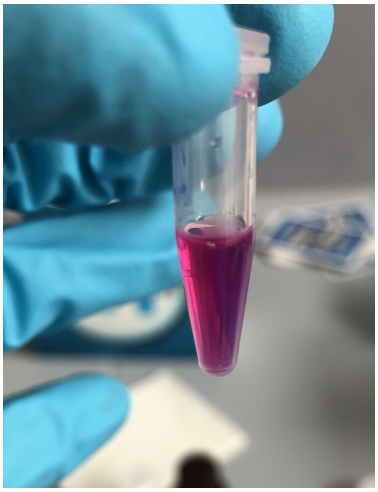

(b) Azo dye formation after adding a nitrite standard sample of 30 mg/l.

Figure 2.6: An example of the strong light absorbance around 540 nm of a Griess reaction based azo dye.

utilizing the same reaction with preceding reduction of nitrate (NO_3-) to nitrite (NO_2-), e.g. via the enzyme Nitrate reductase. Figure 2.6(a,b) shows an example of the Griess method resulting azo dye formation for nitrite determination. The Absorbance A of the light can be predicted with the described Lambert-Beer Law.

2.3 Organic Optoelectronics

Organic optoelectronic devices are widely used in modern smartphone displays and TVs. Also devices such as organic photodetectors or solar cells received considerable attention. This relatively young technology [34] promises particularly for biomedical lab-on-chip applications many advantages over their inorganic counterparts. Organic optoelectronic devices can be fabricated at moderate or room temperature, while inorganic LEDs require epitaxial growth process with high temperatures [19]. However, organic materials based on π-conjugated molecules with an amorphous morphology can be fabricated by thermal evaporation-based technique, allowing all sensing elements be permanently aligned with a high degree of miniaturization. Conductive polymers can be even printed, spin-coated or processed by large-scale roll-to-roll technique [35]. The hybrid integration of organic light-emitting diodes (OLEDs) and organic photodetectors (OPDs) can be applied in highly integrated point-

of-care (POC) devices and be processed on flexible or rigid substrates. Such devices have been already proposed as wearable sensors for health monitoring and other POC analysis applications [36–41]. These units can be easily laminated to a microfluidic system for sensing applications in a liquid [42–45]. The following chapters present an overview of the essential concepts of OLEDs and OPDs.

2.3.1 Organic Light Emitting Diodes (OLEDs)

After the first demonstration of Organic Light Emitting Diodes (OLEDs) in 1987 [34], organic optoelectronic devices gained strongly in popularity. Figure 2.7(a) shows a schematic of a simplified working principle of an OLED. The devices can be fabricated on rigid or flexible substrates, such as glass or plastics, and consist of a stack of organic layers sandwiched between a semi-transparent anode (e.g. Indium Tin Oxide (ITO)) and a metal cathode (e.g. Aluminum (Al)). The semi-transparent anodes are mostly deposited by sputtering directly onto the substrate. In the next sequence, organic layers are built up by thermal evaporation on top of the anode. The cathode consists mostly out of a low-work function metal and gets also evaporated on top of the sandwich structure. Finally, the emission of light occurs after voltage between the electrodes is applied. The efficiency and the emission wavelength can be influenced by tuning the layer thicknesses and changing the organic materials. Figure 2.7(b) shows a simplified illustration of the recombination process in the OLEDs heterojunction system. The Highest Occupied Molecular Orbital (HOMO) and the Lowest Unoccupied Molecular Orbital (LUMO) are shown. Applying voltage to the device results in the injection of electrons and holes through the cathode and the anode into the organic layer, respectively. Due to the electric field, the carriers can migrate through the organic layers towards each other and form an exciton. The exciton can decay after a short time under emission of a photon. Thus, the four most elementary steps of OLED operation are the charge injection, the charge transport, the exciton formation and finally the radiative decay [46]. However, real devices contain many more layers than the simplified model shows. The organic layers usually consist of an electron blocking layer (EBL) and a hole blocking layer (HBL), an emission layer (EML), an electron transport layer (ETL) and a hole transport layer (HTL). These are crucial for optimum electron or hole mobilities for reducing the ohmic losses, to block electrons and holes, and prevent the extraction of charge carriers through the electrodes without forming an exciton. Addition-

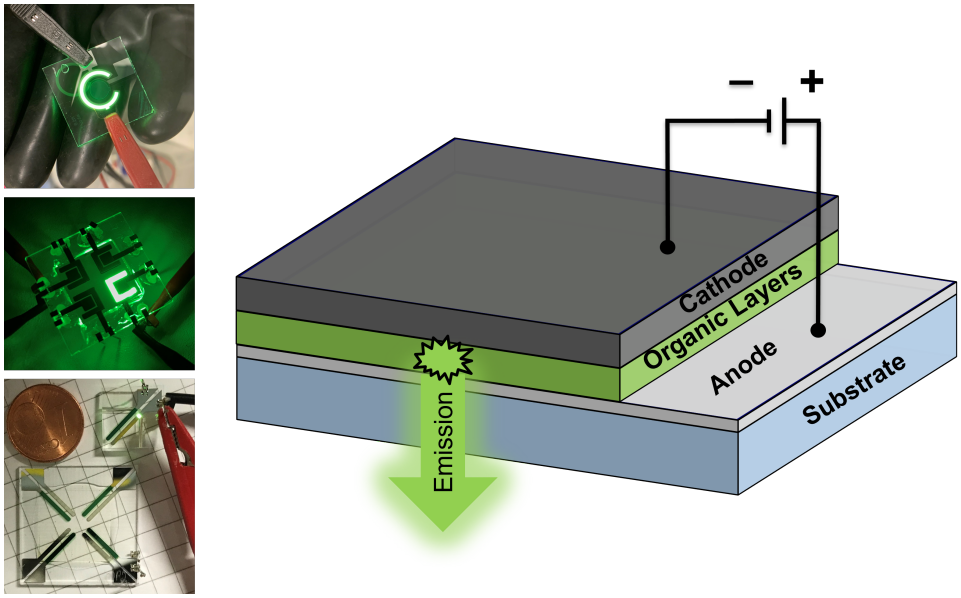

(a) Principal schematic of the device structure of a bottom-emitting OLED and images of different OLED geometries as an example.

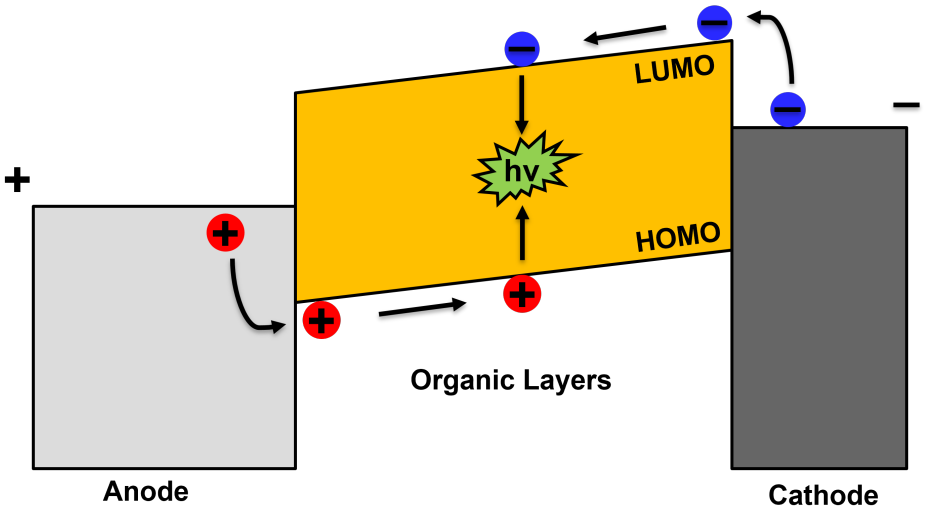

(b) Simplified working principle of an OLED. The four elementary steps of operation are charge injection, charge transport, exciton formation and radiative exciton decay.

Figure 2.7: Illustration of the working principle of an OLED.

ally, a thin layer of LiF or CsF (<1 nm) is evaporated to protect the organic layers from chemical reaction with the cathode. Also the chemical doping of organic materials to raise the intrinsic conductivity of the material is an example of the progress in OLED improvement in display applications. This so-called Guest-Host doped emitter system can improve the internal efficiency to nearly 100% [47–49]. In this work different OLED stacks were utilized. All of them are reported in the publications in Chapter 4.

2.3.2 Organic Photodetectors (OPDs)

Organic photodetectors (OPDs) attracted much attention as possible alternative to the well-established Si-photodiodes. The advantages assigned to these organic semiconductors are the same as for utilizing an OLED. One of the most outstanding advantages of OPDs over their inorganic counterparts is the spectral narrow-band characteristic. As a consequence, the spectral sensitivity of the photodetector can be tuned by the choice of the organic layers instead of integration of color filters. This enhances the attainable degree of miniaturization of POC devices, image sensors and many other applications [50]. The basic function of a photodetector is converting light into electrical current (photocurrent). The efficiency of the photoconversion process, also known as the external quantum efficiency (EQE), is defined as the ratio between the total collected number of photocarriers N_e and the total number of incident photons on the input area by a light source N_p and can be described as

$$EQE = \frac{N_e}{N_p}. \tag{2.7}$$

Figure 2.8(a) shows a simplified example of the structure of an OPD. In general, the structure of an OPD is very similar to the structure of an OLED, but the working principle is reversed. The light absorption generates in the organic layers photocarriers, which get transported to the respective electrodes for their final extraction. The device performance can also be tuned by adding additional organic layers to the sample structure. To minimize ohmic losses, HTLs and ETLs must be added to the structure. A typical configuration of the photoactive layer features two different organic semiconductors, referred to as donor and acceptor. These layers can be fabricated as a mixture (bulk heterojunction (BHJ)) or as adjacent layers (planar heterojunction (PHJ)). The generated excitons dissociate into electrons and holes directly at the donor-acceptor interfaces. The exciton-dissociating volume is determined by the

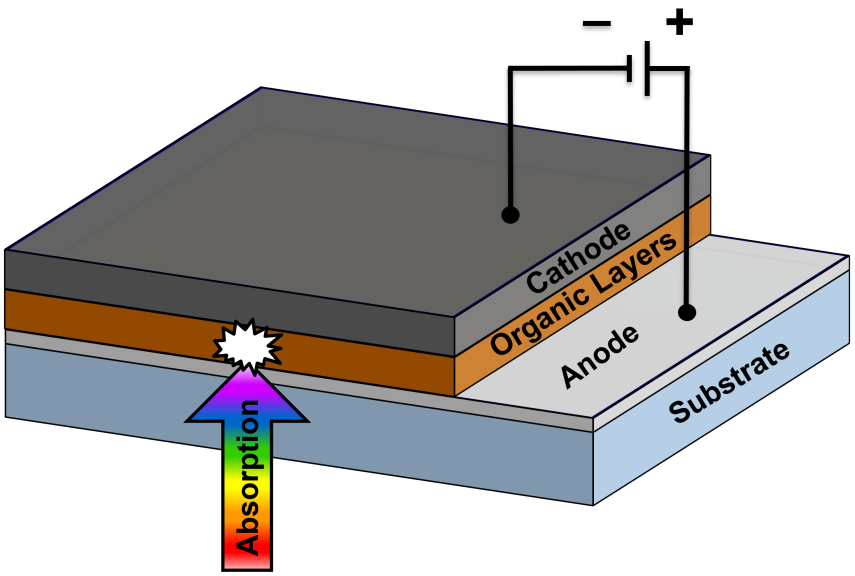

(a) Layer-by-layer schematic of an OPD structure.

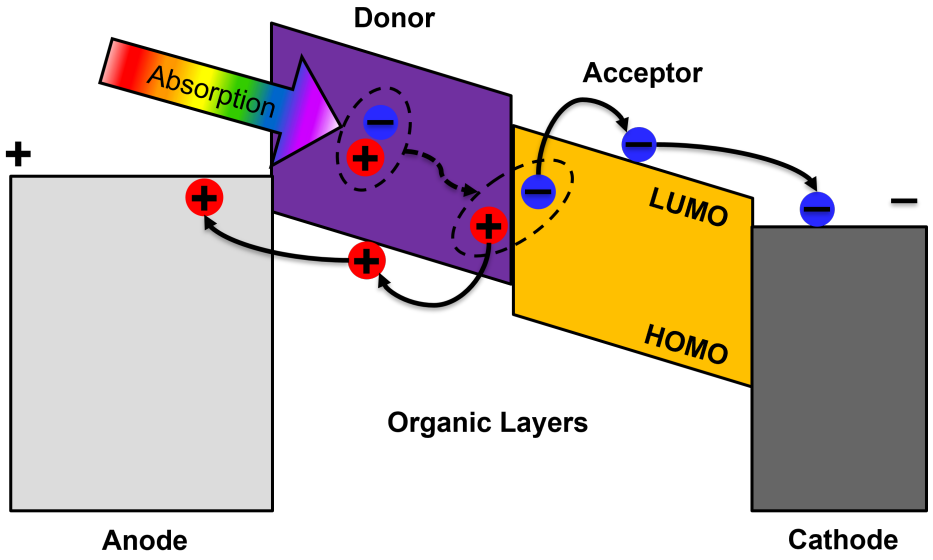

(b) Simplified energy diagram of an planar heterojunction (PHJ) OPD.

Figure 2.8: Illustration of structure and elementary steps of an OPD.

number of donor-acceptor interfaces [51, 52]. The donor and acceptor materials are usually chosen in such a way that under a reverse bias, the contacts with the electrodes act as blocking in nature. Thus, the darkcurrent can be suppressed and even weak light can be detected. Figure 2.8(b) shows a generalized energy diagram of an OPD with a PHJ configuration of the donor-acceptor layers. The four most elementary steps of OPD operation are: light absorption, photocarrier generation, photocarrier transport and photocarrier extraction [53].

2.4 Ray Tracing Simulations

To analyse the propagation of light within a model, ray tracing serves as a very effective tool for optical simulations. With a given initial position of a ray the chosen simulation algorithm involves the optical properties of surfaces, materials, the emission source itself and computes the exact propagation trajectory of the ray, which can be subjected to absorption, reflection or refraction among other effects.

In this work the COMSOL Multiphysics (Ray Optics Module) software was used to perform ray tracing simulations utilizing the non-sequential wavefront method. In contrast to sequential algorithms, COMSOL allows to analyze stray light, scattering and other physical interactions of a ray with objects after emission from a light source. The interactions can occur multiple times and rays can even be split to primary and secondary rays, which get transmitted, absorbed, scattered or reflected. In general, a ray undergoes two basic tracing steps. In the first step, the algorithm traces a released ray to the next surface and computes where the ray will hit the next surface. In the second step, the algorithm determines changes in the direction of the ray considering the boundary conditions, refracts or reflects the ray and traces the adjusted ray through the next media to the next surface. Thus, one entire ray tracing simulation consists of multiple iterations of these two basic steps. Additionally, it is not specified at the beginning of a simulation in which order the ray interacts with a certain medium. Only the light source is specified and the rays-media interactions are computed within the simulation.

One of the most interesting advantages of COMSOL is the ability to trace rays through graded-index or heterogeneous media. In the real world, materials can have a gradient in the refractive index [54]. The software numerically computes the adjustment of the direction using Snell's law for each discontinuity of the refractive index at interfaces. This law describes the relationship between the incident angle (θ_1) and the transmitted angle (θ_2) at the interface of two media with refractive indices n_1 and n_2 and can be expressed as [55]

$$n_1 \cdot \sin(\theta_1) = n_2 \cdot \sin(\theta_2). \tag{2.8}$$

To describe the propagation of rays, the wavefront ray tracing method uses a set of coupled first-order ordinary differential equations, which can be derived from the fundamental equation in geometrical optics. This equation is one of the solutions of the Helmholtz equation for an isotropic, linear, homogeneous

and time-independent material:

$$\nabla^2 \mathbf{E}(\mathbf{r}, t) + \mathbf{k}^2 \mathbf{E}(\mathbf{r}, t) = 0, \tag{2.9}$$

where $\mathbf{E}$ represents the electric field of the wave, $\mathbf{r}$ the position vector, t the time and $\mathbf{k}$ the wave vector. Geometrical optics considers the propagation of waves detached from their wave properties, i.e. $\lambda \to 0$. One of the possible solutions under the assumption that geometrical optics is applicable is the description of a monochromatic plane wave as [56]

$$\mathbf{E}(\mathbf{r}, t) = E_0 e^{i(\mathbf{k}\cdot\mathbf{r} - \omega t + \alpha)}, \tag{2.10}$$

with ω as the angular frequency, E_0 as the amplitude of the wave and α as an arbitrary phase shift. By substituting $\mathbf{k} \cdot \mathbf{r} - \omega t + \alpha$ as Ψ (also called the *eikonal function*) it follows, that the wave vector and the angular frequency can be expressed as [56]:

$$\mathbf{k} = \frac{\partial \Psi}{\partial \mathbf{r}} \qquad \omega = -\frac{\partial \Psi}{\partial t}. \tag{2.11}$$

Due to the analogy of the geometrical optics and the mechanics of particles, we know that the action S is related to the momentum $\mathbf{p}$ and the Hamiltonian H of a solid particle as [56]:

$$\mathbf{p} = \frac{\partial S}{\partial \mathbf{r}} \qquad H = -\frac{\partial S}{\partial t}. \tag{2.12}$$

Comparing the formulas 2.11 and 2.12 it is obvious that the wave vector plays the same role in geometrical optics as the momentum of the particle in mechanics, while the angular frequency plays the same role as the Hamiltonian (energy of the particle). This analogy leads directly to the equations [56]

$$\frac{d\mathbf{k}}{dt} = -\frac{\partial \omega}{\partial \mathbf{r}} \qquad \frac{d\mathbf{r}}{dt} = \frac{\partial \omega}{\partial \mathbf{k}}, \tag{2.13}$$

which can be used for the computation of the ray trajectory. Additionally, the angular velocity can be described in an isotropic medium as:

$$\omega = \frac{c|\mathbf{k}|}{n(\mathbf{r})} \tag{2.14}$$

and be simplified for regions with constant refractive index according to [57]:

$$\frac{d\mathbf{k}}{dt} = 0 \qquad \frac{d\mathbf{r}}{dt} = \frac{c\mathbf{k}}{n|\mathbf{k}|}. \tag{2.15}$$

For refractive index discontinuity at an interface, COMSOL Multiphysics numerically computes the direction of the refracted ray using Snell‘s law.

Chapter 3

State-of-the-Art Biomedical and Environmental Sensors

This chapter provides a short overview of published work related to optical detection with integrated OLED-OPD or inorganic LED-PD systems for biomedical and environmental applications. The most commonly applied system geometries in this field are given as an example.

3.1 Fluorescence and Reflectometry Sensors

A common research goal is to develop a low-cost, widely available and simple-to-fabricate LOC sensor for decentral sensing of biomarkers or nutrients. Researchers demonstrated highly impressive results particularly by deployment of OLEDs and OPDs as wearable sensors fabricated on flexible substrates for pulse oximetry or health monitoring as depicted in Figure 3.1 have been demonstrated by several groups [37, 39, 41]. The organic devices are usually fabricated on separate substrates followed by a subsequent lamination step of foils or other substrates. Each substrate has usually one type of optoelectronic device on it. To give an example for rigid substrates, Mayr et al. [58], Pais et al. [42] and Liu et al. [59] presented fluorescence measurement systems based on the hybrid integration of OLEDs and OPDs on separate substrates. The sensors were designed for the detection of dissolved oxygen, pH-level or the emission of Fluorescein and Rhodamine 6G, as can be seen in Figure 3.2. Furthermore, Lian et al. [19, 60] recently published remarkable results utilizing a microcavity OLED for the excitation and an inorganic photodiode for the detection of single-stranded DNA (ssDNA) of fetal bovine serum (FBS) and SARS-CoV-2 antibody, utilizing FRET and fluorescence-linked im-

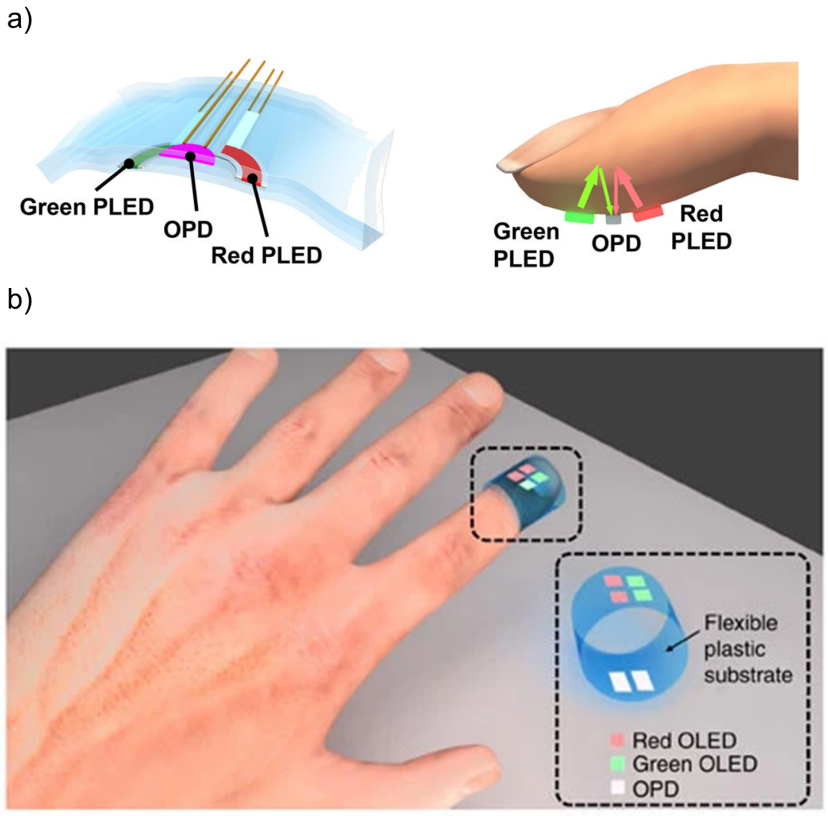

Figure 3.1: Schematics of the sensing setups. a) Device structure and the operation principle of a reflective pulse oximeter [37]. Reproduced and adapted under the terms and conditions of the CC-BY 4.0 license. Copyright 2016, the Authors, some rights reserved. Exclusive licensee American Association for the Advancement of Science.; b) Pulse sensor composed of two OLED arrays and two OPDs fabricated on a flexible substrate [41]. Copyright 2014, Macmillan Publishers Limited. Reproduced with permission from Springer Nature.

munosorbent assay (FLISA), respectively. While the aforementioned reports are highly relevant, they are not easily scaled up for parallel mass fabrication of sensor units since the sensors are mostly fabricated on separate substrates with one type of optoelectronic device on it or aligned in a transmission-based setup. Particularly the subsequent lamination to a single unit is highly sensitive to misalignment. The reproducibility increasingly suffers with the degree of miniaturization. To overcome these limitations the aim of the thesis is to develop a monolithic integrated OLED-OPD unit for POC applications, with all permanently aligned organic devices on one single substrate.

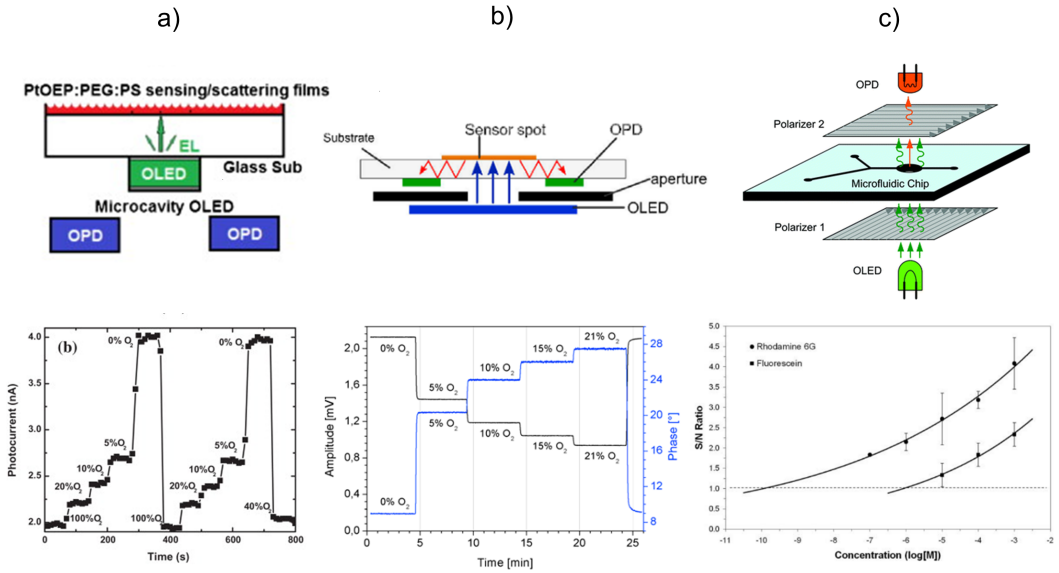

Figure 3.2: Schematics of the sensing setups and the corresponding measurements. a) Back-detection based OLED-OPD O_2 Sensor with a PtOEP:PEG:PS sensing film. Reprinted from [59]. Copyright 2013, with permission from Elsevier.; b) OLED-OPD sensor chip with circular fluorescence spots and ring-shaped OPDs on one single PET substrate. The excitation was realised by assembling an OLED and an aperture on the bottom-side of the chip. Reprinted from [58]. Copyright 2009, with permission from Elsevier.; c) Integrated LOC device with an OLED and an OPD. Between the organic devices a microfluidic chip was covered with two crossed polarizers to avoid OLED background light on the OPD [42]. Copyright 2001, Royal Society of Chemistry. Reproduced with permission.

3.2 Spectrophotometric Sensors

The spectrophotometric investigation of agriculturally and environmentally relevant nutrients such as nitrite and nitrate can be performed utilizing the popular Griess reagent. Early work has been conducted by Petsul et al. [33] using the colorimetric Griess reaction and an external inorganic light emitting diode (LED) with a spectrometer for the absorbance measurements, achieving a limit of detection (LOD) of 0.2 mM. Since then, a variety of different sensor systems with different optical device configurations have been reported. Colorimetric nitrite sensors mostly use LEDs as the light source. Devices such as CCD cameras, spectrometers, smartphone cameras, photomultiplier tubes (PMT) and photodiodes (PD) were recently successfully integrated on the detector side [10]. Figure 3.3 shows recently demonstrated portable systems from Czugala et al. [61] and Nightingale et al. [62] integrated with microfluidic

devices. Figure 3.3 a) shows a compact and transmission-based microfluidic

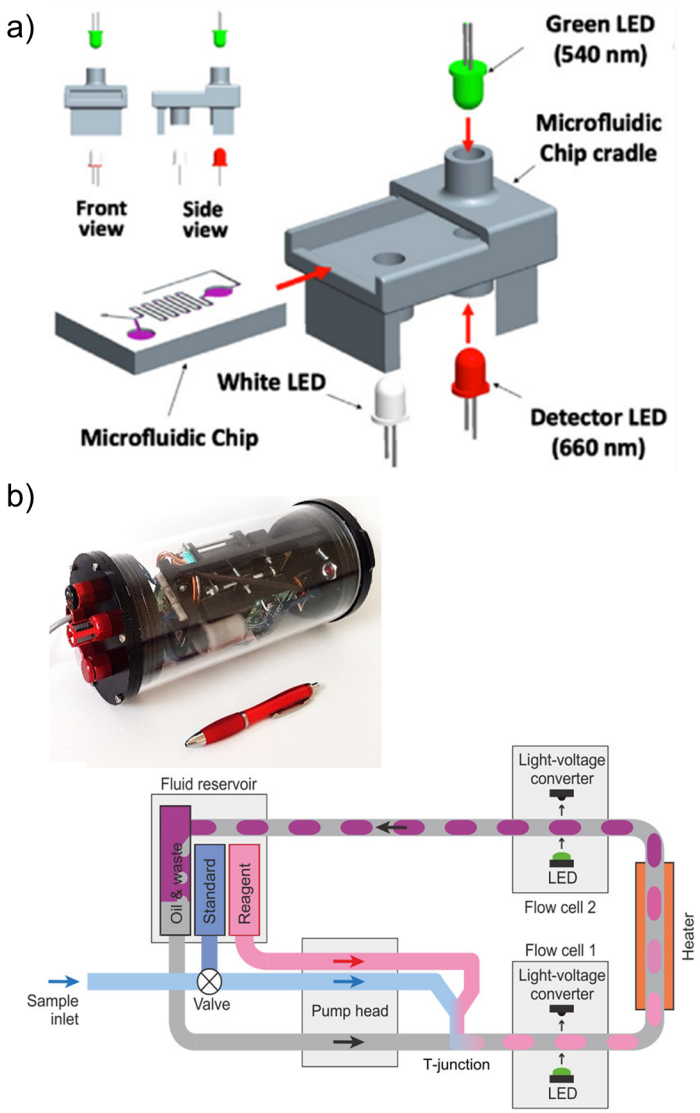

Figure 3.3: Model of the microfluidic device along with inorganic LEDs (green-emitter and red-detector). Reprinted from [61], Copyright 2009, with permission from Elsevier.; b) OLED-OPD sensor chip with circular fluorescence spots and ring-shaped OPDs on one single PET substrate. The excitation was realised by assembling an OLED and an aperture on the bottom-side of the chip [62]. Adapted with permission from Environ. Sci. Technol. 2019, 53, 16, 9677-9685. Copyright 2019, American Chemical Society.

platform (20 mm × 30 mm) for the color intensity change of the Griess reagent nitrite complex, which is highly dependent on the initial nitrite concentration using inorganic LEDs. Nightingale et al. proposed also recently a compact nitrite and nitrate detection unit, shown in Figure 3.3 b). This droplet based detection unit contains PTFE tubes instead of a microfluidic chip. The sub-

sequent transmission-based absorption measurement of the Griess reagent nitrite/nitrate complex is also based on external inorganic optical components. Although the achieved results are very impressive these systems are still rather bulky. For low-cost portable PON solutions, further miniaturization and simpler fabrication methods are needed.

Chapter 4

Publications in Peer-Reviewed Journals

This chapter represents the experimental and discussion part of this PhD thesis. The next five sections contain published journal papers arranged in a thematically reasonsable order. Each section contains an short abstract of the publication, the key findings, a statement about the own contribution in the paper and the included publication.
The first publication shows an investigation of a flexible OLED-OPD matrix designed for flexible sensing applications. The paper contains details of the fabtrication steps, the characterization of the system and an investigation of the system efficiency utilizing ray tracing simulations.
The second publication shows the fluorescence sensing performance of the OLED-OPD chip. In this work, the detection of fluorescence-labeled ssDNA was shown with different sensing scenarios. Additionally, a comprehensive ray tracing simulation study was implemented to investigate the system efficiency of the presented sensor model.
The third publication shows a first demonstration of a full-organic nitrite sensor chip. Here, a modified OLED-OPD organic stack was utilized for an environmental sensing application offering a highly compact sensor chip with a low detection limit and a high linearity. Finally, the last two sections present publications giving an outlook towards a integrated and wireless sensor for monitoring of chemical soil parameters in agricultural applications. Firstly, a microfluidic based soil solution extraction unit is demonstrated and characterized. Secondly, a low-power LoRa communication protocoll was investigated for underground sensor communication. Additionally, a drone was successfully integrated into the setup to extend the communication range up to 1000 m.

4.1 OLED-OPD Matrix for Sensing on a Single Flexible Substrate

4.1.1 Introduction

I. Titov, M. Köpke, N. C. Schneidewind, J. Buhl, Y. Murat, and M. Gerken, "OLED-OPD Matrix for Sensing on a Single Flexible Substrate," IEEE Sensors Journal, vol. 20, no. 14, pp. 7540-7547, Jul. 2020, doi: 10.1109/JSEN.2020.-2986051.

Statement about the own contribution:

Conceptualization	Planning	Implementation	Manuscript preparation
Moderate	Moderate	High	Moderate

- Implementation of the ray tracing simulation model and the investigation of the boundary conditions for an OLED-OPD design with optimized fluorescence excitation and detection efficiency.
- Planning, implementation and evaluation of the electrical and spectral characterization of the fabricated OLED-OPD system on various setups.
- Planning, implementation and evaluation of the reflectometry and fluorescence measurement experiments.
- Fabrication of microfluidic structures with transparent and black (absorptive) PDMS for stray light suppression.
- Estimation of the current OLED-OPD system efficiency.
- Preparation of the first draft of the manuscript and revision.

4.1.2 Abstract

In this work an OLED-OPD matrix with 18 monolithic integrated OLED and OPD pairs was designed and fabricated on a flexible PET substrate. The operation of the devices on foil was successfully demonstrated. However, one of the key findings was the leakage current on the OPDs while operating the OLEDs. It was necessary to separate the electrodes galvanically, to achieve a clear signal. To estimate the system efficiency ray tracing simulations were performed. The model was transferred to the COMSOL Multiphysics software and supplemented with a fluidic chamber. Firstly, the simulations were performed with 1 mm by 1 mm device sizes and fluorophore spots located between the OLED and the OPD. The simulation results indicate, that the illumination is not sufficient for an efficient excitation of the fluorophores. Next, a new design was calculated and implemented in the simulation to increase the excitation of the fluorophores. The device size was set to 140 µm × 140 µm. The average irradiance at the position of the fluorophores has been increased to 228 W/m^2 for the modified design, which is approx. 5 times higher than obtained from 1 mm × 1 mm devices even though the absolute emitted power of the smaller devices is approx. 50 times lower. To investigate a valid stray light suppression the fluidic chamber was modeled as transparent PDMS in the first step and black PDMS in the second step. The direct stray light from the OLED on the OPD was suppressed from 1.8% to 0.05% by utilizing black absorptive fluidic chamber. Furthermore, this work shows a successful excitation of the oxygen sensitive dye $Ru(dpp)_2Cl_3$ with a DPVBi:BCzVBi based blue-emitting OLED and proposes a platform technology for new multiplex sensor concepts based on optoelectronic devices for fluorescence measurements [63].

4.1.3 Published Paper

OLED-OPD Matrix for Sensing on a Single Flexible Substrate

Igor Titov, Markus Köpke, Nicole Christine Schneidewind, Janek Buhl, Yolande Murat, and Martina Gerken, *Member, IEEE*

***Abstract*—Integration of organic light emitting diodes (OLEDs) and organic photodetectors (OPDs) on flexible plastic substrates promises compact and low-cost optical detection units for multiplex sensors. These units may be laminated to a microfluidic system for sensing applications in a liquid. Here, a 6 × 6 element matrix of alternating blue OLEDs and OPDs is demonstrated on a single flexible plastic substrate. The devices are fabricated by masked thermal evaporation on a 200 μm thick polyethylene terephthalate (PET) foil. The individual device size is 1 mm × 1 mm. Both OLEDs and OPDs are demonstrated to work. The spectral characteristics are shown to be suitable for fluorescence measurements. Signals from fluorescence-labeled spots above the OPDs under OLED excitation are investigated. Successful operation of the OLED-OPD matrix for reflection measurement is demonstrated.**

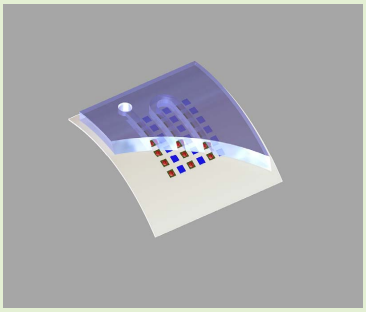

***Index Terms*— OLED, OPD, flexible, sensor, fluorescence.**

I. Introduction

FLEXIBLE and on-skin wearable sensors are highly promising for continuous health monitoring [1]. Lochner *et al.* proposed the realization of a pulse oximeter based on two types of OLEDs and OPDs on a single flexible substrate for a wearable oxygen sensor [2]. They demonstrated the device concept with OLEDs fabricated on separate rigid substrates. Mayr *et al.* presented an array of OPDs on a flexible substrate illuminated by an OLED on a separate substrate [3]. Liu *et al.* discussed different configurations of all-organic sensors for simultaneous oxygen and pH monitoring; OLEDs integrated with sensing films on rigid substrates and OPDs on separate substrates [4]. Yokota *et al.* presented an oximeter with two different OLEDs and an OPD by lamination of ultraflexible foils with different types of OLEDs and OPDs [5]. These foils were obtained by release from a sacrificial layer and each foil has only one type of optoelectronic device on it. While very impressive results are achieved with the lamination of several ultraflexible substrates, this procedure is not easily upscaled for the parallel fabrication of many sensor units. We have previously demonstrated the integration of OLEDs and OPDs on single rigid substrates in a monolithic integration approach [6] and proposed a device configuration for fluorescence measurements [7].

Our long-term goal is the realization of a small, multiplexed sensor for point-of-need analysis. For example, for testing five different parameters of interest with threefold redundancy and three reference sites, 18 simultaneous measurements need to be integrated on a chip. In the past we demonstrated a hand-held camera system for multiplex detection [16]. This approach combined a camera readout system with a disposable chip. An even more compact approach is proposed here based on hybrid integration of the optical readout system with the microfluidic system. For biosensing the surface may be functionalized with capture molecules for the binding of specific fluorescence-labelled biomaterial. Such an integrated approach would require only an electrical (or wireless) connection and could be read out, e.g., with a smartphone. All sensing elements are permanently aligned allowing a high degree of miniaturization. Using flexible plastic materials furthermore promises cost-effective, large-scale fabrication and rugged systems. The key element for the hybrid integration is an optoelectronic system providing 18 detection sites. Excluding movable parts this corresponds to 18 photodetectors –

Manuscript received March 10, 2020; accepted March 30, 2020. This work was supported in part by Interreg under Project RollFlex 1_11.12.2014 and in part by Zentrales Innovationsprogramm Mittelstand (ZIM) (Project AuToilette) under Grant ZF4558802RH8. This is an expanded paper from the 2019 IEEE International Conference on Flexible and Printable Sensors and Systems (FLEPS) [14]. The associate editor coordinating the review of this article and approving it for publication was Prof. Ravinder S. Dahiya. *(Corresponding author: Igor Titov.)*

The authors are with the Chair for Integrated Systems and Photonics, Institute of Electrical Engineering and Information Technology, Kiel University, 24143 Kiel, Germany (e-mail: igti@tf.unikiel.de).

Digital Object Identifier 10.1109/JSEN.2020.2986051

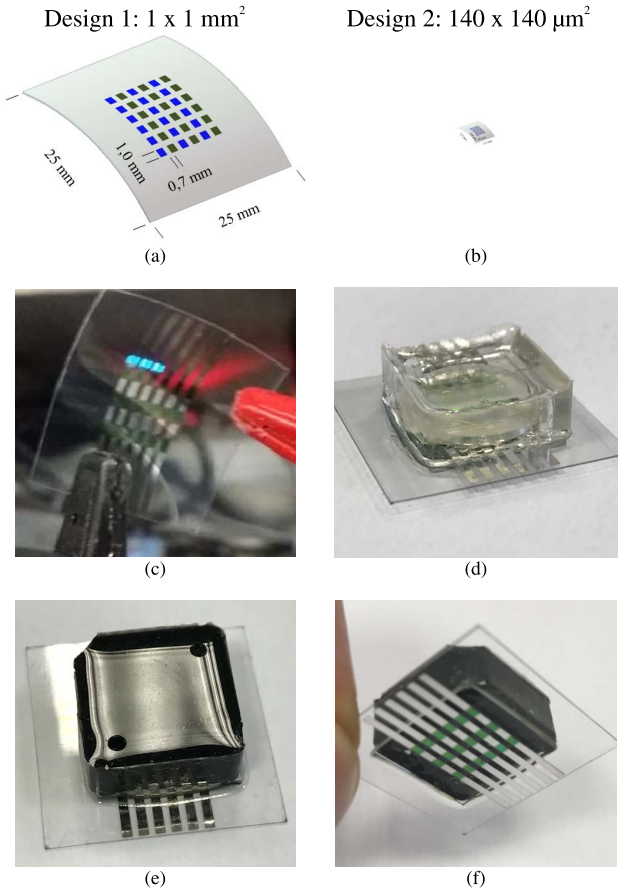

Fig. 1. (a) Design 1: Matrix layout with 18 OLEDs (blue) and 18 OPDs (green) on a 200-μm thick, 2.5 $\times$ 2.5 cm^2 PET foil. Device sizes are 1 $\times$ 1 mm^2. (b) Design 2: 18 OLEDs (blue) and 18 OPDs (green) with device sizes 140 $\times$ 140 μm^2 on a 200-μm thick PET foil. (c) Photograph of fabricated design 1. (d) Matrix of design 1 with microfluidic chamber in transparent PDMS. Holes for inlet and outlet are visible. (e,f) Matrix of design 1 with microfluidic chamber in black PDMS for stray light suppression.

one covering each detection site. Here, we investigate the realization of a matrix of 18 OPDs and 18 OLEDs as excitation sources on a single flexible substrate. Using pairs of OPDs and OLEDs allows for a flat, monolithically integrated design.

In section II we present ray tracing simulations for two different OLED-OPD matrix designs as shown in Fig. 1. Design 1 uses 36 devices of size 1 mm $\times$ 1 mm and design 2 has 36 devices of size 140 μm $\times$ 140 μm. In both designs a 200-μm thick PET foil is used. For both designs the case of a transparent microfluidic system is compared to the case of a black microfluidic system. The system efficiency for fluorescence sensing is calculated for the different designs. Section III presents the fabrication procedure for design 1. The experimental characterization of the OPD and OLED devices is given in section IV. Furthermore, section IV presents first fluorescence experiments. For these experiments we employ the oxygen sensitive dye $Ru(bpy)_3Cl_2$, which is

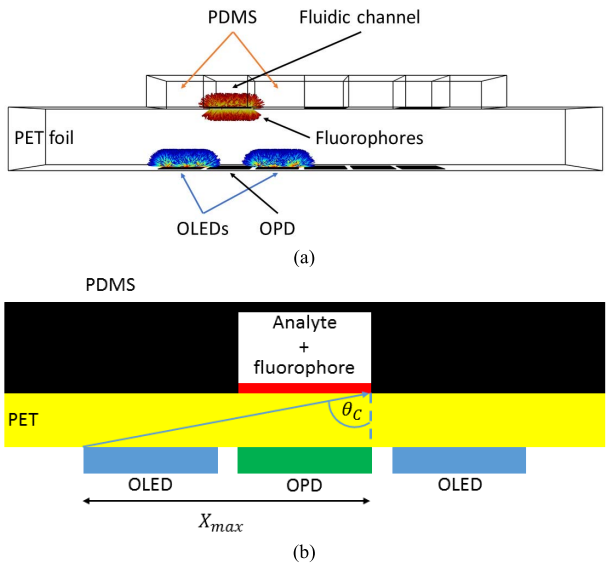

Fig. 2. Model for ray-tracing simulations. (a) Matrix of OLEDs emitting into the substrate and OPDs on PET foil. Fluorescence spots are above OPDs on the other side of the PET foil. A PDMS microfluidic chip is placed such that the fluidic channels are above the OPDs. The PDMS fluidic channels are placed above the fluorophore arrays. (b) 2D view of system with black PDMS microfluidics to prevent stray light.

used commonly to detect dissolved oxygen by fluorescence quenching [9]. Conclusions are given in section V.

II. Fluorescence Sensor Simulations

First, we conduct raytracing simulations in order to estimate the system efficiency for fluorescence sensing. As shown in Fig. 2 OLEDs are assumed to be emitting into the substrate and OPDs are sensitive to light incident from the substrate side. In the hybrid integration approach the PDMS microfluidic is assumed to be placed on the opposite side of the PET foil from the active organic optoelectronics. This ensures that a controlled optical path is achieved and no damage to the devices due to the liquid is expected. The fluidic channels are considered to be located above the row of OPDs. The fluorophores generating the signal are located above the OPD and the active region has the same size as the OPD. We choose this alignment to achieve the highest fluorescence intensity.

A. Simulation Model

In the ray-tracing simulation model, we do not model the full OLED and OPD stack. Instead we assume that the OLEDs emit from a transparent conductive indium tin oxide (ITO) layer with an emission power density of 1750 W/m^2. The OPDs are considered as absorptive surfaces. The microfluidic system is modelled by a 100 μm thick polydimethylsiloxane (PDMS) cap with channels to transport the water-based analyte. The channels have the same width as the OPDs. We consider microfluidics fabricated from transparent and black PDMS. Table I summarizes the refractive indices used in the simulation. The emission vacuum wavelength is set

TABLE I
OPTICAL PROPERTIES USED FOR THE SIMULATION

Medium	Refractive index	Source
ITO	1.9858	[11]
H_2O	1.3376	[12]
PET	1.6	[13]
PDMS	1.4425	[10]

to 450 nm. We assume a Lambertian emission pattern for each individual OLED and assume that the detection region is excited by two neighboring OLEDs. The simulations are carried out with the Ray Optics Module in COMSOL Multiphysics®. The number of rays per release was set to 10^3 with 10^3 rays in wave vector space.

B. Simulation Results

First the irradiation profile of the top surface of the PET foil by the OLEDs is considered. This surface is defined as a cut-plane for accumulating irradiation power in the ray-tracing software. Figs. 3(a,b) show the simulated emission power density for two operational OLEDs for design 1 and design 2, respectively. We use the same radiosity for the small devices as for the large devices. The radiosity of the small OLEDs is kept at 1750 W/m^2. If a larger active area is desired, stripes of active devices should be used. Note that the radiosity of the OLED is transferred to the top surface of the PET foil above the OLED for design 1 as the device size is significantly larger than the PET-foil thickness. For design 2 with 140 μm × 140 μm OLEDs the light is already spread to a larger area with a reduced irradiance at the top side of the 200-μm thick PET foil above the OLED.

At the position of the fluorescence region above the OPDs only a small irradiance is found. The average irradiance on the sensitive spot is obtained by defining the fluorophores as an accumulator. An average irradiance of 43 W/m^2 is simulated at the location of the fluorophores for design 1 The average irradiance at the position of the fluorophores is increased to 228 W/m^2 for design 2, which is ∼ 5 times higher than obtained from 1 mm × 1 mm devices even though the absolute emitted power of the smaller devices is ∼50 times lower. Fig. 3(c) depicts a selection of rays showing that still only a relatively small fraction of rays reaches the illumination area of interest.

Next, we consider how much of the emitted fluorescence reaches the detector. Here, we consider the oxygen sensitive dye $Ru(bpy)_3Cl_2$ as an example. Suzuki *et al.* measured the absolute quantum yield Φ_P for this ruthenium complex at 298K to be 0.063 (in deaerated water) [8]. We used the results obtained from the simulation shown in Fig. 3(a,b) to calculate the emitted fluorescent light after the excitation of the fluorophore. For design 1 the average irradiation of 43 W/m^2 of the dye corresponds to a fluorescence radiosity of ∼ 2 W/m^2 for the given quantum yield and considering the wavelength shift from 450 nm to 615 nm. For design 2 the average irradiation of 228 W/m^2 of the dye corresponds to a fluorescence radiosity of ∼ 10.5 W/m^2. To investigate

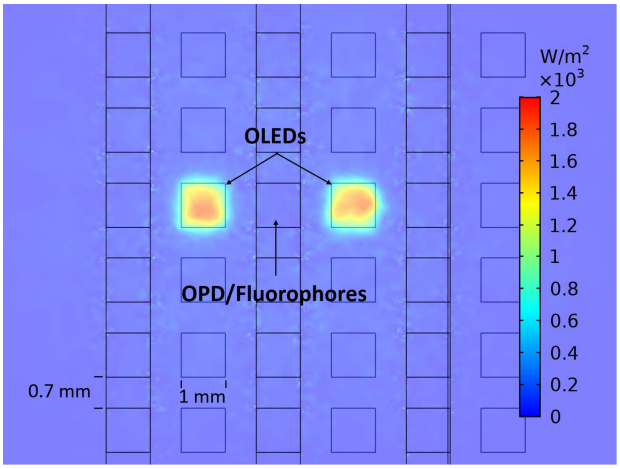

(a)

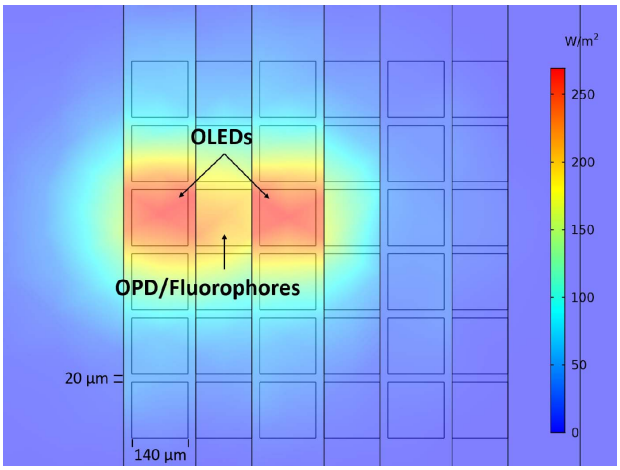

(b)

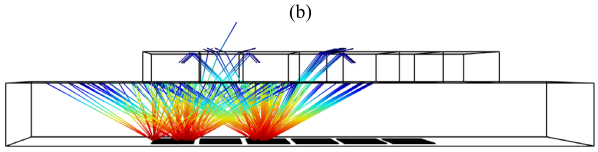

(c)

Fig. 3. (a) Surface distribution of the 1 mm × 1 mm OLED radiosity of 1750 W/m^2 on PET-foil. (b) Surface distribution of the 140 μm × 140 μm OLED radiosity of 1750 W/m^2 on PET-foil. (c) Side view of 140 μm × 140 μm active device matrix with small selection of rays.

the amount of detected emission on the OPD, we defined the fluorophore as a spherical ray release device with a source radiance of 10.5 W/m^2 and the OPD as an accumulator. This results in an average irradiance of 0.48 W/m^2 on the 140 μm × 140 μm OPD device equaling a received power of ∼ 9.5 nW. For design 1 the average irradiance is calculated to be ∼ 1 W/m^2. The system efficiency from OLED radiosity in W/m^2 to OPD irradiance in W/m^2 is 0.6‰ for design 1 and 0.3‰ for design 2, respectively.

Due to the better system efficiency as well as due to less stringent fabrication requirements, we fabricated design 1.

TABLE II
EFFICIENCY ANALYSIS

	Design 1: 1 x 1 mm² devices; transparent PDMS	**Design 1: 1 x 1 mm² devices; black PDMS**	**Design 2: 140 x 140 µm² devices; transparent PDMS**	**Design 2: 140 x 140 µm² devices; black PDMS**
OLED emission power density J_{OLED}	1750 W/m²	1750 W/m²	1750 W/m²	1750 W/m²
Fluorophore area	1 x 1 mm²	1 x 1 mm²	140 x 140 µm²	140 x 140 µm²
Fluorophore illumination avg.	43 W/m²	43 W/m²	228 W/m²	228 W/m²
Fluorophore quantum efficiency	6.3%	6.3%	6.3%	6.3%
Fluorescence on OPD E_{OPD}	1 W/m²	1 W/m²	0.5 W/m²	0.5 W/m²
System efficiency η = E_{OPD}/J_{OLED}	**0.6 ‰**	**0.6 ‰**	**0.3 ‰**	**0.3 ‰**
Stray light on OPD	1.8%	0.05%	~0%	~0%

Before continuing to the experimental results, we want to use the ray tracing simulations to consider the stray light from OLED to OPD for the two different designs. This is background light in the experiment.

The OLED stray light on the OPD is simulated by defining the OPD between two OLEDs as a ray detector. This function counts the incident rays, which are reflected by interfaces. For the design 1 and transparent PDMS, we obtained a value of 1.8%, i.e., 1.8% of the total number of released rays is directly detected on the OPD. In contrast, for device 1 and black PDMS, modeled as perfect absorber, we observe a reduction to 0.05%.

In design 2 we chose the lateral dimension $X_{\max}$ of one OLED-OPD pair in Fig. 2(b) such that the ray shown is just at the critical angle for total internal reflection θ_C. Thus, light guided by total internal reflection does not reach the OPD in this design. All other rays directly incident from the OLED onto the fluorophore have a smaller angle. For the interface between water with a refractive index $n_{H2O} = 1.3376$ and PET with $n_{PET} = 1.6$ we obtain $\theta_C \approx 57°$. For a PET-foil thickness of 200 μm this gives us a value of $X_{\max} \approx 300$ μm. Consequently, the individual device size was set to 140 μm × 140 μm with a distance of 20 μm between devices.

Due to the close positioning of OLEDs and OPDs, stray light is effectively suppressed for design 2 and is 0% within the simulation assumptions. The simulation results are summarized in Table II.

III. OLED-OPD MATRIX FABRICATION

Fig. 1 depicts the matrix layout of design 1, which we fabricated. The OLED and OPD layer sequences are given in Fig. 4. We realized 18 OLEDs and 18 OPDs with an active area of 1 × 1 mm² each on one substrate. The OLED-OPD matrix is fabricated on a 25 × 25 mm² polyethylene terephthalate (PET) foil with a thickness of 200 μm and with an indium tin oxide (ITO) top layer of 20 nm (EMI Tape Co., Thorlabs).

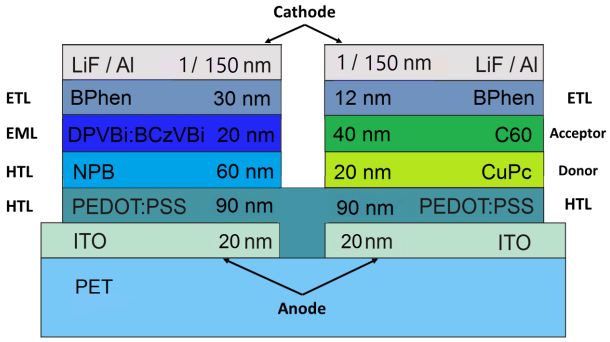

Fig. 4. Schematic diagram of OLED stack (left) and OPD stack (right) on a single PET substrate. The function of the layers is as follows: ETL: electron transport layer, EML: emission layer, HTL: hole transport layer.

Via ultraviolet (UV) lithography and wet etching, the ITO layer is structured to form transparent anode contact pads. For this purpose, the PET coated with ITO is cleaned first in acetone and then in isopropanol in an ultrasonic bath for 10 minutes, each. After dehydrating the sample for 15 minutes at 90°C on a hotplate, the photoresist (AZ1518, MicroChemicals) is spin coated at 2850 rpm for 30 seconds. Then a soft bake for 60 seconds at 90°C on a hotplate is performed. After UV exposure and resist development (60 seconds with developer AZ726 MIF, MicroChemicals, stopped with deionized (DI) water) the resist is hardened at 115°C for 60 seconds. To remove the excess ITO and form the ITO anode pads the sample is etched with 30% hydrochloric acid for 2 minutes. Next, the resist is stripped off the sample by using acetone for 2 minutes and isopropanol for 10 minutes in an ultrasonic bath.

Before the first organic layers for the OLEDs and OPDs are processed the samples are dehydrated for 12 hours at 90°C and treated with oxygen plasma (2 minutes, 8 sccm O_2 and 100 W RF power) such that the surface becomes hydrophilic for better adhesion of the organic layers.

First an organic 90 nm thin layer of poly(3,4-ethylenedioxy thiophene):polystyrene sulfonate (PEDOT:PSS, Sigma-Aldrich Chemie GmbH) is deposited by wet-process using the spin-coating technique (3500 rpm, 30 s) on top of the anode. Following this common step for both OLEDs and OPDs, the remaining organic layers on top of the PEDOT:PSS are evaporated using a thermal evaporation system.

The OLED layer structure is as follows: a layer of 60 nm of N,N'-Bis(naphthalene-1-yl)-N,N'-bis(phenyl) benzidine (NPB) as hole transport layer (HTL), then for the emission layer a 20 nm of 4,4'-Bis(2,2-diphenylvinyl)-1,1'-biphenyl (DPVBi) doped with 5% of 4,4'-Bis(9-ethyl-3-carbazovinylen)1,1'-biphenyl (BCzVBi) to generate a narrowband emission spectrum in the blue spectral range. For the combined electron transport layer (ETL) and hole blocking layer (HBL) a 30 nm layer of 4,4'-Bis(9-ethyl-3-carbazovinylene)-1,1'-biphenyl (BPhen) is deposited, followed by cathode pads consisting of 1 nm lithium fluoride (LiF) and 150 nm aluminum (Al).

The OPD layer structure on the PEDOT:PSS starts with an electron donor layer of 20 nm Copper(II) phthalocyanine (CuPc), then an electron acceptor layer of 40 nm C60, followed by 12 nm BPhen (ETL). The cathode pads have the same layer structure as for the OLED. Fig. 2(c) shows a photograph of a fabricated device matrix operated with a 9 V battery.

For the microfluidic system we suggest to employ a black flexible polymer for the suppression of stray light. We fabricated microfluidic chambers by molding polydimethylsiloxane (PDMS) mixed with Carbon Black (Ketjenblack®EC-600JD, Akzo Nobel Polymer Chemicals B.V.) from a Teflon mold. These systems are still rather bulky as shown in Fig. 1(e,f), but may be further miniaturized.

IV. Experimental Characterization

A. Single-Device Characterization

To prevent degradation of the organic materials during the characterization in the oxygen environment the OLED-OPD matrix was encapsulated with glass and placed in a darkened environment. Characterization is performed without the microfluidic chamber. Two Source Measure Units (SMUs) are used for electrical characterization. The I-V characteristic of the OLED fabricated on PET foil is shown in Fig. 5(a). The emission area of the OLED is aligned above a S1223-01 photodiode (Hamamatsu Photonics K.K.) to obtain the relative light output at different operating voltages. For comparison the I-V curve for an OLED on glass with the same layer stack, but 130 nm ITO anode is plotted as well. The OLEDs fabricated on PET foil show a higher onset voltage and a poorer luminous efficiency. This is attributed to the series resistance of the thin 20 nm ITO layer.

The OPD device characteristics are shown in Fig. 5(b). The I-V curves of two sample OPDs – one on PET and one on glass – are measured under dark conditions and illumination by a red LED operated at 2.5 V and 20 mA (10560 mcd, LL-503VC2E-V1-4DC, Lucky Light Electronics Co., Ltd). The OPD on PET (blue) and on glass (red) show typical

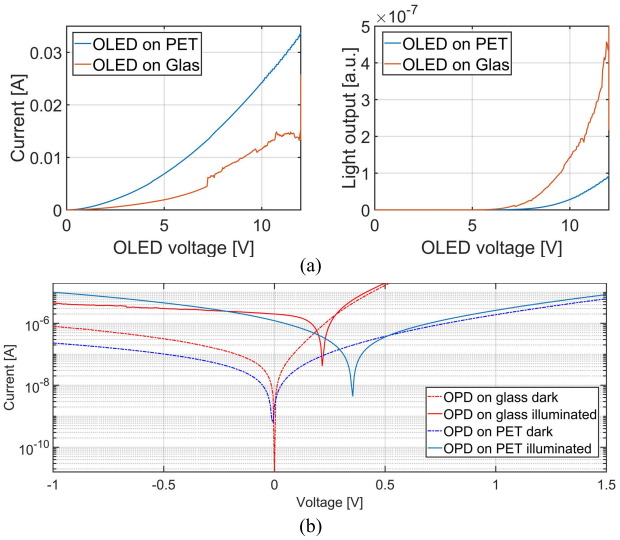

Fig. 5. (a) I-V curve (left) and the light output with voltage (right) for an OLED fabricated on glass (orange) and an OLED fabricated on PET (blue). (b) I-V characteristic of the OPDs fabricated on PET and glass in the dark and under illumination.

diode characteristics. The open-circuit voltage and the short-circuit current under illumination were observed to be 354 mV and -1.21 μA for PET and 216 mV and -2 μA for glass, respectively. The I-V curves show that the light conversion efficiency of the glass device is higher than on PET foil. More details on the device behavior were presented in [17] and [18].

B. OLED-OPD-Pair Characterization

Using a simple matrix electrode design leads to leakage currents when operating OLEDs and OPDs simultaneously. Thus, we fabricated a second-generation matrix with an electrode design galvanically separating neighboring OLED and OPD devices. In Fig. 6(a) we plot the OPD short circuit photocurrent for rectangular pulse operation of the neighboring OLED at 15 V, 1.2 mA and 0.25 Hz. This measurement was carried out in dark environment without the black PDMS chamber presented in Fig. 1(e,f). The switching behavior is clearly observed and reproduced without showing degradation of the organic materials. The light from the OLED reaching the OPD through the common substrate induces an absolute photocurrent at $\sim$ 3.9 nA. This is the stray light discussed in section II. The OPD dark current amounts to $\sim$ 0.25 nA. Fig. 6(b) shows the direct light of the OLED on the OPD while manually reflecting OLED light to the OPD with an optical mirror. In this experiment, the OLED was operated continuously at 10 V. The absolute value of the background current was observed to be $\sim$ 0.95 nA. The OPD photocurrent increases to $\sim$ 7.2 nA by maximizing the reflection of direct light. These experiments show the successful linking of OLED and OPD.

C. Fluorescence Sensing

As the test case for fluorescence sensing we consider the fluorophore $Ru(dpp)_2Cl_3$, which is widely used for

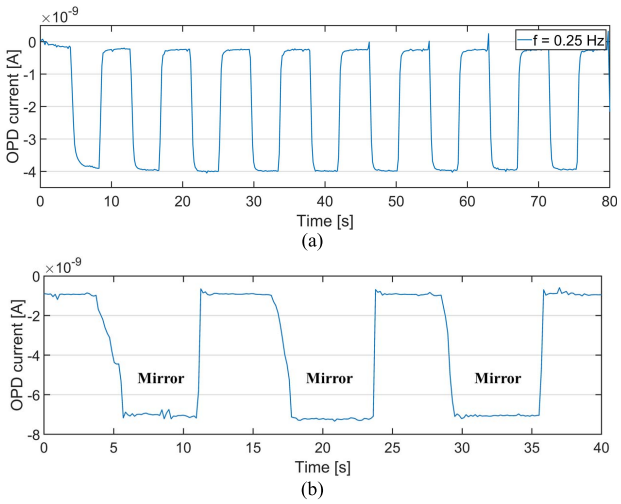

Fig. 6. (a) OPD on PET short circuit photocurrent for rectangular pulse modulated OLED at 15 V, 1.2 mA and 0.25 Hz. (b) Enhancement of OPD signal by manual reflection of direct OLED light onto the OPD with a silver mirror. The OLED is operated continuously at 10 V.

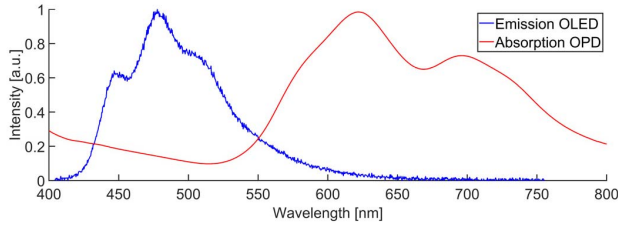

Fig. 7. Normalized emission spectrum of the OLED and absorption spectrum of the OPD.

dissolved-oxygen sensing [15]. The absorption and the emission maxima are located at 450 nm and 620 nm, respectively. Fig. 7 shows the absorption spectrum of the OPD layer stack and the emission spectrum of the OLED layer stack. The devices used for this characterization were fabricated on separate glass substrates for spectral analysis. The spectral characteristic demonstrates that the peaks are suitably located for excitation and fluorescence detection of $Ru(dpp)_2Cl_3$. An additional optical filter in front of the OPD is necessary to obtain the necessary suppression of the excitation light in fluorescence measurements. This filter may either be included on the substrate foil or integrated in the OPD design.

Next, we coated a PET foil with $Ru(dpp)_2Cl_3$. The immobilization was performed in methyltriethoxysilane (MTEOS, Sigma-Aldrich Chemie GmbH, Germany) by the sol-gel process presented in [15]. The chemicals were analytical grade and used as received. Placing this $Ru(dpp)_2Cl_3$-coated PET foil on top of the OLED-OPD matrix we measure the OLED spectrum through the $Ru(dpp)_2Cl_3$-coated PET foil with a fiber-coupled spectrometer. An optical 560 nm longpass filter (O-56, Edmund Optics, Inc.) is included in front of the spectrometer to filter direct OLED light.

Fig. 8(a) shows the difference spectrum of the $Ru(dpp)_2Cl_3$-coated PET foil. In the inset, we plot the original data

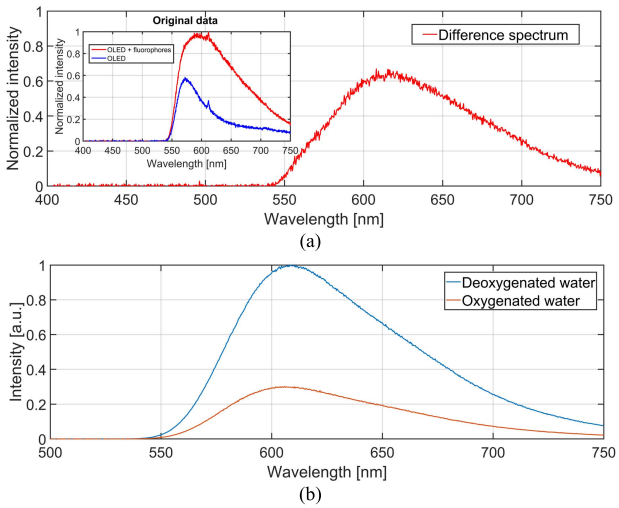

Fig. 8. (a) Difference spectral characteristics of the emission of a $Ru(dpp)_2Cl_3$-coated PET foil excited by the OLED (560-nm long-pass filter employed in both measurements). Inset: Measured data used for differencing. (b) For comparison: Emission characteristic of $Ru(dpp)_2Cl_3$ from a dissolved oxygen quenching measurement carried out with a blue LED.

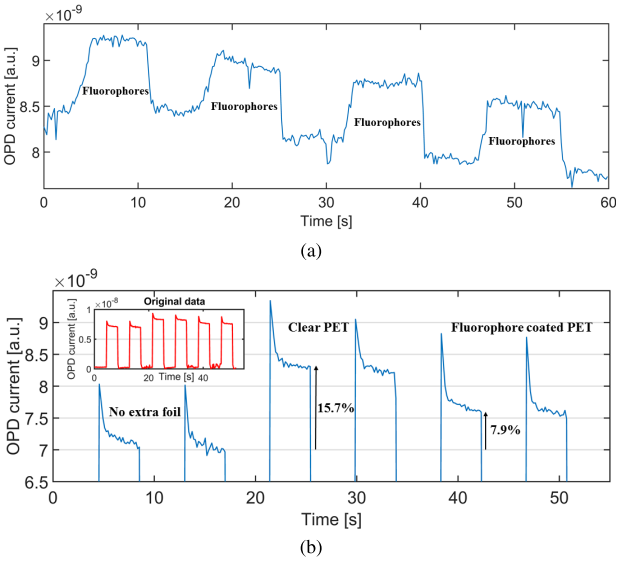

Fig. 9. (a) Enhancement of the photocurrent by adding a $Ru(dpp)_2Cl_3$-coated PET foil on top of the OLED-OPD matrix. (b) Signal comparison between a clear PET foil and a $Ru(dpp)_2Cl_3$-coated PET foil.

normalized at the emission peak with $Ru(dpp)_2Cl_3$-coated PET foil (red curve). The difference of the signals shows a maximum, which fits to the expected emission of $Ru(dpp)_2Cl_3$ shown in Fig. 8(b).

In Fig. 9(a) we present a measurement of an OLED-OPD matrix fabricated on PET foil, which shows the OPD photocurrent with a continuously operated neighboring OLED at 15 V and $\sim$ 3.5 mA. The increase of the photocurrent was achieved by adding and removing the $Ru(dpp)_2Cl_3$ coated PET foil on top of the operated matrix.

In order to investigate if the OPD current increase is due to a fluorescence effect or due to increased reflection off the

substrate, we conducted a second type of experiment (using a new matrix as the old one was degraded). We operate the OLED with a rectangular pulse at 20 V and ∼ 2.25 mA to have a clear base line. Then we place a non-coated PET foil above the matrix and finally exchange this with the $Ru(dpp)_2Cl_3$ coated PET foil. Fig. 9(b) shows the resulting OPD photocurrent for two pulses in each of the three conditions – no extra PET foil, non-coated PET foil, and $Ru(dpp)_2Cl_3$ coated PET foil. The first two peaks are caused by stray light from the OLED to the OPD resulting in an OPD current of ∼7 nA. The second pair of peaks are caused by reflection off the non-coated PET foil superimposed on the stray light yielding an OPD current of ∼8.3 nA. The last pair of peaks shows the superposition of stray light, reflectance and the fluorophore effect of the $Ru(dpp)_2Cl_3$ coated PET foil. The signals decrease to ∼7.6 nA in comparison to clear PET. Thus, we conclude that absorption effects of the fluorophore reducing the signal dominate fluorescence effects increasing it. This result shows that for successful fluorescence sensing OPDs with a narrowband absorption around the fluorescence or a longpass filter for direct light suppression need to be used. On the other hand, the experiments also clearly demonstrate that the OLED-OPD matrix detection unit is functional and may be used for sensing tasks requiring the measurement of a change in direct light reflection, e.g. absorption or refractive index measurements.

V. Conclusions

In conclusion, we demonstrated the monolithic integration of a matrix of 18 OLEDs and 18 OPDs on a flexible substrate. Operation of both device types as well as detection of OLED light with the OPD was demonstrated. It was found that electric matrix operation of OLEDs and OPDs leads to leakage currents between the two device types due to the highly different operating voltages. Galvanic separation of OLEDs and OPDs on a single substrate prevents such leakage currents. The lifetime of the devices was short, hence they were characterized encapsulated with glass. This prevents degradation of the organic layers upon oxygen contact. For flexible applications the substrates can be encapsulated with an additional foil on top of the active devices.

The spectra of the designed devices have suitable peak positions for fluorescence measurements. We demonstrated the excitation of the oxygen sensitive fluorophore $Ru(dpp)_2Cl_3$ with the OLED. The fluorescence light was observed with a spectrometer. The OPD detects a superposition of direct light effected by fluorophore absorption and the fluorescence signal. Our experiments suggest that the absorption effect is dominating in the current system. Thus, OPDs with a narrowband absorption around the fluorescence are preferable. Alternatively, a longpass filter needs to be integrated.

For suppressing stray light from the OLED to the OPD we suggest the use of smaller device sizes. Design 2 is also preferable for a smaller overall system size.

The demonstrated flexible OLED-OPD matrix serves as a platform technology for new multiplex sensor concepts based on optoelectronic measurements. It is ready to use for absorption or refractive index measurements changing the intensity of reflected light.

References

[1] Kenry, J. C. Yeo, and C. T. Lim, "Emerging flexible and wearable physical sensing platforms for healthcare and biomedical applications," *Microsyst. Nanoeng.*, vol. 2, no. 1, Dec. 2016, Art. no. 16043.

[2] C. M. Lochner, Y. Khan, A. Pierre, and A. C. Arias, "All-organic optoelectronic sensor for pulse oximetry," *Nature Commun.*, vol. 5, no. 1, pp. 1–7, Dec. 2014.

[3] T. Mayr *et al.*, "An optical sensor array on a flexible substrate with integrated organic opto-electric devices," *Procedia Eng.*, vol. 5, pp. 1005–1008, Jun. 2010.

[4] R. Liu, T. Xiao, W. Cui, J. Shinar, and R. Shinar, "Multiple approaches for enhancing all-organic electronics photoluminescent sensors: Simultaneous oxygen and pH monitoring," *Analytica Chim. Acta*, vol. 778, pp. 70–78, May 2013.

[5] T. Yokota *et al.*, "Ultraflexible organic photonic skin," *Sci. Adv.*, vol. 2, no. 4, Apr. 2016, Art. no. e1501856, doi: 10.1126/sciadv.1501856.

[6] D. Threm, J. L. Gugat, A. Pradana, M. Radler, J. Mikat, and M. Gerken, "Self-aligned integration of spin-coated organic light-emitting diodes and photodetectors on a single substrate," *IEEE Photon. Technol. Lett.*, vol. 24, no. 11, pp. 912–914, Jun. 2012.

[7] S. Jahns, A. F. K. Iwers, J. Balke, and M. Gerken, "Organic optoelectronics for lab-on-chip fluorescence detection," *Technisches Messen*, vol. 84, no. s1, pp. 48–51, Sep. 2017.

[8] K. Suzuki *et al.*, "Reevaluation of absolute luminescence quantum yields of standard solutions using a spectrometer with an integrating sphere and a back-thinned CCD detector," *Phys. Chem. Chem. Phys.*, vol. 11, no. 42, pp. 9850–9860, 2009.

[9] X. Xiong, Y. Tang, and B. Zheng, "Dissolved oxygen sensor based on sol-gel matrix doped with tris(2,2'-bipyridine)ruthenium dichloride," *J. Chongqing Univ.*, vol. 12, no. 1, pp. 11–15, 2013.

[10] F. Schneider, J. Draheim, R. Kamberger, and U. Wallrabe, "Process and material properties of polydimethylsiloxane (PDMS) for optical MEMS," *Sens. Actuators A, Phys.*, vol. 151, no. 2, pp. 95–99, Apr. 2009.

[11] T. A. F. König *et al.*, "Electrically tunable plasmonic behavior of Nanocube—Polymer nanomaterials induced by a redox-active electrochromic polymer," *ACS Nano*, vol. 8, no. 6, pp. 6182–6192, Jun. 2014.

[12] G. M. Hale and M. R. Querry, "Optical constants of water in the 200-nm to 200-μm wavelength region," *Appl. Opt.*, vol. 12, no. 3, p. 555, Mar. 1973.

[13] M. Biron, "Plastics solutions for practical problems," in *Thermoplastics Thermoplastic Composites*, 2nd ed. New York, NY, USA: William Andrew, 2013, pp. 831–984.

[14] N. Schneidewind, M. Kopke, J. Buhl, Y. Murat, and M. Gerken, "OLED-OPD matrix for fluorescence sensing on a single flexible substrate," in *Proc. IEEE Int. Conf. Flexible Printable Sensors Syst. (FLEPS)*, Glasgow, U.K., Jul. 2019, pp. 1–3.

[15] C. McDonagh, P. Bowe, K. Mongey, and B. D. MacCraith, "Characterisation of porosity and sensor response times of sol-gel-derived thin films for oxygen sensor applications," *J. Non-Crystalline Solids*, vol. 306, no. 2, pp. 138–148, 2002.

[16] S. Jahns *et al.*, "Handheld imaging photonic crystal biosensor for multiplexed, label-free protein detection," *Biomed. Opt. Express*, vol. 6, no. 10, p. 3724, Oct. 2015, doi: 10.1364/boe.6.003724.

[17] T.-G. Kim, H.-S. Oh, Y.-H. Kim, and W.-Y. Kim, "Study of deep blue organic light-emitting diodes using doped BCzVBi with various blue host materials," *Trans. Electr. Electron. Mater.*, vol. 11, no. 2, pp. 85–88, Apr. 2010, doi: 10.4313/teem.2010.11.2.085.

[18] P. Peumans and S. R. Forrest, "Very-high-efficiency double-heterostructure copper phthalocyanine/C60 photovoltaic cells," *Appl. Phys. Lett.*, vol. 79, no. 1, pp. 126–128, Jul. 2001, doi: 10.1063/1.1384001.

Igor Titov was born in Kazakhstan in 1991. He received the master's degree in electrical engineering and information technology from Kiel University, Germany, in 2018, where he is currently pursuing the Ph.D. degree with the Chair for Integrated Systems and Photonics, Institute of Electrical Engineering and Information Technology. His research interests include biosensors and lab-on-a-chip systems.

Markus Köpke was born in Hohwacht, Germany, in 1970. He received the State Certified Technician in electrical engineering from the Technical College, Kiel, in 2003. Since 2014, he has been a Technician with the Institute of Electrical Engineering and Information Technology, Kiel University. His research skills are the manufacturing of thin film layers for optoelectronic devices, fabrication of nanostructured surfaces, and development of processes in manufacturing of micro devices and characterization.

Nicole Christine Schneidewind (born Klindtworth) was born in Viborg, Denmark, in 1983. She received the B.Sc. and M.Sc. degrees in engineering and mechatronics, profile in nanotechnology from the University of Southern Denmark, Sønderborg. Her research interests include production and development of matrices OLED's and OPD's and production of flexible matrices.

Janek Buhl was born in Kiel, Germany, in 1990. He received the B.S. and M.S. degrees in electrical engineering, information technology and business management and the second B.S. degree in chemistry and business management from Kiel University, Germany, in 2017. He is currently pursuing the Ph.D. degree with the Chair for Integrated Systems and Photonics, Institute of Electrical Engineering and Information Technology. He is also a Scientific Staff Member with the Institute of Electrical Engineering and Information Technology. His research interests include charge carrier processes in organic semiconductor devices and the integration of nanostructures in OLEDs.

Yolande Murat received the M.S. degree in material sciences and the Ph.D. degree in physics from the University of Bordeaux, France, in 2013 and 2017, respectively.

Since 2018, she has been a Postdoctoral Researcher with the Chair for Integrated Systems and Photonics, Kiel University, Germany. Her research interests are focused on printed electronics and organic electronics, including light-emitting diodes.

Martina Gerken (Member, IEEE) received the Dipl.Ing. degree in electrical engineering from the University of Karlsruhe, Germany, in 1998, and the Ph.D. degree in electrical engineering from Stanford University, Stanford, CA, USA, in 2003. From 2003 to 2008, she was an Assistant Professor with the University of Karlsruhe. In 2008, she was appointed as a Full Professor of Electrical Engineering and the Head of the Chair for Integrated Systems and Photonics, Kiel University, Germany.

4.2 Detection of Fluorescence-Labeled DNA with In-Plane Organic Optoelectronic Devices

4.2.1 Introduction

I. Titov, N. Rutschke, F. A. Kraft, M. Köpke, E. Nebling, and M. Gerken, "Detection of fluorescence-labeled DNA with in-plane organic optoelectronic devices," Biomedical Optics Express, vol. 13, no. 12, p. 6300, Dec. 2022, doi: 10.1364/BOE.475358.

Statement about the own contribution:

Conceptualization	Planning	Implementation	Manuscript preparation
High	High	High	High

- Design and modeling of the miniaturized OLED-OPD system for optical measurements.
- Implementation of the ray tracing simulation model and the investigations of the boundary conditions for an OLED-OPD design with optimized fluorescence excitation and detection efficiency.
- Estimation of the current system efficiency based on simulated and measured data.
- A comprehensive characterization of the fabricated OLED-OPD system on various setups. The spectral characteristics investigation was performed with an fluorescence microscope coupled to a spectrometer. The

OPD sensitivity and detectivity was investigated with a reflectometry-based setup and a laser diode. The limit-of-detection (LOD) was determined using Fluorescein and 6-FAM as fluorescence dyes.

- Planning, implementation and evaluation of hybridization sensing experiments based on fluorescence quenching mechanism with the synthesized ssDNA strands from Altona Diagnostics GmbH.

- Figure 3 and chapter 2.2 were provided by Nils Rutschke from Altona Diagnostics GmbH. The remaining part of the manuscript was written and revised by the first author.

4.2.2 Abstract

This paper presents the investigation of a sensing system for decentralized detection of biomarkers based on a specific EHV ssDNA assay and an optical detection unit with a side-by-side configuration of OLEDs and OPDs. The proof-of-concept of hybridization sensing of two complementary dye-labeled ssDNA strands diluted in TE buffer measured on a $12.5\,\mathrm{mm} \times 12.5\,\mathrm{mm}$ OLED-OPD chip with 8 integrated device pairs was successfully demonstrated. After the hybridization of the ssDNA segments to dsDNA the fluorophores undergo FRET, which results in a decreased fluorescence intensity. To characterize the system the LOD performance of $0.7\,\mathrm{mg\,L^{-1}}$ ($1.7\,\mathrm{\mu mol\,L^{-1}}$) for fluorescein was determined in water. For multiplex POC testing several specific biomarkers of interest can act as capture ssDNA, labeled with different fluorescence molecules. For this purpose, fluorescence-labeled ssDNA was covalently coupled on a glass surface, which was intended to act as sample capture molecule. However, the fluorescence of surface-bound biomarkers with the OLED-OPD chip could not been detected, hence a detailed investigation of the limiting factors in the current system was performed, based on further experiments and ray tracing simulations. The simulations show, that the highest light loss factors are due the wide emission angle of the OLED (approx. 97.3 %) (assumed a lambertian emission pattern) and the spherical losses of the fluorescence emission of the biomarkers (approx. 97 %). The highest experimental identified loss factor is the high light transmission rate of the fluorophores (approx. 97%). Nevertheless, the detection was demonstrated to be within the reach for improved OLED brightness, thinner substrates and optionally directly integrated light guiding elements, such as planar optical waveguides or air mirrors within the microfluidic structure [64, 65]. In summary, the developed monolithic in-

tegrated OLED-OPD sensing unit is now ready for biomedical detection of single-type dye-labeled ssDNA in solution [3].

4.2.3 Published Paper

Research Article | Vol. 13, No. 12 / 1 Dec 2022 / Biomedical Optics Express 6300

Biomedical Optics EXPRESS

Detection of fluorescence-labeled DNA with in-plane organic optoelectronic devices

IGOR TITOV,[1,*] NILS RUTSCHKE,[2] FABIO A. KRAFT,[1] MARKUS KÖPKE,[1] ERIC NEBLING,[3] AND MARTINA GERKEN[1]

[1]Integrated Systems and Photonics, Faculty of Engineering, Kiel University, Germany
[2]altona Diagnostics GmbH, Hamburg, Germany
[3]Battery Systems for Special Applications, Fraunhofer Institute for Silicon Technology, Germany
[*]igti@tf.uni-kiel.de

Abstract: We present a system efficiency analysis of a monolithic integrated organic optoelectronic unit for the detection of fluorescence labeled single-stranded DNA (ssDNA) for veterinary disease testing. The side-by-side integration of an organic light emitting diode (OLED) and an organic photodetector (OPD) with 0.5 mm by 0.5 mm device sizes has the potential to enable compact and low-cost fluorescence point-of-care (POC) devices for decentral multiplex biomedical testing. Here, we used two 6-FAM and BHQ1 labeled complementary ssDNA strands to form the Förster resonance transfer (FRET) upon the hybridization of the DNA. In this work we successfully show ssDNA hybridization sensing with samples diluted in TE buffer and investigate the detection of covalently bound 6-FAM-ssDNA on a glass surface for multiplex biomarker measurements.

1. Introduction

Equid herpesviruses (EHV) cause different diseases in equine population and have been reported in five variants named EHV-1 to 5. EHV-1 is the most pathogenic variant and is responsible for neurological and respiratory diseases, abortions as well as equine herpesvirus myeloencephalopathy (EHM) [1]. These severe equine diseases are often followed by loss of life, the inability to move horses and participate in equine races or competitions. Since the virus is transmitted by nose-to-nose contact or by fomites, it is essential to immediately separate the horses and establish quarantine to prevent closure of equine venues or equestrian farms as a consequence [2]. Both result in considerable economic cost to the owner and horse industry and require surveillance and prophylaxis. Thus, the detection of EHV is crucial and a variety of techniques have been reported for the diagnosis. Viral load can be collected in nasal swabs by using viral transport media for further quantification. The confirmation of viral identity can be realized by immunostaining or polymerase chain reaction (PCR) analysis after a virus isolation. Additionally, a nested PCR-enzyme-linked immunosorbent assay (ELISA) has also been reported to detect EHV infection. However, the stated detection techniques suffer from severe disadvantages: they are lab intensive and highly time consuming [3,4]. To overcome the aforementioned limitations lab-on-chip (LOC) systems for rapid point-of-care (POC) diagnosis are of high interest.

The current research aim is to develop a low-cost, widely available and simple to fabricate LOC biosensor for decentral EHV testing. The hybrid integration of organic light emitting diodes (OLEDs) and organic photodetectors (OPDs) promises great potential for highly integrated biosensors. Early work has achieved highly interesting results with the application of OLEDs and OPDs as wearable sensors for pulse oximetry or health monitoring [5–8] and several analytical applications [9,10] fabricated on flexible and rigid substrates. Mayr et al. [11], Pais et al. [12] and Liu et al. [13] presented fluorescence measurement systems based on the hybrid integration of OLEDs and OPDs. Recently Lian et al. [14] published very impressive results utilizing a microcavity OLED for detection of single-stranded DNA (ssDNA) of fetal bovine serum (FBS)

#475358 https://doi.org/10.1364/BOE.475358
Journal © 2022 Received 21 Sep 2022; revised 25 Oct 2022; accepted 26 Oct 2022; published 8 Nov 2022

Biomedical Optics EXPRESS

diluted in phosphate-buffered saline (PBS). Two complementary ssDNA labeled with Cyanine dyes were used to form a Förster resonance energy transfer (FRET) upon the hybridization of the ssDNA to double-stranded DNA (dsDNA). They excited the Cy3-dye with the OLED and detected the fluorescence of the Cy5-dye with an inorganic photodiode, achieving a low limit of detection (LOD) as 1 nM.

While the aforementioned reports are highly relevant, they are not easily upscaled for parallel fabrication of many sensor units. The sensing units are mostly fabricated on separate substrates with one type of optoelectronic device on it. The subsequent lamination to a single unit is liable to misalignment and thus not easy to upscale. To overcome this limitation we aim to develop a monolithic integrated OLED-OPD unit for biosensing applications. Integrating the optoelectronic detection unit on a single substrate is an essential step for ease of alignment and contacting and for the integration with a microfluidic system. Recently we demonstrated the fabrication of OLEDs and OPDs on one single flexible substrate in a matrix integration approach [15] and proposed recently 8 monolithic integrated OLED-OPD pairs with each device size of 0.5 mm * 0.5 mm for point-of-need (PON) nitrite sensing [16]. These detection units are based on thermal evaporation (PVD) device fabrication technique allowing a high degree of miniaturization and permanently aligned optical elements. On the longer term, the fabrication on flexible substrates is highly promising for roll-to-roll fabrication promising a new level of scalability and cost reduction [17,18]. In this work, we adapt the OLED stack for efficient excitation of the fluorophore 6-Carboxyfluorescein (6-FAM). This is a common label for biosensing. We investigate the light budget and efficiency for systems using OLEDs and OPDs integrated on a single substrate in a side-by-side configuration for the detection of fluorescence-labeled ssDNA. We present detection scenarios of fluorescence-labeled ssDNA with a filter-free design of a monolithic integrated OLED-OPD unit shown in the schematic of Fig. 1.

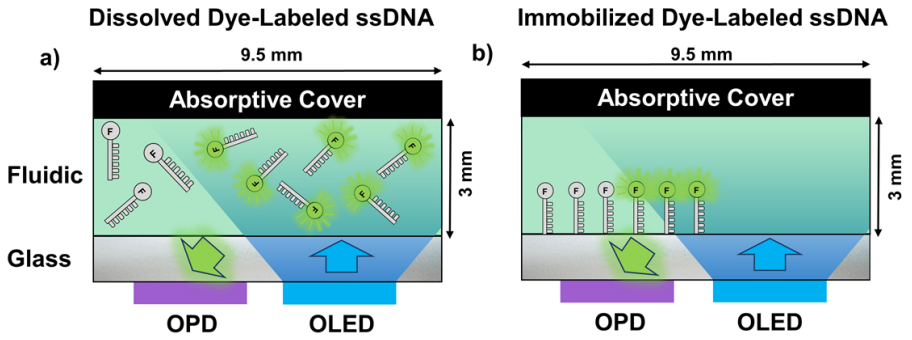

Fig. 1. Schematic view of the analyzed sensing scenarios with the investigated monolithic integrated OLED-OPD unit for detection of fluorescence dye-labeled ssDNA; (a) Sensing of dissolved fluorescence dye-labeled ssDNA in a buffer solution. The fluid chamber contains approx. 270 µl analyte with a certain concentration of dye-labeled ssDNA; (b) Sensing of surface bound dye-labeled ssDNA on a glass substrate.

In the first detection scenario we investigate the sensitivity of sensing fluorescence-labeled ssDNA free diffusive in TE buffer (Fig. 1(a)). The OLED excites the dissolved randomly-orientated fluorescence molecules in a liquid chamber with a volume of approx. 270 µl. The top of the fluidic is covered with a black absorptive polymer cover, to avoid light scattering directly from the OLED to the OPD. We discussed the suppression of stray light using black microfluidic chambers in our previous work [15]. Secondly, we investigate a detection setup with surface bound dye-labeled ssDNA utilized as capture molecules (Fig. 1(b)). Here, we developed a specific ssDNA assay based on the fluorescence quenching mechanism. We covalently coupled

Biomedical Optics EXPRESS

a fluorescence-labeled ssDNA on a glass surface, which is intended to act as a capture molecule. The detection principal bases on the hybridization of the fluorescence-labeled ssDNA strand and a quencher-labeled reverse complementary ssDNA segments, where the fluorescence of the fluorophore is suppressed upon a certain proximity to the quencher [19,20]. After the hybridization of the ssDNA segments to dsDNA the fluorophores undergo FRET. This setup is highly relevant for multiplex measurements. For testing of several specific biomarkers of interest, capture ssDNA can be labeled with different fluorescence molecules. This results in a specific wavelength for certain biomarker, which can be excited and detected with a suitable OLED-OPD pair.

The paper is structured as follows. In section 2 we present the synthesis and the detection principal of the fluorescence-labeled ssDNA and the fabrication and characterization of the OLED-OPD detection unit. Section 3 describes our results with three different measurement setups. Firstly, we show a successful fluorescence quenching of surface bound fluorescence-labeled ssDNA on a fluorescence microscope. Secondly, we show a compact measurement system containing a laser diode as the excitation source and an OPD as the detector. Here we obtained an LOD of 63 µg/l (150 nM) for fluorescein in water and performed successfully DNA hybridization detection. Next, we show the detection of fluorescence-labeled ssDNA on a compact, monolithic integrated OLED-OPD unit with an LOD performance of 0.7 mg/l (1.7 µM) for fluorescein in water. Finally, we give an estimation of the system efficiency by performing ray tracing simulations and verify the theoretical results with experimental measurements. Conclusions are given in section 4.

2. Experimental section

2.1. Chemicals and materials

Following materials were used as the organic components of the devices: 1,1-bis[(di-4-tolylamino)phenyl]cyclohexane (TAPC, CAS-No: 58473-78-2, Merck KGaA, Darmstadt, Germany), tris(4-carbazoyl-9-ylphenyl)amine (TCTA, CAS-No: 139092-78-7, Merck KGaA, Darmstadt, Germany), 2,2',2''-(1,3,5-Benzinetriyl)-tris(1-phenyl-1-H-benzimidazole) (TPBi, CAS-No: 192198-85-9, Luminescence Technology Corp., New Taipei City, Taiwan), Bis[2-(4,6-difluorophenyl)pyridinato-C2,N](picolinato)iridium (FIrPic, CAS-No: 376367-93-0, Ossila Ltd, Solpro Business Park, Windsor Street, Sheffield S4 7WB, U.K.), N,N-Dimethyl quinacridone (DMQA, CAS-No: 19205-19-7, Lumtec), 3',4'-Dibutyl-5,5''-bis(dicyanovinyl)-2,2':5',2''-terthiophene (DCV3T, CAS-No: 908588-68-1, Luminescence Technology Corp., New Taipei City, Taiwan), molybdenum trioxide (MoO_3, CAS-No: 1313-27-5, Merck KGaA, Darmstadt, Germany), lithium fluoride (LiF, CAS-No: 7789-24-4, Merck KGaA, Darmstadt, Germany), aluminum (Al, CAS-No: 7429-90-5, Merck KGaA, Darmstadt, Germany).

2.2. Synthesis of ssDNA for hybridization sensing

The chemical synthesis of modified ssDNA was done using the phosphoramidite method on a solid phase. The nucleotides were added in a cyclic process to the start nucleotide or 3' modification which were bound to a solid phase consisting of Controlled Pore Glass (CPG). During the process, the functionalized groups of phosphates, desoxyribose and nucleobases needed to be temporarily or permanent encapsulated to avoid unwanted side reactions. In the final stage of oligonucleotide synthesis, the oligonucleotide was cleaved from the CPG. The cycle is displayed in Fig. 2.

The synthesis was executed on a DNA/RNA Synthesizer ABI 3900 (Biolytic Lab Performance, Inc., Fremont, USA). The purification of the target ssDNA was carried out by a Reversed Phase Ion Pairing Chromatography (Chromaster, Hitachi High-Tech, Tokio, Japan) in combination with a fractionator (Foxy R2, TELEDYNE ISCO, Inc., Lincoln, USA) according to the hydrophobicity

Biomedical Optics EXPRESS

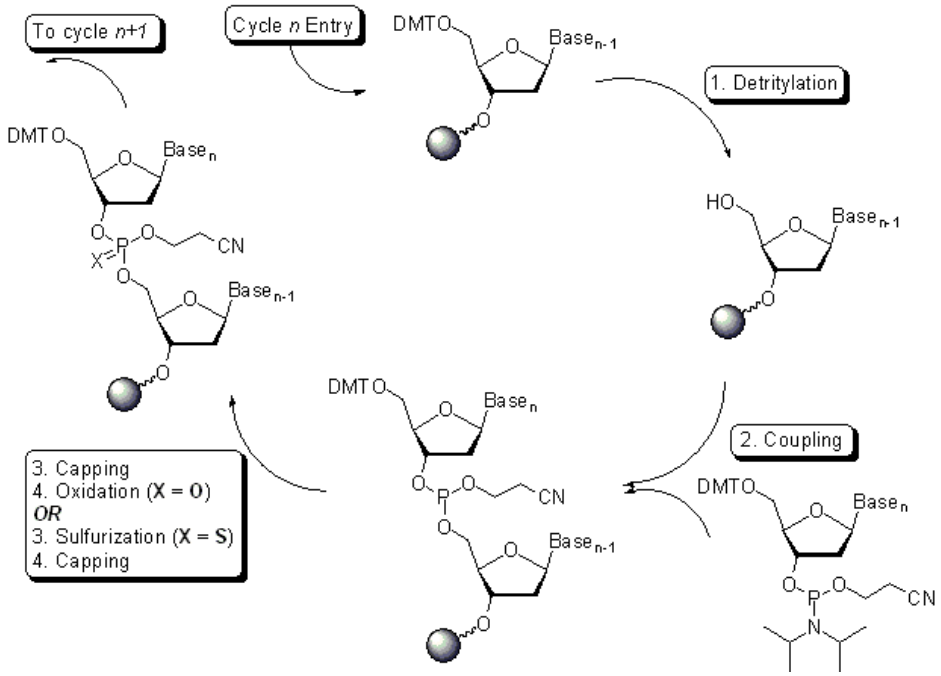

Fig. 2. The phosphoramidite ssDNA synthesis cycle.

and ionic character [21]. The dye-labeled ssDNA sequences were synthesized at altona Diagnostics GmbH and obtained with an initial concentration of 100 µM in TE-buffer.

2.3. Detection principle of 6-FAM-labeled ssDNA

This section focuses on the fluorescence detection principle, after an isothermal amplification reaction. For the target sequence two primers are used, one of the primers is modified with an internal black hole quencher (BHQ1) and a secondary structure. This secondary structure should prevent false positive results and is only unwound when the target sequence is present and amplified (Fig. 3). In case of a successful amplification, the double stranded amplicon is generated with a short single stranded (ss)DNA tail (Fig. 3). This DNA tail is designed to fit to a single stranded reverse complementary capture molecule in another compartment of chip.

For further immobilization of capture molecules we functionalized a glass surface with 3-aminopropyltriethoxysilane (APTES) and modified the amino-silane groups by subsequent adding of *bis*-NHS-PEG compounds. This procedure leads to a crosslinker with homobifunctional NHS-ester compounds for protein interactions [22]. In Fig. 4(a) schematic representations of the APTES and *bis*-NHS-PEG_5 surface functionalization are shown with a verification photograph of a spot (Fig. 4(b)) after successful immobilized fluorescence-labeled ssDNA, visualized on a fluorescence microscope (Leica DMi8, Leica Microsystems CMS GmbH, Wetzlar, Germany).

The capture molecule is immobilized on a glass surface via an amine group at its 5'-End. At the 3'-End the fluorophore 6-Carboxyfluorescein (6-FAM) is orientated (Fig. 5(a)). The detection principal bases on the Förster resonance energy transfer (FRET), where the fluorescence of the fluorophore is suppressed when it is in a certain proximity to the quencher.

Biomedical Optics EXPRESS

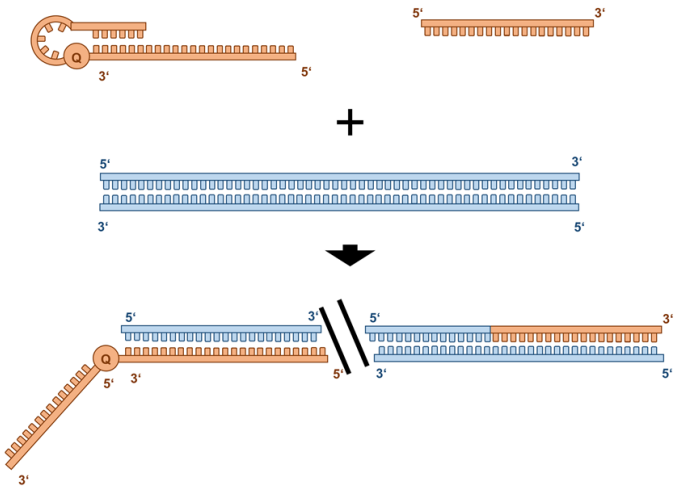

Fig. 3. Isothermal amplification reaction: Specific primer binds to double stranded target sequence, which is accessible due to DNA associated proteins. In the next step an isothermal Polymerase elongates the primer and generates with each amplicon a product with a ssDNA tail. This ssDNA tail is reverse complementary to the capture molecule immobilized on the glass surface. The amplification reaction is continued until one of the reaction components is imitating.

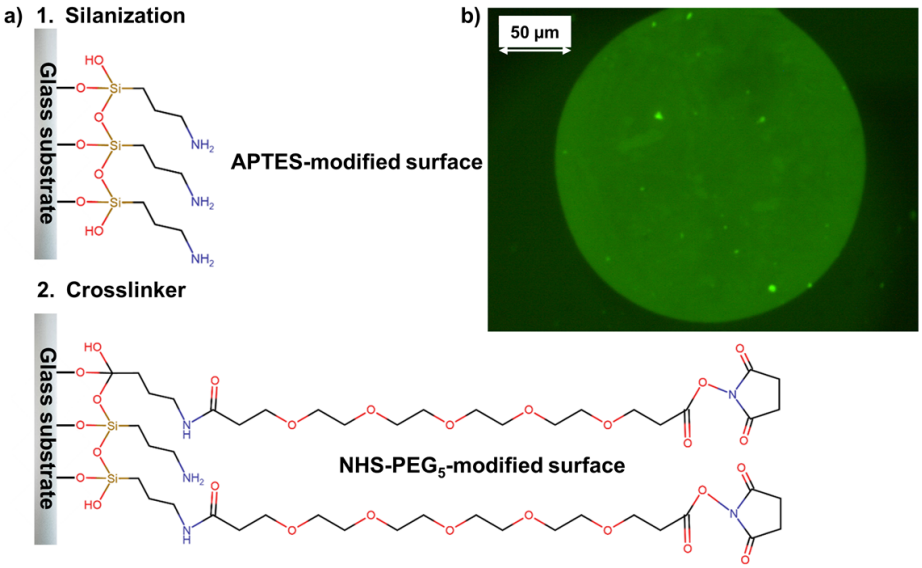

Fig. 4. (a) Schematic of the APTES-modified glass surface functionalization with bis-NHS-PEG_5 crosslinker for coupling proteins on the NHS ester terminals; (b) Resulting photograph of a spot with fluorescence (6-FAM)-labeled ssDNA tails.

Biomedical Optics EXPRESS

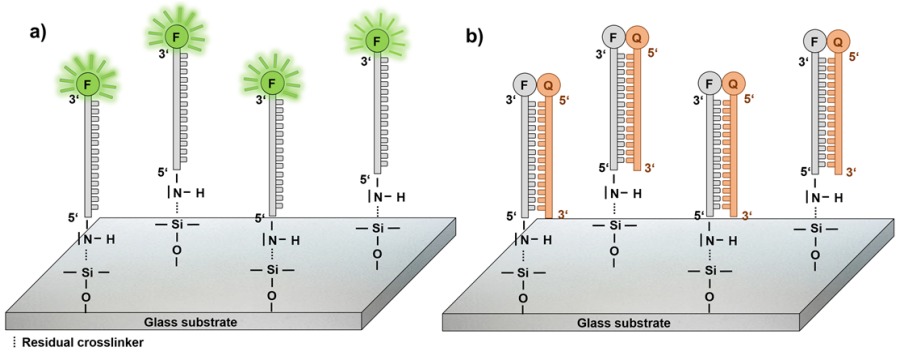

Fig. 5. a) Schematic of immobilized capture molecules; b) Binding of ssDNA tail of target amplicon to immobilized capture molecule and the resulting fluorescence quenching.

2.4. OLED-OPD detection unit fabrication and device characterization

Figures 6(a,b,d) show the organic stacks, a geometrical schematic and a photograph of the test chip with 8 OLED-OPD detection units. The realized TCTA:FIrPic OLEDs and DMQA:DCV3T OPDs are fabricated on a 25 mm × 25 mm glass substrate with a thickness of 1 mm. Each substrate contains 4 test chips, which are separated afterwards to 12.5 mm × 12.5 mm sensing units by a wafer saw. Here, each test chip has 8 OLED-OPD detection units with each device size of 0.5 mm * 0.5 mm. The blue emitting OLED (peaking at ~468 nm and ~494 nm) pixels fabrication was carried out on indium-doped tin oxide (ITO) covered glass by thermally evaporating organic materials. The ITO layer was structured via ultraviolet (UV) photolithography and wet etching to form the 130 nm thin anodes. The organic layers, in sequence, are the hole transport layer of 5 nm molybdenum trioxide (MoO3) and 35 nm 1,1-bis[(di-4-tolylamino)phenyl]cyclohexane (TAPC), then for the emission layer a 20 nm of tris(4-carbazoyl-9-ylphenyl)amine (TCTA) doped with 8% Bis[2-(4,6-difluorophenyl)pyridinato-C2,N](picolinato)iridium (FIrPic) to fabricate a blue emitting OLED. As the electron transport layer (ETL) and hole blocking layer (HBL) a film of 50 nm 2,2',2''-(1,3,5-Benzinetriyl)-tris(1-phenyl-1-H-benzimidazole) (TPBi) is deposited followed by the cathode pads consisting of 1 nm lithium fluoride (LiF) and 175 nm aluminum (Al). Consequently, the OLED pixels are defined by the overlapping regions of mutually perpendicular ITO and Al pads. The OPD structure starts with 30 nm molybdenum trioxide (MoO_3) layer deposited on the indium-tin-oxide (ITO) coated glass. The organic bilayer structure is composed of 30 nm N,N-Dimethyl quinacridone (DMQA) as the common donor and 30 nm 3',4'-Dibutyl-5,5''-bis(dicyanovinyl)-2,2':5',2''-terthiophene (DCV3T) as the acceptor layer. Next, 8 nm 2,2',2''-(1,3,5-Benzinetriyl)-tris(1-phenyl-1-H-benzimidazole) (TPBi) was evaporated followed by 1 nm lithium fluoride (LiF) and 175 nm aluminum (Al) to form the cathode pads. The fabricated devices were encapsulated in a nitrogen-filled glovebox to prevent degradation of the organic layers upon measurements outside the glovebox [16]. Figure 6(c) shows the normalized photoluminescence spectrum of the OLED, with an excitation wavelength peaks at 468 nm and 494 nm, the spectrum of the OPD with the DMQA:DCV3T absorptive bilayer and the spectra of the 6-FAM dye with an excitation and emission wavelength of approx. 496 nm and 521 nm, respectively. The electrical characterization of the OPD is shown in Fig. 6(e). We performed the current-voltage measurement sweep by a source measure unit (SourceMeter 2450, Keithley Instruments, USA) while illuminating the device with a collimated laser module (CPS520, 4.5 mW, Thorlabs GmbH, Lübeck, Germany). The OPD displays a typical diode characteristic with a good sensitivity. The darkcurrent density at 0 V was determined as 15 nA/cm^2 and approx. 0.7 mA/cm^2 are obtained for an incident light power of approx. 0.8 mW/cm^2.

Biomedical Optics EXPRESS

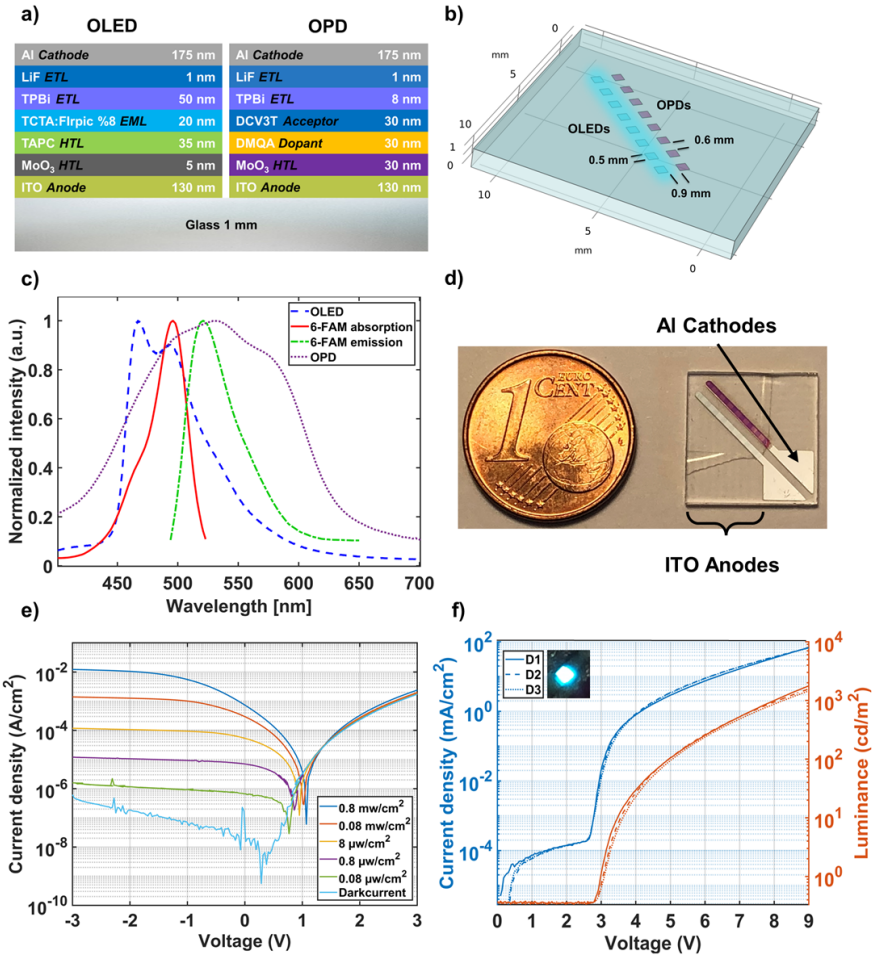

Fig. 6. Fabrication of the OLED-OPD unit for fluorescence sensing. (a) Schematic diagram of the OLED and OPD stacks on a single glass substrate; (b) Geometrical model of the OLED–OPD unit layout with 8 pixel pairs on one test chip; (c) Normalized absorption and emission of 6-FAM [23] and the spectral characteristics of 8 wt% FIrPic in TCTA host OLED emission and the DMQA:DCV3T OPD absorption; (d) Photograph of the fabricated test chip; (e) Current density-voltage characteristics under illumination with a subsequently filtered 520 nm laser and the darkcurrent of the DMQA:DCV3T OPD as an example; (f) J-V-L characteristics of 3 different devices (D1, D2 and D3) as an example.

Biomedical Optics EXPRESS

The OLED was characterized using a commercial calibrated Si-photodiode (FDS1010 Cal, Thorlabs GmbH, Lübeck, Germany) and two source measure units (SourceMeter 2450 & 2400, Keithley Instruments, Cleveland, USA). We placed the light source on top of the large-area photodiode and collected the outcoupled light. Hence, we calculated the current density and the luminance (Fig. 6(f)) with the recorded OLED current and the photocurrent induced by the OLED. We performed all further calculations considering the whole OLED spectrum by multiplying the sensitivity curve of the calibrated Si-PD with the normalized OLED spectrum and the subsequent integration of the relevant wavelength. The onset voltage is approximately 3 V. The measurement was performed with 3 different devices in sequence and shows a good reproducibility. The inset shows a photograph of the 0.5 mm * 0.5 mm OLED pixel operated at 9 V. Here we achieved a luminance of ~1700 cd/m^2 and a current density of 70 mA/cm^2 at 9 V. Additionally, we obtained a maximum current efficiency η of 2.7 cd/A. Due to our observation of a damage threshold voltage between 10 V and 12 V for our devices, we decided to apply 9 V as the operation voltage.

3. Fluorescence sensing setups for ssDNA detection

3.1. 6-FAM-labeled ssDNA characterization on a fluorescence microscope

As the first step towards a compact fluorescence sensing setup we started our experiments with a characterization of our samples on a fluorescence microscope. In this study we evaluated the feasibility of immobilization of capture molecules by measuring the fluorescence after application and washing. Subsequently, we added the ssDNA hosting a quencher, to simulate whether this part of the target amplicon would fit to the capture molecule. In case of a successful binding 6-FAM and the quencher BHQ1 will undergo FRET. Consequently, we expect a suppression of fluorescence.

Figure 7 shows a verification photograph and the spectra of 6-FAM labeled ssDNA spots on a glass substrate after successful binding of fluorescence-labeled ssDNA. We used a spotter (Nanoplotter 2.0, GeSiM Gesellschaft für Silizium-Mikrosysteme mbH, Germany) to fabricate 9 homogeneous spots with each diameter of 200 µm and 200 µm space between the single spots (Fig. 7(a)). Figure 7(b) shows the spectra of 6 randomly picked spots across one fabrication batch. The shape of the spots is highly homogeneous, whereas the fluorescence intensity varies up to a factor of 2. The variability could be further reduced by optimization of the surface functionalization. However, here our aim is to analyze the measurement system aspects and the functionalization is not studied further. As a verification of the hybridization sensing mechanism we investigated the behavior of one single 6-FAM-labeled ssDNA spot, as shown in Fig. 7(c). Here, we took one picture before and one after the application of the complementary BHQ-labeled ssDNA strand in TE buffer as a drop. The second picture shows a successfully quenched area with a fully suppressed fluorescence spot at the location of the applied quencher drop. Thus, this results show readiness off the assay for detecting EHV on a fluorescence microscope.

3.2. Laser excitation of 6-FAM-labeled ssDNA and detection on OPD

Towards a compact fluorescence measurement system we implemented in the first step a laser and OPD based setup, as depicted in the schematic of Fig. 8(a). The 6-FAM-labeled ssDNA sample was diluted in TE buffer solution. We used DNase, DNA and RNase free micro cuvettes as sample holder. We chose a 488 nm laser diode (BLD-488-58, Lasertack GmbH, Germany) as the light source, a collimating lens and a 480 nm bandpass filter on the excitation side. On the detection side we implemented a DMQA:DCV3T OPD with a preceding lens and a 527 nm bandpass filter to avoid the excitation light reaching the detector. Additionally, we used a dichroic mirror for splitting of the excitation light and the fluorescence and performed the experiments in a dark environment.

Biomedical Optics EXPRESS

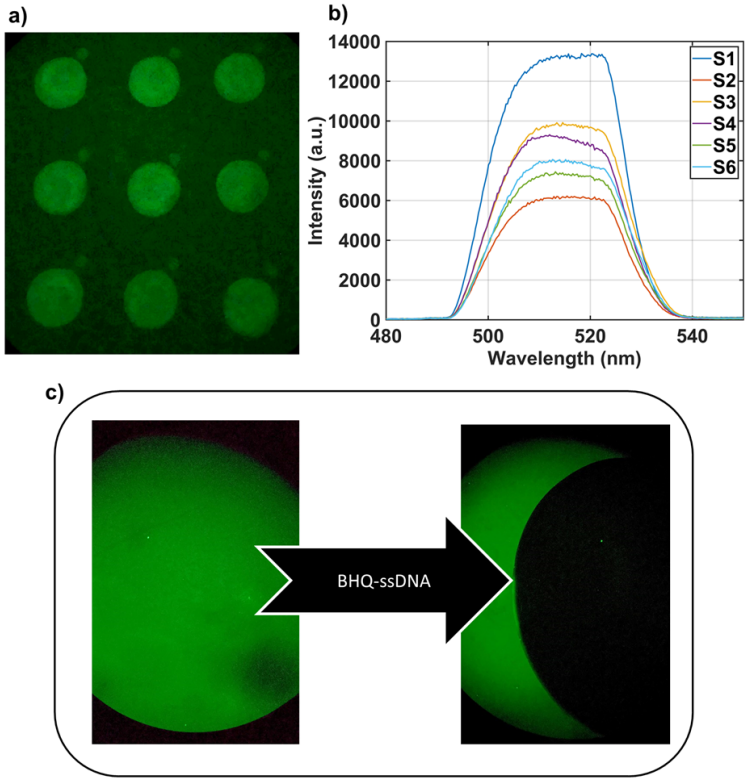

Fig. 7. (a) Photograph of 9 6-FAM-labeled ssDNA spots with each spot diameter of approx. 200 µm made on a fluorescence microscope; (b) Spectral characteristic of 6 random chosen spots as an example; (c) Photograph of a 6-FAM-labeled ssDNA spot, before and after applying a BHQ drop. After the hybridization to dsDNA the FRET based quenching process can clearly be observed by forming a dark spot as seen in the right picture.

Figure 8(b) shows a photograph of the investigated labeled ssDNA samples. The left cuvette contains the 6-FAM-labeled ssDNA, which shows the characteristically green emission of the fluorescent molecules. The right cuvette contains a 50/50 (wt/wt) mixture of 6-FAM-labeled ssDNA and the complementary BHQ-labeled ssDNA, both in 8.45 µM. As expected FRET was successfully observed even with the naked eye. The fluorescence gets suppressed after the hybridization to dsDNA and the resulting proximity of the 6-FAM and BHQ molecules. In the next step we evaluated the sensing performance of our laser diode and OPD based measurement setup. Figure 8(c) shows the fluorescence measurement, starting with 5 premixed fluorescein standard samples in cuvettes ranging from 2 mg/l to 10 mg/l. We illuminated every sample for 40 s and recorded the photocurrent on the OPD. The signal peak at the beginning of each sample is based on diffuse reflection of the laser light due to the manual change of the cuvettes and can be neglected. The observed increase of the photocurrent upon the increase of the fluorescein concentration is shown for the first 5 samples. Furthermore, we also observed a strong photo bleaching of the fluorescein, due to the illumination of the sample with the laser. Hence, we obtained the calibration function by taking the last measurement point for each fluorescein standard signal. We calculated the sensitivity as $S = 1$ nA/(mg/l) offering a linearity of approx. 99%. The standard deviation of the current noise level is determined as $\sigma = 21$ pA. This yields

Biomedical Optics EXPRESS

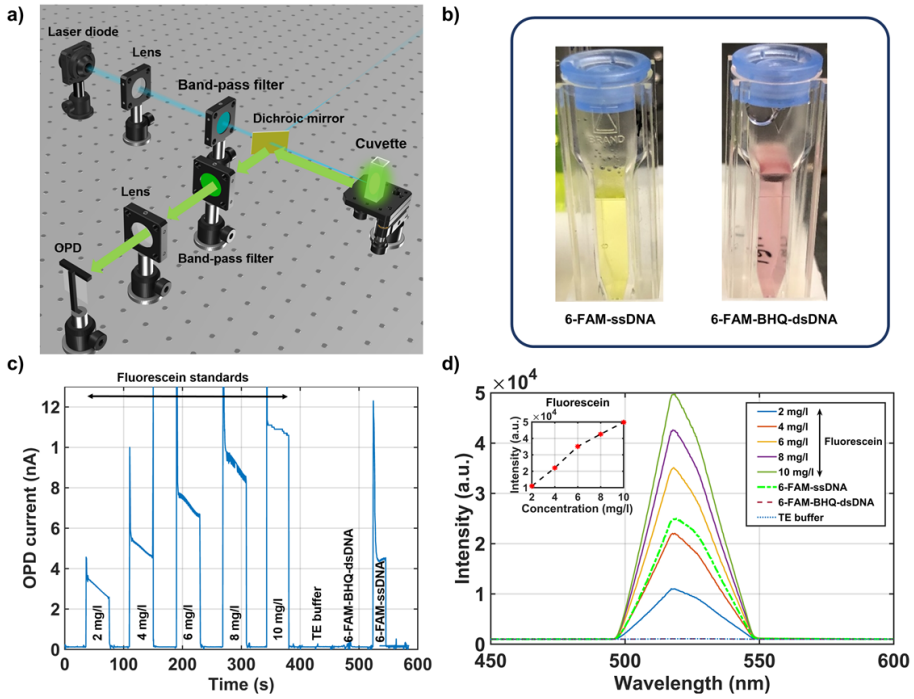

Fig. 8. (a) Schematic diagram of the fluorescence sensing setup based on a laser diode as the excitation source and an OPD as detector; (b) Photography of 6-FAM labeled ssDNA sample diluted in TE buffer (left) and a 6-FAM labeled ssDNA sample mixed with the complementary BHQ1 labeled ssDNA quencher system; (c) Fluorescence measurement of premixed fluorescein standards and bio-samples; (d) Spectral characteristics of the measured samples. The inset shows a linear behavior of the fluorescein standards.

a limit of detection (LOD) of LOD = 3×σ/S = 63 µg/l (150 nM). Next, we proceeded with the DNA hybridization measurements. As shown in Fig. 8(c) we recorded in the last 3 measurements subsequently the resulting OPD photocurrent of a cuvette with TE buffer, a cuvette with a 50/50 (wt/wt) mixture of 6-FAM-labeled ssDNA and the BHQ-labeled ssDNA (as depicted in Fig. 8(b) right) and a cuvette of the 6-FAM-labeled ssDNA. The concentration of the ssDNA samples was always fixed at 8.45 µM. This measurement also confirms that the hybridization of the ssDNA strands to dsDNA takes place with subsequent FRET based fluorescence quenching. Furthermore, we excluded any influence of the laser induced light on the OPD by testing the clear TE buffer sample. This reference measurement is seen in Fig. 8(c) at around 420 s. No signal is observed on the OPD. Thus, the combination of the excitation and emission filters with the dichroic mirror allows a strong suppression of undesired background signal in the measurements. As a verification of the measurements we checked the spectral characteristics of the investigated samples prior to the laser measurements. As depicted in Fig. 8(d) the fluorescein standard solutions and the 6-FAM-labeled ssDNA show the expected emission peak at approx. 520 nm. The quenched sample and the TE buffer show no fluorescence intensity. These results show that using a laser diode and an OPD has a high potential to be employed in compact systems for DNA hybridization measurements. However the process of integrating a laser diode and an OPD as a LOC system cannot easily be upscaled for parallel fabrication of many sensor units. Thus,

Biomedical Optics EXPRESS

we investigate DNA hybridization sensing on a full organic optoelectronic chip with in-plane integrated devices in the following chapter.

3.3. Fluorescence sensing with the OLED-OPD detection unit

As the next step towards POC testing we used our OLED-OPD chip for fluorescence sensing. Figure 9(b) shows an exploded-view schematic of the detection setup. We contacted the OLED-OPD chip (Fig. 6(b,d)) with elastomeric ZEBRA connectors, using a printed circuit board (PCB) with mirrored electrodes design. The OLED-OPD chip and the PCB are pressed with caps and the housing to ensure electrical contact and prevent displacement. The fluid chamber is sealed with a rubber seal (9.5 mm by 9.5 mm by 3 mm) to ensure tightness and avoid leakage of the liquid samples resulting in a volume of approx. 270 µl. Two butterfly cannulas were used to form the in- and outlets. They are punched through the rubber into the chamber. Figure 9(c) shows a photograph of the setup. The measurements were performed with two source-measure units (SMUs) for OLED power supply and recording the photocurrent of the OPD. To characterize the system we performed a fluorescence measurement with a dilution series of fluorescein again ranging from 2 mg/l to 10 mg/l. Figure 9(a) shows the OPD photocurrent as a function of dye concentrations. Every 100 s we changed the analyte to investigate the photocurrent change between DI water and the increasing fluorescein concentration. The inset of the plot shows the background corrected staircase shaped increasing signal, due to the increased fluorescence signal. For example, the absolute photocurrent changed to 0.18 nA after addition of a 10 mg/l fluorescein standard solution. The calibration function obtained from these measurements was found to be linear within the tested region, offering linearity of approximately 99%. The sensitivity was calculated as S = 10 pA/(mg/l). The standard deviation current noise level was determined as $\sigma = 3$ pA. This yielded a limit of detection (LOD) of $\mathrm{LOD} = 3 \times \sigma/S = 0.7$ mg/l (1.7 µM). Pais et al. [12] reported a transmission based setup with an OLED and an OPD fabricated on separate substrates and two orthogonally orientated polarizers to filter out the excitation light. They obtained an LOD of 10 µM for fluorescein, which shows that our OLED-OPD unit already show a better performance by approx. a factor of 6. Finally, we proceeded with the ssDNA hybridization sensing. In Fig. 9(d) we show the fluorescence signal under OLED excitation of 6-FAM-ssDNA and premixed 6-FAM-BHQ-dsDNA with fixed concentrations at 8.45 µM. The inset of the figure shows the original data with the typical degradation behavior of the OLED. For 6-FAM-ssDNA the OPD photocurrent increases due to the fluorescence of 6-FAM and drops for approx. 0.14 nA after flushing the chamber with the premixed 6-FAM-BHQ dsDNA. Figure 9(d) shows the background corrected measurement.

These results show successful DNA hybridization sensing on a fully organic-semiconductor-based in-plane integrated sensor. We believe that this OLED-OPD detection unit is a highly relevant first step towards the realization of compact, low-power point-of-care devices in the veterinary or human diagnostic.

Our long-term goal is the realization of multiplexed detection by specific binding of fluorescence-labeled biomaterial. For example, our OLED-OPD chip design with 8 OLED-OPD pairs is a suitable POC system for testing of four different biomarkers with a reference site each. By local functionalization this would allow eight simultaneous measurements on one single chip without the need for wavelength multiplexing. To test this idea, we prepared a series of glass slides with immobilized 6-FAM-ssDNA strands as capture molecules as shown in Fig. 7(a). The goal was to excite the 6-FAM-ssDNA spots with the OLEDs and measure the FRET after adding BHQ-ssDNA. In this set of experiments, the OLED-OPD detection unit showed no signal change after applying a BHQ-labeled ssDNA drop even though the fluorescence microscope showed clear and successful binding of 6-FAM-ssDNA on the glass slides. The fluorescence emission of the 6-FAM-labeled monolayer of surface bound capture molecules provide weaker fluorescence signal, due to the smaller absolute amount of fluorophores inside the fluidic chamber compared to

Biomedical Optics EXPRESS

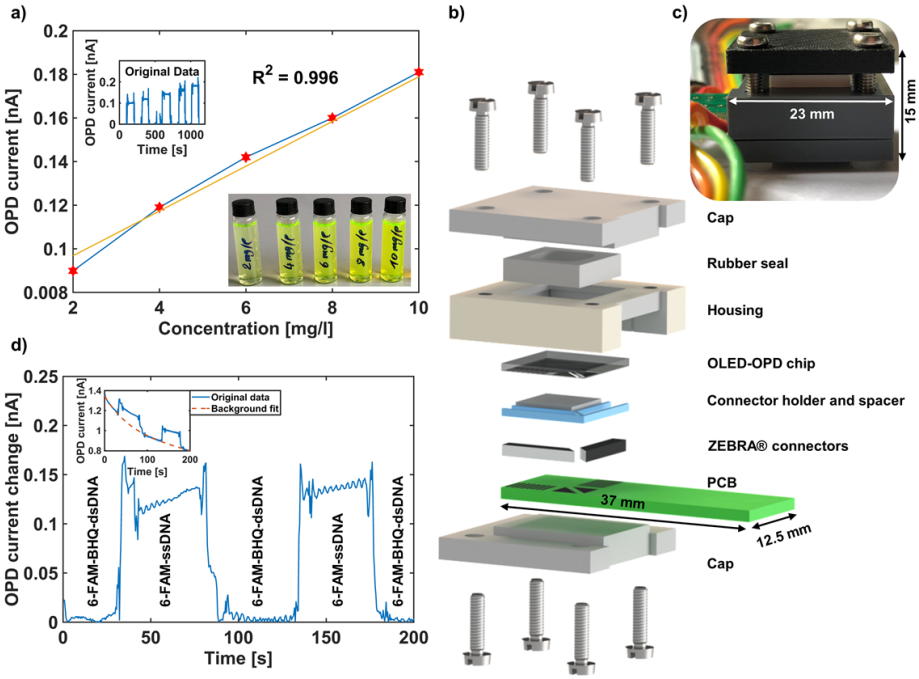

Fig. 9. (a) Photoresponse of the OPD for the dilution series of fluorescein dye with OLED excitation. The inset shows the original data and the main plot represents the amount of photocurrent induced on the corresponding fluorescein concentration; (b) Exploded-view drawing of the detection setup. The OLED-OPD chip is contacted with elastomeric ZEBRA connectors, using a printed circuit board (PCB) with mirrored electrodes design. The OLED-OPD chip and the PCB are pressed with a cap and the housing to ensure electrical contact and prevent displacement. The fluid chamber is sealed with a rubber seal; (c) Photograph of the detection unit; (d) Fluorescence measurement of the 6-FAM-ssDNA and the hybridized 6-FAM-BHQ-dsDNA samples as liquids with fixed concentration at 8.45 µM. The inset shows the original data and the typical degradation of the OLED during the operation.

Biomedical Optics EXPRESS

the measurement with higher concentrated liquid samples. Thus, the signal-to-noise ratio of our OLED-OPD detection unit is not sufficient yet for detection of immobilized DNA hybridization sensing. In the next chapter we investigate the system efficiency in order to give a feasibility analysis.

3.4. System efficiency and light budget of the OLED-OPD detection unit

3.4.1. Raytracing simulations

To evaluate the current system efficiency we conducted ray tracing simulations with the Ray Optics Module in COMSOL Multiphysics. In the first simulation we investigate the efficiency of the 6-FAM-ssDNA spot excitation by the OLED. We assume that the OLED releases the emission power with a Lambertian emission pattern directly from the semitransparent ITO anode layer, which gets partly absorbed by the fluorescence dye spot modeled as a ray detector. The wavelength was fixed at 495 nm, since our hybridization sensing assay was developed based on 6-FAM as the fluorescence dye. We located the spot above the OPD in our model (Fig. 10(a,b)) with the same size of active region as the photodetector to achieve the highest fluorescence intensity upon a successful excitation of the fluorescence spot. As the total OLED emission power we obtained $J_{OLED} = 3.5$ mW/cm^2 (active area of 0.25 mm^2 as reference) operating the OLED at 9 V and using a calibrated Si-PD and considered this value in our simulations. Finally, the excitation power on the spot was simulated as $E_{SPOT} = 95$ µW/cm^2. We calculate that only $\eta_{Ill} = 2.7\%$ of initial OLED emission power reach the fluorescence spot, which is due to the small solid angle of the fluorescence spot as viewed from the OLED. Figure 10(b) shows a sideview of a simulation snapshot with our OLED-OPD model. Most of the OLED light does not reach the fluorescence spot.

In the next simulation step, we consider how much fluorescence emission reaches the OPD. To estimate the initial fluorescence emission power we prepared a glass slide fully covered with surface bound 6-FAM-ssDNA and measured the transmission spectrum with a UV-Vis spectrometer (Lambda 800, PerkinElmer, USA). The absorption around 496 nm was measured to be approx. $\eta_{Abs} = 3\%$. Additionally, we considered the quantum yield of $\eta_{QY} = 95\%$ for fluorescein [24] and calculated the energy conversion efficiency of $\eta_{\Delta E} = \lambda_{Ex}/\lambda_{Em} = 95.2\%$ due to the wavelength shift from 496 nm to 521 nm. Considering all factors leads to a total fluorescence efficiency at the spot of $\eta_{Fl} = \eta_{Abs} * \eta_{QY} * \eta_{\Delta E} = 2.7\%$. Thus, we defined the fluorescence spot in the next step of our simulation as a spherical ray release device (Fig. 10(a)) with a source emission power of $J_{SPOT} = E_{SPOT} * \eta_{Fl} = 2.6$ µW/cm^2. Due to the small solid angle, the OPD detected approx. $\eta_{Det} = 1.8\%$ of the initial released rays resulting in an OPD irradiance of $E_{OPD} = J_{SPOT} * \eta_{Det} = 46$ nW/cm^2. According to our simulations the system efficiency of the OLED emission power to OPD irradiance with the fluorescence emission of the dye spot is calculated to be approx. $\eta_{Sys} = E_{OPD} / J_{OLED} = 0.013‰$. The simulation results are summarized in Table 1.

Table 1. System Efficiency Simulation

Simulation Benchmarks	Determination	Efficiency Factor	Value
OLED emission power density J_{OLED}	Measured	-	3.5 mW/cm^2
6-FAM-ssDNA spot illumination E_{SPOT}	Simulated	$\eta_{Ill} = E_{SPOT} / J_{OLED}$	95 µW/cm^2
6-FAM-ssDNA emission power density J_{SPOT}	$E_{SPOT} * \eta_{Fl}$	$\eta_{Fl} = \eta_{Abs} * \eta_{QY} * \eta_{\Delta E}$	2.6 µW/cm^2
Fluorescence radiation on OPD E_{OPD}	Simulated	$\eta_{Det} = E_{OPD} / J_{SPOT}$	46 nW/cm^2
System efficiency	E_{OPD}/J_{OLED}	η_{Sys}	0.013‰

As a conclusion, the simulated low system efficiency of $\eta_{Sys} = 0.013‰$ is attributed to three dominant loss factors – the low irradiation of the 6-FAM-ssDNA spot by the OLED, the low irradiation of the OPD by the fluorescence emission of 6-FAM-ssDNA, and the high transmission

Biomedical Optics EXPRESS

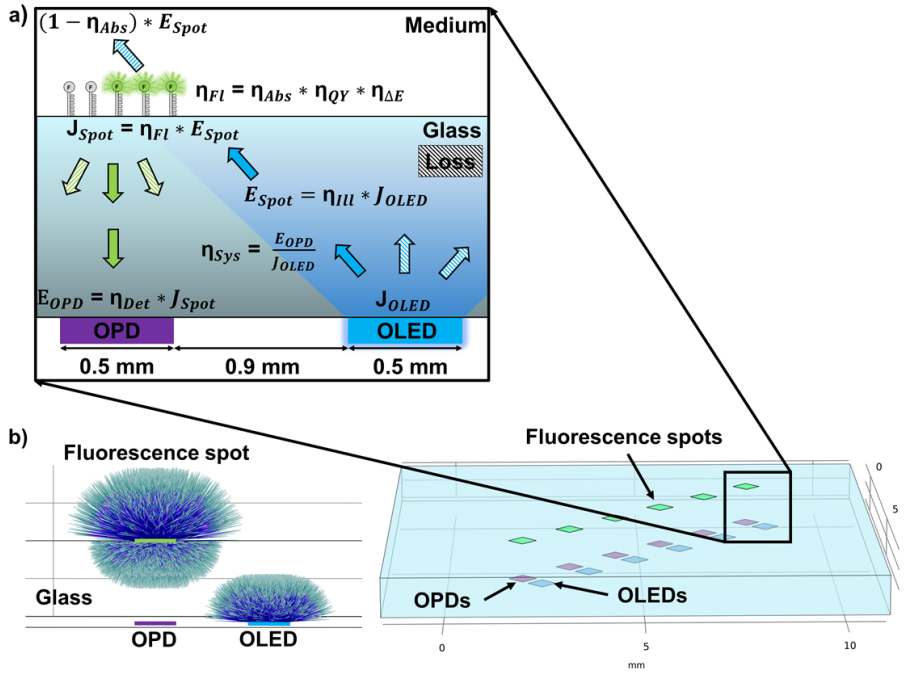

Fig. 10. Ray-Tracing simulation model. (a) 3D view of the full OLED-OPD unit model with 8 pixel pairs on one substrate. The 6-FAM-labeled-ssDNA spots are placed above the OPDs. The zoomed inset shows a 2D schematic, the efficiency factors and the geometrical properties of one OLED-OPD pixel pair and the fluorescence spot; (b) Sideview of an OLED-OPD pair model with a fluorescence spot above the OPD. The OLED was modeled as a Lambertian emitter and the fluorescence spot as a spherical ray release source.

through the monolayer of 6-FAM-ssDNA capture molecules. The first two factors are due to the geometrical losses of the monolithically integrated OLED-OPD system. The geometrical losses are visualized in the Fig. 10(b) as a plot that shows a snapshot of the simulated ray trajectories of one OLED and one fluorescence spot. The picture shows clearly the high fraction of excitation rays, which do not arrive at the fluorophore, and fluorescence rays not reaching the OPD. Thirdly, the monolayer of 6-FAM-ssDNA capture molecules transmits approx. 97% (1-η_{Abs}) of incident light. In Table 2 we summarized all considered loss factors and highlighted the dominant ones, which can be minimized with a manageable effort.

3.4.2. Experimental system light budget

In order to verify dominating system limitations we performed further system characterization experiments. We stress that all power density measurements in this chapter were done with our calibrated Si-photodiode and we referenced all values to the active area of 10 mm by 10 mm for a good comparison. We investigated the noise equivalent power (NEP) of the OPD and evaluated the available fluorescence emission power of a 6-FAM-ssDNA spot to estimate the light budget on the detector side. Here we obtained a NEP of 6.4 nW/cm^2 for our OPD with the 520 nm collimated laser module. The NEP equals the lowest irradiation on the detector for generating a photocurrent above the noise level. The emission power density of the 6-FAM-ssDNA spots were subsequently investigated on the fluorescence microscope. Here we focused the fluorescence

Biomedical Optics EXPRESS

Table 2. Light Budget: Summary of Loss Factors and Improvement Options

Factor	Loss Value	Recommendation
Initial OLED emission power	-	Tuning of organic stacks [25]
Small solid angle of OLED on 6-FAM-ssDNA spot	~97.3%	Use of directional OLEDs, integration of optical elements
6-FAM quantum yield	~5%	-
Stokes shift energy transfer	~4.8%	-
6-FAM-ssDNA spot light transmission	~97%	Place spot in cavity
Spherical fluorescence emission	~98.2%	Reduce the distance between the OPD and the fluorescence spot to collect ~50% of light, integration of optical elements

emission output of one single spot on the Si-Photodiode and calculated an emission power density of approx. 800 nW/cm^2. Thus, the available fluorescence signal under illumination on the microscope lamp is 125 times higher, than the lowest required power density on the OPD to generate a signal above the noise level. Consequently, the detection side of the OLED-OPD unit is evidently not in principle a limitation factor.

As the next step we investigated the efficiency of the 6-FAM-ssDNA excitation with our fabricated FIrPic-OLED. First, we evaluated the excitation intensity under the fluorescence microscope. For our ssDNA assay evaluation experiments (Chapter 3.1) we used the maximum available intensity of the excitation light, which is expected to be much higher than the OLED emission power. Here we placed our Si-Photodiode directly on the stage of our microscope and obtained approx. 15.5 mW/cm^2 as the emission power density. Subsequently we placed again our 6-FAM-ssDNA spot on the stage of the microscope, decreased stepwise the intensity of the excitation light, until the emission spectrum of 6-FAM around 520 nm reached the intensity level of the background signal of the CCD detector. We measured this power density as 60 µW/cm^2 and defined this value as the minimum required emission power density for a successful excitation of the 6-FAM-ssDNA spot. Next, we calculated the emission power density from the OLED normalized to the active area of the Si-PD. For a bias voltage of 9 V the OLED emits 8 µW/cm^2. This power density is 7.5 times lower than the minimum required emission power density for a sufficient excitation of 6-FAM-ssDNA spots and approx. 2000 times lower than the power density of the excitation light used on the fluorescence microscope. Thus, the excitation intensity is currently one of the highest limitation factors for fluorescence sensing of surface bound 6-FAM-ssDNA spots on glass with an OLED-OPD chip.

3.4.3. Discussion

The evaluation above shows that the light budget of the current system is not sufficient to detect with the OPD the fluorescence emission from surface bound 6-FAM-labeled-ssDNA excited by the OLED. To overcome the aforementioned limitations and realize multiplex POC testing further improvements of the system are necessary. Tuning the OLED stacks is a promising next step towards a stable blue emitting FIrPic-OLED with higher damage threshold voltage and thus higher emission power. Liu et al. increased the OLED current efficiency by a factor of ~ 6.5 using a MoO_3 modified ITO as the anode and even by ~ 13.6 by adopting a bilayer device with FIrPic:CBP and FIrPic:TPBi as the double emission layers [25]. We believe, that increasing the efficiency of the OLED will lead to a sufficient excitation for the dye-labeled-ssDNA spots. Additionally, the excitation may also be increased by minimizing the distance between the OLED and the OPD. As an example, reducing the distance from 0.9 mm to 0.1 mm would increase the OLED excitation irradiance on the fluorescence spot by a factor of ~ 1.3 from $\eta_{Det} = 1.8\%$ ($E_{SPOT} = 95$ µW/cm^2) to $\eta_{Det} = 3.95\%$ ($E_{SPOT} = 126$ µW/cm^2). To further improved excitation

Biomedical Optics EXPRESS

performance the integration of planar optical waveguides should be evaluated to get more light on the fluorescence spot. For example, planar waveguides or air mirrors can be directly integrated on microfluidic structures as light guiding elements [26,27]. Furthermore, the geometry of the system should be changed such that the OPD is placed with minimum distance to the fluorescence spots. For this purpose, the optical system could be processed on thin foils. Considering a substrate thickness of 200 µm instead of the current 1-mm glass substrate the simulated efficiency of fluorescence detection could be improved from $\eta_{Det} = 1.8\%$ to $\eta_{Det'} = 22.8\%$. However, this step deserves a careful consideration, since reducing the substrate thickness will lead to a decrease of OLED irradiation on the fluorescence spot. An optimum ratio between the substrate thickness and the OLED-OPD distance has to be evaluated. In summary, the simulations and experiments show that an OLED-OPD detection of surface bound fluorescence markers is within reach with current technology and will profit from the further development of organic optoelectronic devices on thin foils.

4. Conclusions

We investigated a sensing system for decentralized detection of veterinary biomarkers based on an optical detection unit with side-by-side OLED and OPD. This configuration has the advantage of simple assembly and contacting. We developed a specific EHV ssDNA assay based on the hybridization of the fluorescence-labeled ssDNA strand and quencher-labeled reverse complementary ssDNA segments, where the fluorescence of the fluorophore is suppressed upon a certain proximity to the quencher. After the hybridization of the ssDNA segments to dsDNA the fluorophores undergo FRET. We successfully performed the proof-of-concept of hybridization sensing of two complementary dye-labeled ssDNA strands diluted in TE buffer measured on a 12.5 mm by 12.5 mm chip with 8 integrated OLED-OPD pairs. For multiplex POC testing several specific biomarkers of interest can act as capture ssDNA, labeled with different fluorescence molecules. This results in a specific wavelength for a certain biomarker (EHV-1-5 or other viral pathogens), which can be excited and detected with a suitable OLED-OPD pair. An easier approach to multiplex measurements requiring only one type of OLED and one type of OPD is the localized surface binding of a specific biomarker to a specific OLED-OPD detection pair. For this purpose we covalently coupled a fluorescence-labeled ssDNA on a glass surface, which is intended to act as sample capture molecule. We could not detect fluorescence of surface-bound biomarkers with the OLED-OPD chip. We performed a detailed investigation of the limiting factors in the current system. We demonstrated that detection is within reach for improved OLED brightness. Also the system efficiency may be improved employing thinner substrates. This requires at the same time the consideration of directional OLEDs and optical waveguides to achieve efficient fluorescence excitation with the OLED.

The integration of organic optoelectronic devices is a powerful approach pushing further the device sizes towards a highly compact and low-power POC system for biomedical applications. The thermal evaporation technique enables a wide variety of geometrical shapes, sizes and the fabrication on rigid or flexibles substrates. Taking the step towards an in-plane integrated OLED-OPD sensing platform enables the potential for parallel mass fabrication, increasing the commercial viability. Particularly, the fabrication on flexible substrates is highly promising for roll-to-roll fabrication [28]. This monolithic integrated OLED-OPD sensing unit is now ready for biomedical detection of single-type dye-labeled ssDNA in solution.

Funding. European Regional Development Fund (LPW-E/1.2.2/1303, OPTOCHIP); DFG Open Access-Publikationskosten.

Disclosures. NR: altona Diagnostics GmbH (E)

Data availability. Data underlying the results presented in this paper are not publicly available at this time but may be obtained from the authors upon reasonable request.

References

Biomedical Optics EXPRESS

1. C. J. Thieulent, E. S. Hue, C. I. Fortier, P. Dallemagne, S. Zientara, H. Munier-Lehmann, A. Hans, G. D. Fortier, P. H. Pitel, P. O. Vidalain, and S. L. Pronost, "Screening and evaluation of antiviral compounds against Equid alpha-herpesviruses using an impedance-based cellular assay," Virology **526**, 105–116 (2019).
2. G. Perkins, S. Babasyan, A. E. Stout, H. Freer, A. Rollins, C. L. Wimer, and B. Wagner, "Intranasal IgG4/7 antibody responses protect horses against equid herpesvirus-1 (EHV-1) infection including nasal virus shedding and cell-associated viremia," Virology **531**, 219–232 (2019).
3. S. B. Hussey, R. Clark, K. F. Lunn, C. Breathnach, G. Soboll, J. M. Whalley, and D. P. Lunn, "Detection and quantification of equine herpesvirus-1 viremia and nasal shedding by real-time polymerase chain reaction," J. Vet. Diagnostic Investig. **18**(4), 335–342 (2006).
4. P. Daly and S. Doyle, "The development of a competitive PCR-ELISA for the detection of equine herpesvirus-1," J. Virol. Methods **107**(2), 237–244 (2003).
5. H. Lee, E. Kim, Y. Lee, H. Kim, J. Lee, M. Kim, H. J. Yoo, and S. Yoo, "Toward all-day wearable health monitoring: An ultralow-power, reflective organic pulse oximetry sensing patch," Sci. Adv. **4**(11), 1–9 (2018).
6. Y. Khan, D. Han, A. Pierre, J. Ting, X. Wang, C. M. Lochner, G. Bovo, N. Yaacobi-Gross, C. Newsome, R. Wilson, and A. C. Arias, "A flexible organic reflectance oximeter array," Proc. Natl. Acad. Sci. U. S. A. **115**(47), E11015 (2018).
7. E. L. Ratcliff, P. A. Veneman, A. Simmonds, B. Zacher, D. Huebner, S. S. Saavedra, and N. R. Armstrong, "A planar, chip-based, dual-beam refractometer using an integrated organic light-emitting diode (OLED) light source and organic photovoltaic (OPV) detectors," Anal. Chem. **82**(7), 2734–2742 (2010).
8. C. M. Lochner, Y. Khan, A. Pierre, and A. C. Arias, "All-organic optoelectronic sensor for pulse oximetry," Nat. Commun. **5**(1), 5745 (2014).
9. E. Manna, T. Xiao, J. Shinar, and R. Shinar, "Organic photodetectors in analytical applications," Electron. **4**(3), 688–722 (2015).
10. C. Murawski and M. C. Gather, "Emerging biomedical applications of organic light-emitting diodes," Adv. Opt. Mater. **9**(14), 2100269 (2021).
11. T. Mayr, T. Abel, E. Kraker, S. Köstler, A. Haase, C. Konrad, M. Tscherner, and B. Lamprecht, "An optical sensor array on a flexible substrate with integrated organic opto-electric devices," Procedia Engineering **5**, 1005 (2010).
12. A. Pais, A. Banerjee, D. Klotzkin, and I. Papautsky, "High-sensitivity, disposable lab-on-a-chip with thin-film organic electronics for fluorescence detection," Lab Chip **8**(5), 794–800 (2008).
13. R. Liu, T. Xiao, W. Cui, J. Shinar, and R. Shinar, "Multiple approaches for enhancing all-organic electronics photoluminescent sensors: simultaneous oxygen and pH monitoring," Anal. Chim. Acta **778**, 70–78 (2013).
14. C. Lian, K. Yoshida, C. Nogues, and I. D. W. Samuel, "Organic light-emitting diode based fluorescence sensing system for DNA detection," Adv. Mater. Technol. **7**(5), 2100806 (2022).
15. I. Titov, M. Köpke, N. Schneidewind, J. Buhl, Y. Murat, and M. Gerken, "OLED OPD matrix for sensing on a single flexible substrate," IEEE Sens. J. **20**(14), 7540–7547 (2020).
16. I. Titov, M. Köpke, and M. Gerken, "Monolithic integrated OLED–OPD unit for point-of-need nitrite sensing," Sensors **22**(3), 910 (2022).
17. R. Abbel, I. De Vries, A. Langen, G. Kirchner, H. T'Mannetje, H. Gorter, J. Wilson, and P. Groen, "Toward high volume solution based roll-to-roll processing of OLEDs," J. Mater. Res. **32**(12), 2219–2229 (2017).
18. N. Sun, C. Jiang, Q. Li, D. Tan, S. Bi, and J. Song, "Performance of OLED under mechanical strain: a review," J. Mater. Sci.: Mater. Electron. **31**(23), 20688–20729 (2020).
19. L. Le Reste, J. Hohlbein, K. Gryte, and A. N. Kapanidis, "Characterization of dark quencher chromophores as nonfluorescent acceptors for single-molecule FRET," Biophys. J. **102**(11), 2658–2668 (2012).
20. C. Wang, C. Y. Lim, E. Choi, Y. Park, and J. Park, "Highly sensitive user friendly thrombin detection using emission light guidance from quantum dots-aptamer beacons in 3-dimensional photonic crystal," Sens. Actuators, B **223**, 372–378 (2016).
21. M. Gilar, K. J. Fountain, Y. Budman, U. D. Neue, K. R. Yardley, P. D. Rainville, R. J. Russell, and J. C. Gebler, "Ion-pair reversed-phase high-performance liquid chromatography analysis of oligonucleotides: Retention prediction," J. Chromatogr. A **958**(1-2), 167–182 (2002).
22. G. T. Hermanson, Bioconjugate Techniques Chapter 18 - PEGylation and Synthetic Polymer Modification (2013).
23. T. J. Lambert, "FPbase: a community-editable fluorescent protein database," Nat. Methods **16**(4), 277–278 (2019).
24. J.R. Lakowicz, *Principles of Fluorescence Spectroscopy*, 2nd Ed., (Kluwer Academic/Plenum Publishers, 1999).
25. Z. Liu, M. G. Helander, Z. Wang, and Z. Lu, "Band alignment at anode/organic interfaces for highly efficient simplified blue-emitting organic light-emitting diodes," J. Phys. Chem. C **114**(39), 16746–16749 (2010).
26. S. Balslev, A. M. Jorgensen, B. Bilenberg, K. B. Mogensen, D. Snakenborg, O. Geschke, J. P. Kutter, and A. Kristensen, "Lab-on-a-chip with integrated optical transducers," Lab Chip **6**(2), 213–217 (2006).
27. A. Llobera, S. Demming, R. Wilke, and S. Büttgenbach, "Multiple internal reflection poly(dimethylsiloxane) systems for optical sensing," Lab Chip **7**(11), 1560–1566 (2007).
28. Y. Murat, K. Petersons, D. Lanka, L. Lindvold, L. Yde, J. Stensborg, and M. Gerken, "All solution-processed ITO free flexible organic light-emitting diodes," Mater. Adv. **1**(8), 2755–2762 (2020).

4.3 Monolithic Integrated OLED-OPD Unit for Point-of-Need Nitrite Sensing

4.3.1 Introduction

I. Titov, M. Köpke, and M. Gerken, "Monolithic Integrated OLED-OPD Unit for Point-of-Need Nitrite Sensing," Sensors, vol. 22, no. 3, p. 910, Jan. 2022, doi: 10.3390/s22030910.

about the own contribution:

Conceptualization	Planning	Implementation	Manuscript preparation
High	High	High	High

- Definition of the organic materials composition suitable for the detection of nitrite dependent azo dye formations
- Design and modeling of the miniaturized OLED-OPD system for optical measurements
- Planning and implementation of the electrical and spectral characterization of the fabricated OLED-OPD system and the utilized colorimetric Griess assay on various setups
- Planning and construction of the nitrite measurement detection setup and the implementation and evaluation of the experiments
- Estimation of the current system efficiency by using an UV-Vis spectrometer as a reference and comparing the results with literature
- Manuscript preparation and revision

4.3.2 Abstract

In this work, the first photometric nitrite sensor based on the fully organic optoelectronic chip was developed. The realized TCTA:Ir(mppy)$_3$ OLEDs and DMQA:DCV3T OPDs were fabricated in the similar geometrical design as in the first publication. Each substrate contained 4 test chips, which were separated afterwards to 12.5 mm × 12.5 mm sensing units by a wafer saw. Each test chip had 8 OLED-OPD detection units and the organic composition of the OLED-OPD matrix was designed to have suitable peak positions for high absorbance measurements of the azo dye (absorption around 540 nm), formed by the popular Griess reaction. This colorimetric reaction is highly sensitive to the initial nitrite concentration in the sample and shows high linearity up to 1.2 mg L^{-1}. The paper successfully demonstrates measurements of premixed nitrite standard solutions of different concentrations. The calibration plot obtained from these measurements offers a linearity of 99% and an LOD of 46 µg L^{-1} (1 µmol L^{-1}). The proposed nitrite sensing unit is ready for toxic threshold testing of drinking water or aquaculture systems and serves as a first step towards a highly compact, low cost and highly commercially viable PON analytic platform for environmental and agricultural applications [10, 66].

4.3.3 Published Paper

sensors

MDPI

Article

Monolithic Integrated OLED–OPD Unit for Point-of-Need Nitrite Sensing

Igor Titov *, Markus Köpke and Martina Gerken

Integrated Systems and Photonics, Faculty of Engineering, Kiel University, 24118 Kiel, Germany; mko@tf.uni-kiel.de (M.K.); mge@tf.uni-kiel.de (M.G.)
* Correspondence: igti@tf.uni-kiel.de

Abstract: In this study, we present a highly integrated design of organic optoelectronic devices for Point-of-Need (PON) nitrite (NO_2^-) measurement. The spectrophotometric investigation of nitrite concentration was performed utilizing the popular Griess reagent and a reflection-based photometric unit with an organic light emitting diode (OLED) and an organic photodetector (OPD). In this approach a nitrite concentration dependent amount of azo dye is formed, which absorbs light around ~540 nm. The organic devices are designed for sensitive detection of absorption changes caused by the presence of this azo dye without the need of a spectrometer. Using a green emitting TCTA:$Ir(mppy)_3$ OLED (peaking at ~512 nm) and a DMQA:DCV3T OPD with a maximum sensitivity around 530 nm, we successfully demonstrated the operation of the OLED–OPD pair for nitrite sensing with a low limit of detection 46 µg/L (1.0 µM) and a linearity of 99%. The hybrid integration of an OLED and an OPD with 0.5 mm × 0.5 mm device sizes and a gap of 0.9 mm is a first step towards a highly compact, low cost and highly commercially viable PON analytic platform. To our knowledge, this is the first demonstration of a fully organic-semiconductor-based monolithic integrated platform for real-time PON photometric nitrite analysis.

Keywords: sensor systems; photonic devices; nitrite measurement; Griess reagent; OLED; OPD; monolithic integration

Citation: Titov, I.; Köpke, M.; Gerken, M. Monolithic Integrated OLED–OPD Unit for Point-of-Need Nitrite Sensing. *Sensors* **2022**, *22*, 910. https://doi.org/10.3390/s22030910

Academic Editors: Barry K. Lavine and Karl Booksh

Received: 20 December 2021
Accepted: 21 January 2022
Published: 25 January 2022

1. Introduction

Nitrates and nitrites play an essential role for plant growth in agriculture. Thus, they are a major component of inorganic fertilizers [1]. Their high solubility in water results in a particularly critical exceedance of limits in the ground water [2]. The accumulation of agricultural chemicals in the groundwater is a well-known problem. In 1989, Hallberg reported about 39 pesticides in the groundwater of 34 states or provinces of the United States with nitrate as one of the common agricultural chemicals [3]. The exceedance of nitrates and nitrites limits in environmental and physiological systems have adverse effects on animal and human health. The World Health Organization (WHO) set a guideline value of 3 mg/L nitrite in water. Recent studies reported carcinogenic effects, methemoglobinemia, and detrimental effects on the thyroid gland and other organs, associated with the ingestion of high concentrations of nitrate and nitrite due to the high toxicity. Infants are particularly susceptible to methemoglobin formation due to reduction in nitrite. In contrast to hemoglobin, methemoglobin is unable to transport oxygen to the tissues. This condition causes cyanosis or asphyxia. Thus, the detection of nitrite in samples such as water, urine, saliva or blood plasma is crucial and has been reported by many different research groups [4].

Current methods for nitrite ion detection include electrochemical methods (including voltametric, potentiometric and impedimetric electrodes), spectrophotometry, spectrofluorimetry and ion chromatography [5–9]. Electrochemical sensors are popular due to the potential low cost, portability and simple fabrication. Despite the wide application areas

there are still some limitations. Current research on electrochemical sensors focusses on improving the limit of detection and reducing the cross-sensitivity of the electrodes [10]. Here, we focus on spectrophotometry as the most common method for nitrite detection due to its easy procedure, low detection limits, high selectivity and low cost. In particular, the assay based on the Griess reagent for colorimetric nitrite sensing is very popular due to its high stability, selectivity and sensitivity [11]. Early work has been conducted by Petsul et al. using the Griess reaction and an external light emitting diode (LED) with a spectrometer for the absorbance measurements, achieving a limit of detection (LOD) of 0.2 mM [12]. Since then, a variety of different sensor systems with different optical device configurations have been reported. Colorimetric nitrite sensors mostly use LEDs as the light source. Devices such as CCD cameras, spectrometers, smartphone cameras, photomultiplier tubes (PMT) and photodiodes (PD) were recently successfully integrated on the detector side [13–22]. While very impressive results are achieved with the compact integration of the inorganic optoelectronic devices and microfluidic-based approaches, these systems are still rather bulky. For low-cost portable Point-of-Need (PON) solutions, further miniaturization and a simple fabrication method are needed.

To overcome the aforementioned limitations, the integration of organic light emitting diodes (OLEDs) and organic photodetectors (OPDs) promises compact and low-cost optical detection units as hybrid integrated sensors. Recently, very impressive results have been achieved with fabrication of OLEDs and OPDs on flexible and rigid substrates. The devices have been proposed as wearable sensors for health monitoring and Point-of-Need analysis applications [23–29]. Due to the thermal evaporation-based device fabrication technique, all sensing elements are permanently aligned, allowing a high degree of miniaturization. These units can be easily laminated to a microfluidic system for sensing applications in a liquid [30–34].

Based on our experience in biomedical lab-on-chip systems for multiplexed detection [35,36] and monolithic integrated organic optoelectronic devices [37,38], we aim at developing a highly integrated nitrite sensor for Point-of-Need analysis. In this work we present, to the best of our knowledge, the first demonstration of a fully organic optoelectronic system for photometric nitrite sensing based on the Griess reagent with a reflection-type architecture. The OLED and the OPD are successfully monolithically integrated and have a device size of 0.5 mm × 0.5 mm each. The gap between the devices is 0.9 mm. Due to the monolithic integration and a simple fabrication process, the scalability of parallel fabricated sensor units is promising, leading to low cost and potentially disposable PON systems. As a consequence, the commercial viability can be significantly increased.

In the Experimental Section 2, we present in Section 2.1 the OLED–OPD device design and the fabrication procedure of the organic stacks. The experimental characterization of the OPD and OLED devices is given in Section 2.3. Section 2.4 presents the design of the nitrite sensing platform followed by the nitrite sensing experiments in Section 2.5. Conclusions are given in Section 3.

2. Experimental Section

2.1. OLED–OPD Matrix Fabrication

Figure 1a–c show the organic stacks, a geometrical schematic and a photograph of the test chip with 8 OLED–OPD detection units. The realized TCTA:Ir(mppy)$_3$ OLEDs and DMQA:DCV3T OPDs were fabricated on a 25 mm × 25 mm glass substrate with a thickness of 1 mm. Each substrate contained 4 test chips, which were separated afterwards to 12.5 mm × 12.5 mm sensing units by a wafer saw. Here, each test chip had 8 OLED–OPD detection units. The green emitting OLED (peaking at ~512 nm) pixels fabrication was carried out on indium-doped tin oxide (ITO) covered glass by thermally evaporating organic materials. The ITO layer was structured via ultraviolet (UV) photolithography and wet etching to form the 130 nm thin anodes. The organic layers, in sequence, were the hole transport layer of 5 nm molybdenum trioxide (MoO_3) and 35 nm 1,1-bis[(di-4-tolylamino)phenyl]cyclohexane (TAPC), then for the emission layer 20 nm of tris(4-

carbazoyl-9-ylphenyl)amine (TCTA) doped with 8% Tris[2-(p-tolyl)pyridine]iridium(III) ($Ir(mppy)_3$) to generate a highly efficient green-emitting OLED. As the electron transport layer (ETL) and hole blocking layer (HBL) a film of 50 nm 2,2′,2″-(1,3,5-Benzinetriyl)-tris(1-phenyl-1-H-benzimidazole) (TPBi) was deposited followed by the cathode pads consisting of 1 nm lithium fluoride (LiF) and 175 nm aluminum (Al). Consequently, the OLED pixels were defined by the overlapping regions of mutually perpendicular ITO and Al pads.

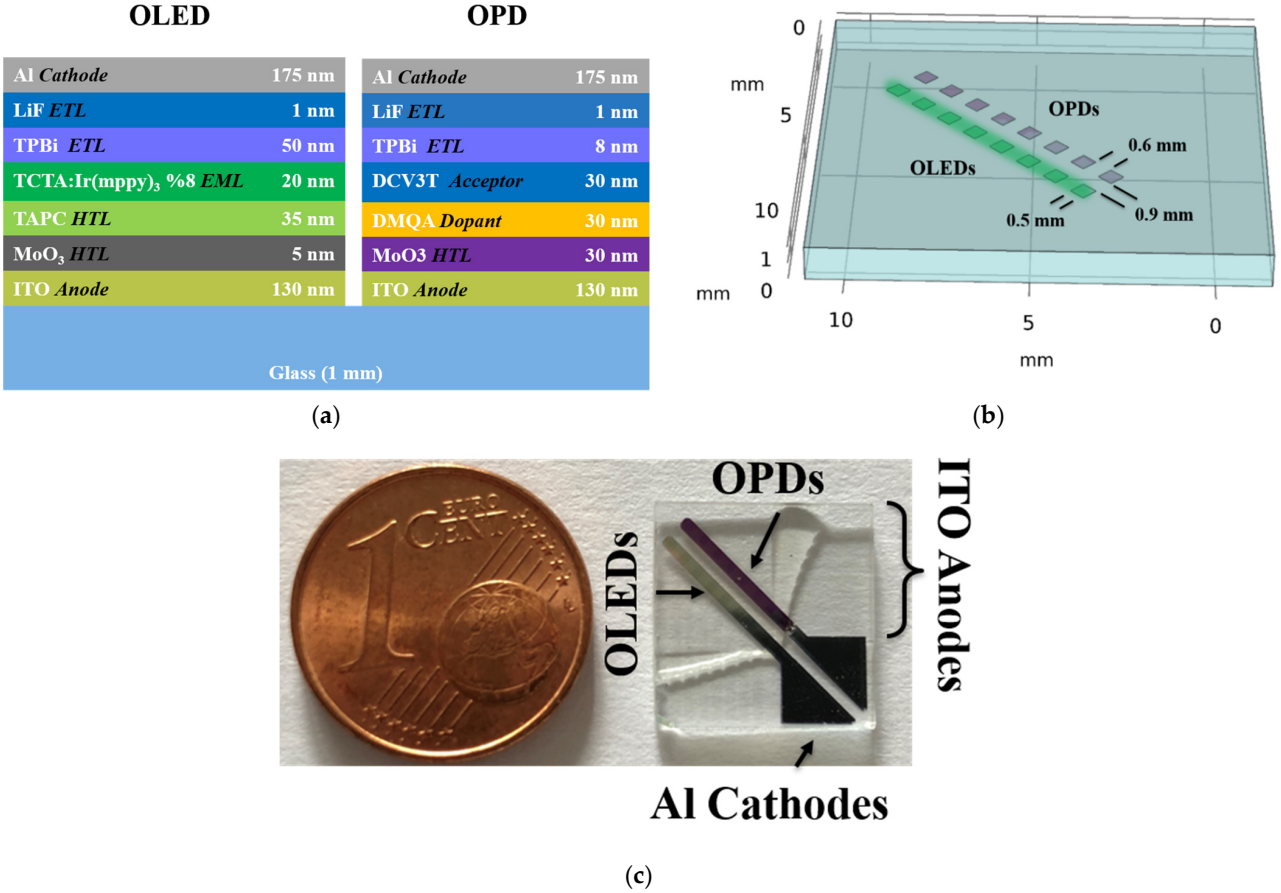

Figure 1. (**a**) Schematic diagram of the OLED and OPD stacks on a single glass substrate; (**b**) geometrical model of the OLED–OPD unit layout with 8 units on one test chip; (**c**) photograph of a fabricated test chip.

The OPD structure starts with a 30 nm molybdenum trioxide (MoO3) layer deposited on the indium-tin-oxide (ITO) coated glass. The organic bilayer structure is composed of 30 nm N,N-Dimethyl quinacridone (DMQA) as the common donor and 30 nm 3′,4′-Dibutyl-5,5″-bis(dicyanovinyl)-2,2′:5′,2″-terthiophene (DCV3T) as the acceptor layer. Next, 8 nm 2,2′,2″-(1,3,5-Benzinetriyl)-tris(1-phenyl-1-H-benzimidazole) (TPBi) was evaporated followed by 1 nm lithium fluoride (LiF) and 175 nm aluminum (Al) to form the cathode pads. The fabricated devices were encapsulated in a nitrogen-filled glovebox to prevent degradation of the organic layers upon measurements outside the glovebox.

2.2. Chemicals and Materials

Following materials were used as the organic components of the devices: 1,1-bis[(di-4-tolylamino)phenyl]cyclohexane (TAPC, CAS-No: 58473-78-2, Merck KGaA, Darmstadt, Germany), tris(4-carbazoyl-9-ylphenyl)amine (TCTA, CAS-No: 139092-78-7, Merck KGaA, Darmstadt, Germany), 2,2′,2″-(1,3,5-Benzinetriyl)-tris(1-phenyl-1-H-benzimidazole) (TPBi, CAS-No: 192198-85-9, Luminescence Technology Corp., New Taipei City, Taiwan), Tris[2-

(p-tolyl)pyridine]iridium(III) ($Ir(mppy)_3$, CAS-No: 149005-33-4, Luminescence Technology Corp., New Taipei City, Taiwan), N,N-Dimethyl quinacridone (DMQA, CAS-No: 19205-19-7, Lumtec), 3′,4′-Dibutyl-5,5″-bis(dicyanovinyl)-2,2′:5′,2″-terthiophene (DCV3T, CAS-No: 908588-68-1, Luminescence Technology Corp., New Taipei City, Taiwan), molybdenum trioxide (MoO_3, CAS-No: 1313-27-5, Merck KGaA, Darmstadt, Germany), lithium fluoride (LiF, CAS-No: 7789-24-4, Merck KGaA, Darmstadt, Germany), aluminum (Al, CAS-No: 7429-90-5, Merck KGaA, Darmstadt, Germany).

Nitrite standard solutions were diluted from 200 mg/L sodium nitrite ($NaNO_2$) prior to use. The stock solution was prepared by dissolving 0.3 g sodium nitrite (CAS-No: 908588-68-1, Merck KGaA, Darmstadt, Germany) in deionized water. A nitrite essay kit (MAK376, Merck KGaA, Darmstadt, Germany) was used to prepare the Griess reagent.

2.3. Device Characterization

The characteristics of one OPD are shown in Figure 2a,b. The absorption spectrum of the organic donor–acceptor bilayer composite was determined using a UV-Vis spectrometer (Lambda 800, PerkinElmer, Waltham, MA, USA), showing the highest sensitivity between 500 and 550 nm. The current–voltage characteristics were performed by a source measure unit (SourceMeter 2450, Keithley Instruments, Cleveland, OH, USA) and a 520 nm collimated laser module (CPS520, 4.5 mW, Thorlabs GmbH, Lübeck, Germany). The OPD shows typical diode characteristics and a good sensitivity. The measured photocurrent was 15.4 nA under dark conditions and 0.7 mA for an incident light power of ~0.8 mW/cm^2 at the wavelength of 520 nm at 0 V.

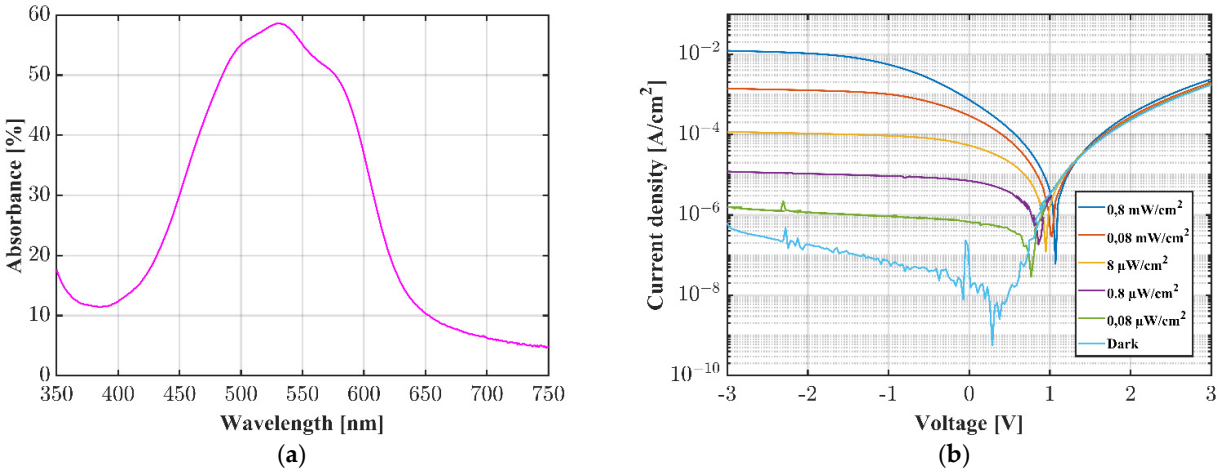

(**a**) (**b**)

Figure 2. Optical and electrical characterization of the DMQA.DCV3T OPD. (**a**) UV-Vis measurement of 60 nm DMQA:DCV3T absorptive bilayer; (**b**) current density–voltage characteristics in the dark and under illumination with a subsequently filtered 520 nm laser.

The OLED emission spectrum was measured with a spectrometer (iHR320, Horiba, Kyoto, Japan) by using an optical fiber placed right above the OLED pixel. For optical and electrical characterization, we used a commercial calibrated Si-photodiode (FDS1010, Thorlabs GmbH, Lübeck, Germany) and two source measure units (SourceMeter 2450 and 2400, Keithley Instruments, Cleveland, OH, USA). The bottom-emitting OLED was placed on top of the large-area photodiode to collect the outcoupled light. The current density and the luminance were calculated with the recorded OLED current and the Si-photodiode photocurrent induced by the OLED. Figure 3a shows the spectrum of the green-emitting OLED. The peak wavelength is located at ~512 nm. The inset shows a photograph of an OLED pixel operated at 9 V. Figure 3b shows the electrical and optical characterization of the $Ir(mppy)_3$ OLED. The onset voltage is approximately 3.3 V. The measurement was performed 4 times in sequence and showed good repeatability.

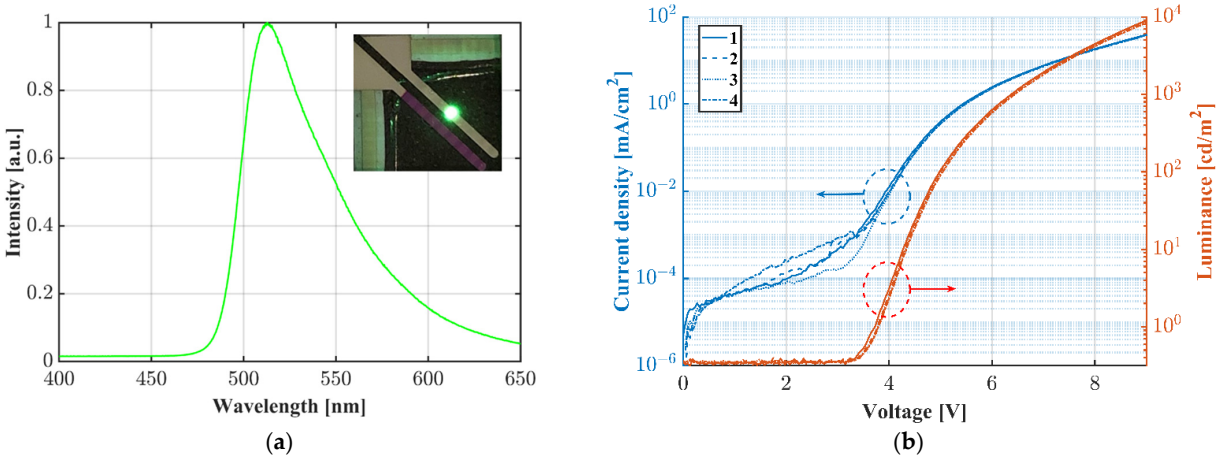

Figure 3. (**a**) Normalized spectrum of the green emitting (peaking at ~512 nm) $Ir(mppy)_3$ OLED as an example; (**b**) current density and luminance vs. voltage characteristics of the fabricated bottom-emitting OLED.

It is stressed that the spectrometer is only used for device characterization and reference measurements. No spectrometer is needed for the final nitrite-measurement system.

2.4. Design of the Test Chamber

For proof-of-principle demonstration of nitrite sensing with the OLED–OPD unit, we realized a test setup for contacting and fluid application. The OLED–OPD units were contacted with a printed circuit board (PCB) and elastomeric ZEBRA® connectors. The proof of concept was performed with a custom rubber seal covered with a cap to ensure tightness and avoid leakage of the chemicals. The setup was used with a drilled cap (Figure 4III) and the liquids were filled into the chamber with a pipette. The measurements were performed with two source measure units for OLED supplying and recording the photocurrent of the OPD in a darkened environment.

2.5. Nitrite Sensing with OLED–OPD Matrix

The photometric nitrite sensing was performed with a reagent based on the Griess reaction. Figure 5a shows the chemical transformation of N-(1-naphthyl)ethylenediamine dihydrochloride (NED) and sulfanilamide in an acidic solution. Sulfanilamide reacts with the nitrite ion and forms a diazonium salt. The azo dye formation occurs due to the reaction with NED. The absorbance around 540 nm strongly depends on the initial nitrite concentration.

As depicted in Figure 5b, we chose the organic composition of the OLED–OPD matrix for the highest absorbance of the green OLED light on the OPD. Due to total internal reflection (TIR) the light propagated partly inside the glass substrate and induced photocurrent in the OPD, since the OLED is an extended device with isotropic emission. The following Figure 6 shows a schematic of the expected azo dye concentration dependent signal change of the OLED–OPD matrix unit. In Figure 6a the light propagated partly inside the glass substrate and was partly reflected back onto the OPD after traveling inside the analyte. For lower sample concentration the partly absorbed light was reflected multiple times at the surfaces inside the liquid chamber and was partly reflected back onto the OPD. For higher concentration (Figure 6b) of nitrite standard sample and, consequently, higher concentration of the azo dye, the absorbance of the light inside the chamber increased. Thus, only a fraction of initial emitted amount of light was reflected back onto the OPD and the photocurrent consequently decreased.

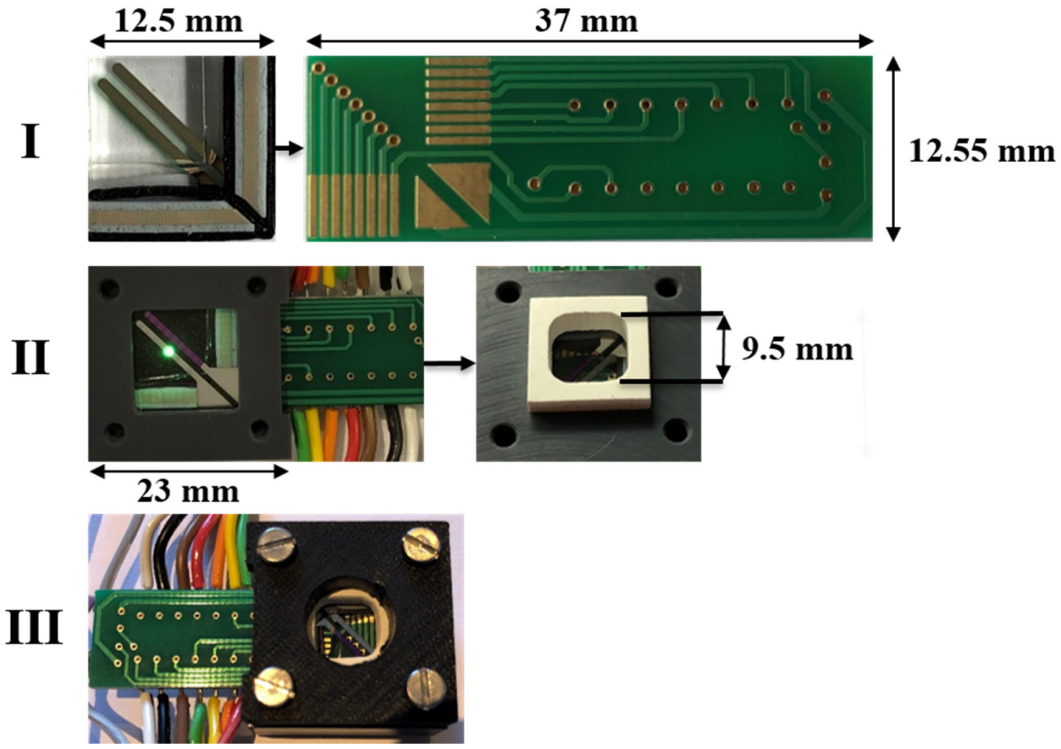

Figure 4. Nitrite measurement detection setup. The system is housing an OLED–OPD matrix, contacted with elastomeric ZEBRA® connectors and a printed circuit board (PCB) with mirrored electrodes design (**Step I**). The organic platform and the PCB are pressed to each other with a milled mount. The fluid chamber is sealed with a rubber seal, pressed on top of the organic OLED–OPD chip (**Step II**). Finally, the setup was used with a drilled cap for adding and removing liquids with a pipette (**Step III**).

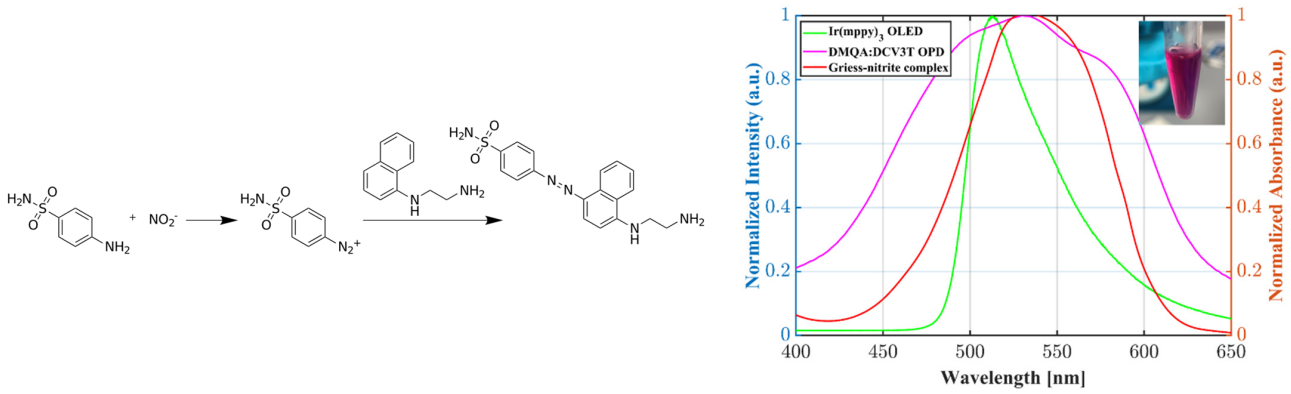

Figure 5. (**a**) Schematic of the Griess reaction for spectrophotometric quantification of the nitrite concentration; (**b**) overview of the OLED emission spectrum as well as the absorption spectra of the OPD and the Griess-reaction-based azo dye. The chosen organic composition of the OLED–OPD system has overlapping emission and absorbance spectra for the highest nitrite sensitivity. The inset shows, as an example, strong absorbance at around 540 nm for a nitrite standard sample of 30 mg/L.

The nitrite sensing experiments were performed with nitrite standard solutions at room temperature prepared 10 min prior to use. Although the azo dye formation was near instantaneous, according to the datasheet the reaction was accomplished after an incubation time of 10 min. The signal was stable for 1 h after adding the reagents. Brizzolari et al.

reported a reaction time of 15 min to achieve the most stable results [39]. Pai and Yang evaluated the azo forming kinetics for different concentration of NED and the final acidity [40]. The evaluated t(90%) values were measured to be in the region of <1 min. The OLED was operated at constant current mode at 60 µA during all measurements. The photocurrent of the OPD was recorded at zero bias.

Figure 7a,b shows the measurement of the premixed Griess reagent and nitrite standard solutions. Prior to the measurements with the OLED–OPD unit we tested the nitrite samples with a UV-Vis spectrometer (Lambda 800, PerkinElmer, Waltham, MA, USA). Figure 7a shows a calibration plot with a linearity of 99% as a reference. Figure 7b shows the measurement with the investigated OLED–OPD sensing unit. We started each measurement with an empty fluid chamber and subsequently added samples of 200 µL ranging from 0.2 to 1.2 mg/L nitrite with a pipette. The Griess complex recorded the signal response in real time. The signal was a superposition of waveguided light, stray light and light passing through the liquid chamber. The detected intensity depended on the absorbance of light by the azo dye. The observed decrease in the photocurrent upon addition of the nitrite solution is shown in the inset of Figure 7b. For example, the photocurrent for the empty chamber was 2.46 nA and after addition of a 1.0 mg/L nitrite solution the photo current changed to 1.10 nA. Thus, the absolute value of the current was reduced by 1.36 nA. The calibration function obtained from these measurements was found to be linear up to 1.2 mg/L, offering linearity of approximately 99%. The sensitivity was calculated as S = 0.6 nA/(mg/L). The standard deviation current noise level was determined as σ = 9.23 pA. This yielded a limit of detection (LOD) of LOD = 3 × σ/S = 46 µg/L (1.0 µM).

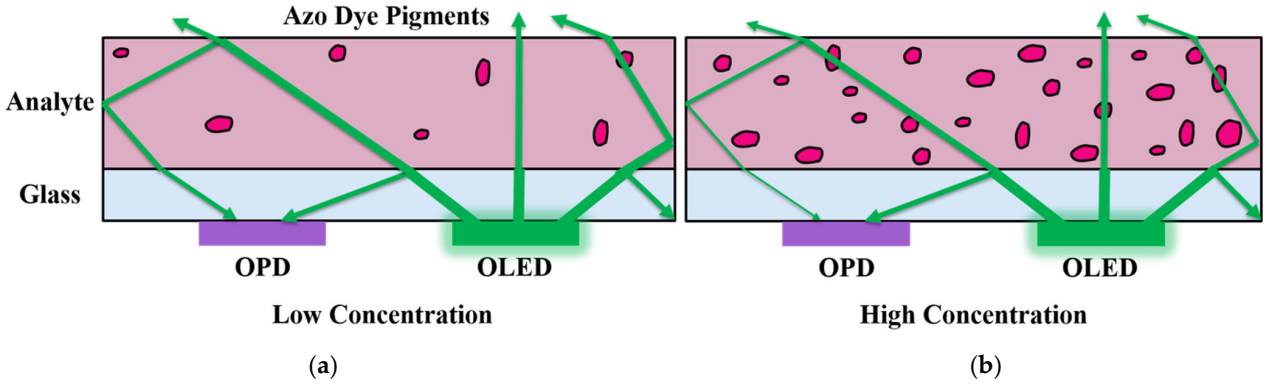

Figure 6. Schematic of the azo dye concentration-dependent absorbance of OLED light inside the analyte. (**a**) The light propagated partly inside the glass substrate and was partly reflected back onto the OPD; (**b**) for higher concentrations of nitrite standard sample and consequently higher concentrations of the azo dye the light showed increased absorption inside the chamber at the azo dye pigments. Thus, only a fraction of initial amount of light was reflected back onto the OPD. The photocurrent decreased as a consequence.

The system shows the highest photocurrent induced by the OLED light in the absence of the analyte in the fluidic chamber. Injecting the azo dye concentrated sample inside the chamber resulted in decreasing photocurrent due to the superposition of the refractive index change and the absorbance of the light at azo dye pigments. Since the critical angle for total internal reflection (TIR) inside the glass substrate increases for liquid analytes on the OLED–OPD matrix surface, the amount of light entering the analyte also increased and resulted in less guided stray light inside the glass substrate. For constant refractive indices of the analytes, the offset of the photocurrent was also constant and was consequently neglected during the measurement. The OPD signal at high absorption is determined with a highly concentrated nitrite sample (200 mg/L) to be 2.17 nA. As a further verification of the absorption inside the analyte, we evaluated the influence on the OPD photocurrent by adding a mirror on top of the OLED–OPD measurement unit. Due to reflection of the light

back to the OPD we observed a small increase in the photocurrent for low concentrations of the nitrite samples, whereas adding a mirror for high nitrite concentrations resulted in no enhancement of the photocurrent. This is due to the high absorption of the high azo dye concentration.

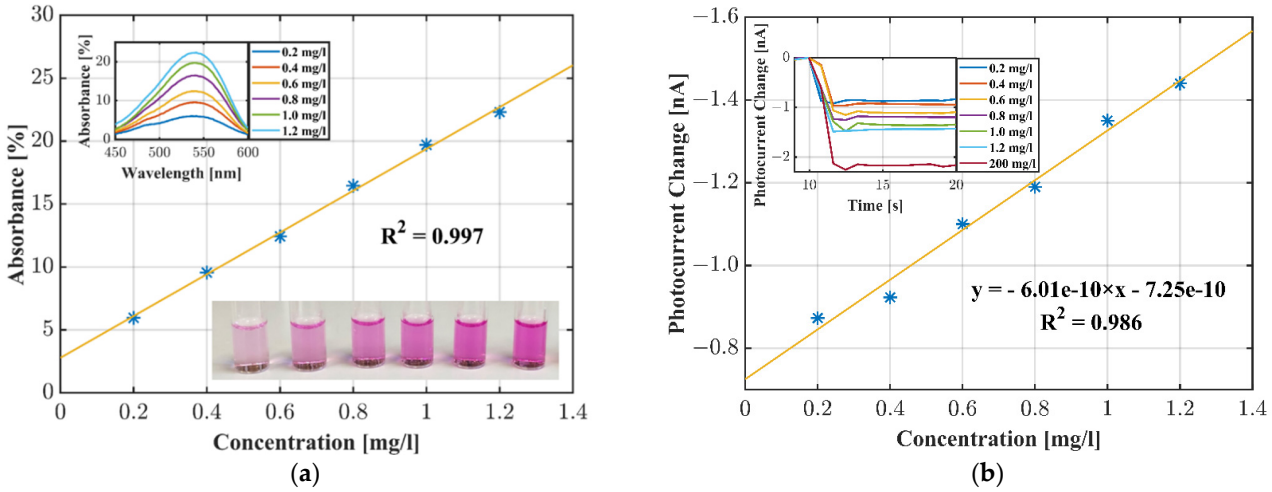

Figure 7. (**a**) UV-Vis reference measurement evaluated at 540 nm; (**b**) nitrite measurement and the calibration plot for the nitrite standard solutions obtained with the OLED–OPD unit and the azo dye absorbance.

Table 1 shows a comparison between our investigated OLED–OPD unit and other recently reported photometric based nitrite sensing platforms. It shows that our proof-of-concept detection system already has a promising limit of detection. Taking the step towards a fully integrated organic-semiconductor chip, our approach has the potential for parallel mass fabrication. Whereas the proof of concept was successfully performed, the analyte consumption was still rather high due to the large fluid chamber. The filling of the chamber requires approximately 100 µL to avoid light scattering due to air–liquid boundaries. Furthermore, operating the current setup in sunlight results in a significant photocurrent offset. This background signal can be subtracted in the post processing of the raw data or simply suppressed by using a non-transparent microfluidic device. Recently, we suggested employing a black absorptive material combined with a PDMS microfluidic for successful suppression of stray light [30]. Consequently, we aim to integrate the OLED–OPD matrix with a microfluidic device as the next step. Since the requirements for PON applications implicate a portable and wireless system, we also aim to upgrade the OLED–OPD sensing platform to a battery-powered system. A reliable hardware setup can be achieved by integrating low-cost, state-of-the-art hardware, i.e., a transimpedance amplifier for an I/V conversion and an analog-to-digital converter (ADC) that translates the photocurrent in a digital dataset representing the magnitude of the induced current. The results can be processed with a microcontroller and transmitted to a monitor. Wang et al. recently reported a comprehensive design of a hardware circuit for an optoelectronic sensor [41].

Further performance improvements of the system can be achieved by tuning the organic stacks of the OLED–OPD unit. Green OLEDs with higher efficiency have been recently proposed [42].

Table 1. Sensing performance comparison of investigated OLED–OPD unit and recently reported photometric nitrite sensors.

Detection Hardware	LOD (μM)	Reference
Spectrometer based laboratory systems		
Fluorescence spectrometer	0.1	Zhang et al. [43]
Fluorescence spectrometer	0.04	Feng et al. [18]
Fluorescence spectrometer	0.05	Ren et al. [19]
UV–Vis spectrometer	0.1	Amanulla et al. [14]
UV–Vis spectrometer	0.12	Wang et al. [16]
Compact and miniaturized systems		
UV lamp–Photomultiplier tube	0.009	Wang and Wang [17]
Smartphone	0.65	Vidal et al. [15]
Raspberry Pi camera	4.34	Luka et al. [44]
Micro spectrometer	0.2	Greenway et al. [45]
LED–CCD camera	<250	Shi et al. [13]
LED–Photodiode	0.014	Sieben et al. [46]
LED–Photodiode	0.015	Beaton et al. [47]
LED–Photodiode	1.7	Khanfar et al. [20]
LED–Photodiode	1.54	Dudala et al. [21]
LED–Photodiode	1.7	Nightingale et al. [48]
LED–LED	0.74	Czugala et al. [23]
LED–PTB7:$PC_{70}BM$ OPD	<0.55	Pires et al. [49]
TCTA:$Ir(mppy)_3$ OLED–DMQA:DCV3T OPD	1.0	This work

3. Conclusions

We developed the first photometric nitrite sensor based on a fully organic optoelectronic chip. The organic composition of the OLED–OPD matrix was designed to have suitable peak positions for high absorbance measurements of the azo dye (Abs. ~540 nm). We demonstrated a measurement of premixed nitrite standard solutions of different concentrations utilizing the Griess reagent. The calibration plot obtained from these measurements was found to be linear up to 1.2 mg/L, offering a linearity of 99%. The limit of detection (LOD) was calculated to be 46 μg/L (1.0 μM). This nitrite sensing unit is now ready for toxic threshold testing of drinking water or aquaculture systems. For quantification of concentrations below the current LOD, further improvements shall be investigated. As the next step, tuning of the organic stacks may serve for improvement of the system performance. The analyte consumption may be reduced by integrating the organic chip with a microfluidic unit. For Point-of-Need applications it is crucial to integrate the device with a portable and battery-powered system.

On the fabrication side, we already demonstrated the monolithic integration of 8 OLED–OPD pairs on a 12.5 mm by 12.5 mm substrate. Thus, this chip holds the potential for highly integrated multiplex sensing as well as the implementation of redundancy. In summary, employing organic optoelectronic devices in optical sensing approaches led to several benefits. The sensors can be manufactured on rigid or flexible substrates. The thermal evaporation technique enables a wide variety of geometrical shapes and device sizes leading to a high degree of design freedom. Particularly, the fabrication on flexible substrates is highly promising for large-scale roll-to-roll fabrication. The OLED–OPD unit holds great promise for use in a variety of applications ranging from bio-photonic sensors for human disease detection to environmental monitoring.

Author Contributions: Conceptualization, I.T. and M.G.; methodology, I.T.; validation, I.T. and M.G.; formal analysis, I.T. and M.G.; investigation, I.T. and M.K.; data curation, I.T.; writing—original draft preparation, I.T. and M.G.; writing—review and editing, I.T. and M.G.; visualization, I.T.; project administration, I.T. and M.G.; resources, M.G.; funding acquisition, M.G. All authors have read and agreed to the published version of the manuscript.

Funding: This project has received funding partly from the European Research Council (ERC) under the European Union's Horizon 2020 research and innovation programme (BEAMOLED, grant agreement No. 899861) and partly from the European Regional Development Fund (EFRE) by the European Union (OPTOCHIP, LPW-E/1.2.2/1303). We also acknowledge financial support by DFG within the funding programme Open Access Publizieren.

Conflicts of Interest: The authors declare no conflict of interest.

References

1. Follett, R.F.; Hatfield, J.L. Nitrogen in the Environment: Sources, Problems, and Management. *Sci. World J.* **2001**, *1*, 920–926. [CrossRef] [PubMed]
2. Speijers, G.J.A. Nitrate and nitrite in drinking-water. *World Health Organ.* **2011**. Available online: https://www.who.int/water_sanitation_health/dwq/chemicals/nitratenitrite2ndadd.pdf (accessed on 30 August 2021).
3. Hallberg, G.R. Pesticides Pollution of Groundwater in the Humid United States. *Agric. Ecosyst. Environ.* **1989**, *26*, 299–367. [CrossRef]
4. Parvizishad, M.; Dalvand, A.; MahviA, H.; Goodarzi, F. A Review of Adverse Effects and Benefits of Nitrate and Nitrite in Drinking Water and Food on Human Health. *Health Scope* 2017, in press. [CrossRef]
5. Adarsh, N.; Shanmugasundaram, M.; Ramaiah, D. Efficient Reaction Based Colorimetric Probe for Sensitive Detection, Quantification, and on-Site Analysis of Nitrite Ions in Natural Water Resources. *Anal. Chem.* **2013**, *85*, 10008–10012. [CrossRef] [PubMed]
6. Liu, Y.L.; Kang, N.; Ke, X.B.; Wang, D.; Ren, L.; Wang, H.J. A Fluorescent Nanoprobe Based on Metal-Enhanced Fluorescence Combined with Förster Resonance Energy Transfer for the Trace Detection of Nitrite Ions. *RSC Adv.* **2016**, *6*, 27395–27403. [CrossRef]
7. Antczak-Chrobot, A.; Bąk, P.; Wojtczak, M. The Use of Ionic Chromatography in Determining the Contamination of Sugar By-Products by Nitrite and Nitrate. *Food Chem.* **2018**, *240*, 648–654. [CrossRef]
8. Tan, J.F.; Anastasi, A.; Chandra, S. Electrochemical Detection of Nitrate, Nitrite and Ammonium for on-Site Water Quality Monitoring. *Curr. Opin. Electrochem.* **2022**, *32*, 100926. [CrossRef]
9. Li, G.; Xia, Y.; Tian, Y.; Wu, Y.; Liu, J.; He, Q.; Chen, D. Review—Recent Developments on Graphene-Based Electrochemical Sensors toward Nitrite. *J. Electrochem. Soc.* **2019**, *166*, B881–B895. [CrossRef]
10. Wang, Q.H.; Yu, L.J.; Liu, Y.; Lin, L.; Lu, R.G.; Zhu, J.P.; He, L.; Lu, Z.L. Methods for the Detection and Determination of Nitrite and Nitrate: A Review. *Talanta* **2017**, *165*, 709–720. [CrossRef]
11. Dutt, J.; Davis, J. Current Strategies in Nitrite Detection and Their Application to Field Analysis. *J. Environ. Monit.* **2002**, *4*, 465–471. [CrossRef] [PubMed]
12. Petsul, P.; Greenway, G.; Haswell, S. The Development of an On-Chip Micro-Flow Injection Analysis of Nitrate with a Cadmium Reductor. *Anal. Chim. Acta* **2001**, *428*, 155–161. [CrossRef]
13. Shi, Y.; Liu, H.L.; Zhu, X.Q.; Zhu, J.M.; Zuo, Y.F.; Yang, Y.; Jiang, F.H.; Sun, C.J.; Zhao, W.H.; Han, X.T. Optofluidic Differential Colorimetry for Rapid Nitrite Determination. *Lab Chip* **2018**, *18*, 2994–3002. [CrossRef] [PubMed]
14. Amanulla, B.; Palanisamy, S.; Chen, S.M.; Chiu, T.W.; Velusamy, V.; Hall, J.M.; Chen, T.-W.; Ramaraj, S.K. Selective Colorimetric Detection of Nitrite in Water Using Chitosan Stabilized Gold Nanoparticles Decorated Reduced Graphene Oxide. *Sci. Rep.* **2017**, *7*, 1–9. [CrossRef] [PubMed]
15. Vidal, E.; Lorenzetti, A.; Lista, A.G.; Domini, C.E. Micropaper-Based Analytical Device (MPAD) for the Simultaneous Determination of Nitrite and Fluoride Using a Smartphone. *Microchem. J.* **2018**, *143*, 467–473. [CrossRef]
16. Wang, H.; Wan, N.; Ma, L.; Wang, Z.; Cui, B.; Han, W.; Chen, Y. A Novel and Simple Spectrophotometric Method for Detection of Nitrite in Water. *Analyst* **2018**, *143*, 4555–4558. [CrossRef]
17. Wang, L.; Wang, Q. Selective Determination of Nitrite/Nitrate Based on Photo-Induced Redox Activity of Titanium Dioxide. *J. Sep. Sci.* **2018**, *41*, 4075–4082. [CrossRef]
18. Feng, Z.; Li, Z.; Zhang, X.; Shi, Y.; Zhou, N. Nitrogen-Doped Carbon Quantum Dots as Fluorescent Probes for Sensitive and Selective Detection of Nitrite. *Molecules* **2017**, *22*, 2061. [CrossRef]
19. Ren, H.H.; Fan, Y.; Wang, B.; Yu, L.P. Polyethylenimine-Capped CdS Quantum Dots for Sensitive and Selective Detection of Nitrite in Vegetables and Water. *J. Agric. Food Chem.* **2018**, *66*, 8851–8858. [CrossRef]
20. Khanfar, M.F.; Abu Eisheh, N.J.; Al-Ghussain, L.; Al-Halhouli, A.T. Lab on a Chip for the Colorimetric Determination of Nitrite in Processed Meat Products in the Jordanian Market. *Micromachines* **2019**, *10*, 36. [CrossRef] [PubMed]
21. Dudala, S.; Dubey, S.K.; Goel, S. Fully Integrated, Automated, and Smartphone Enabled Point-of-Source Portable Platform with Microfluidic Device for Nitrite Detection. *IEEE Trans. Biomed. Circuits Syst.* **2019**, *13*, 1518–1524. [CrossRef] [PubMed]
22. Czugala, M.; Fay, C.; O'Connor, N.E.; Corcoran, B.; Benito-Lopez, F.; Diamond, D. Portable Integrated Microfluidic Analytical Platform for the Monitoring and Detection of Nitrite. *Talanta* **2013**, *116*, 997–1004. [CrossRef] [PubMed]
23. Bansal, A.K.; Hou, S.; Kulyk, O.; Bowman, E.M.; Samuel, I.D.W. Wearable Organic Optoelectronic Sensors for Medicine. *Adv. Mater.* **2015**, *27*, 7638–7644. [CrossRef]

24. Yokota, T.; Zalar, P.; Kaltenbrunner, M.; Jinno, H.; Matsuhisa, N.; Kitanosako, H.; Tachibana, Y.; Yukita, W.; Koizumi, M.; Someya, T. Ultraflexible Organic Photonic Skin. *Sci. Adv.* **2016**, *2*, e1501856. [CrossRef] [PubMed]
25. Lee, H.; Kim, E.; Lee, Y.; Kim, H.; Lee, J.; Kim, M.; Yoo, H.J.; Yoo, S. Toward All-Day Wearable Health Monitoring: An Ultralow-Power, Reflective Organic Pulse Oximetry Sensing Patch. *Sci. Adv.* **2018**, *4*, eaas9530. [CrossRef] [PubMed]
26. Khan, Y.; Han, D.; Pierre, A.; Ting, J.; Wang, X.; Lochner, C.M.; Bovo, G.; Yaacobi-Gross, N.; Newsome, C.; Wilson, R.; et al. A Flexible Organic Reflectance Oximeter Array. *Proc. Natl. Acad. Sci. USA* **2018**, *115*, E11015–E11024. [CrossRef] [PubMed]
27. Ratcliff, E.L.; Veneman, P.A.; Simmonds, A.; Zacher, B.; Huebner, D.; Saavedra, S.S.; Armstrong, N.R. A Planar, Chip-Based, Dual-Beam Refractometer Using an Integrated Organic Light-Emitting Diode (OLED) Light Source and Organic Photovoltaic (OPV) Detectors. *Anal. Chem.* **2010**, *82*, 2734–2742. [CrossRef] [PubMed]
28. Lochner, C.M.; Khan, Y.; Pierre, A.; Arias, A.C. All-Organic Optoelectronic Sensor for Pulse Oximetry. *Nat. Commun.* **2014**, *5*, 5745. [CrossRef]
29. Mayr, T.; Abel, T.; Kraker, E.; Köstler, S.; Haase, A.; Konrad, C.; Tscherner, M.; Lamprecht, B. An Optical Sensor Array on a Flexible Substrate with Integrated Organic Opto-Electric Devices. *Procedia Eng.* **2010**, *5*, 1005–1008. [CrossRef]
30. Titov, I.; Kopke, M.; Schneidewind, N.C.; Buhl, J.; Murat, Y.; Gerken, M. OLED OPD Matrix for Sensing on a Single Flexible Substrate. *IEEE Sens. J.* **2020**, *20*, 7540–7547. [CrossRef]
31. Pais, A.; Banerjee, A.; Klotzkin, D.; Papautsky, I. High-Sensitivity, Disposable Lab-on-a-Chip with Thin-Film Organic Electronics for Fluorescence Detection. *Lab Chip* **2008**, *8*, 794. [CrossRef] [PubMed]
32. Poorahong, S.; Lefevre, F.; Perron, M.C.; Juneau, P.; Izquierdo, R. Integration of Optical and Electrochemical Sensors on a Microfluidic Platform Using Organic Optoelectronic Components and Silver Nanowires. In Proceedings of the Annual International Conference of the IEEE Engineering in Medicine and Biology Society, EMBS, Orlando, FL, USA, 16–20 August 2016; pp. 3002–3005. [CrossRef]
33. Williams, G.; Backhouse, C.; Aziz, H. Integration of Organic Light Emitting Diodes and Organic Photodetectors for Lab-on-a-Chip Bio-Detection Systems. *Electronics* **2014**, *3*, 43–75. [CrossRef]
34. Lefèvre, F.; Chalifour, A.; Yu, L.; Chodavarapu, V.; Juneau, P.; Izquierdo, R. Algal Fluorescence Sensor Integrated into a Microfluidic Chip for Water Pollutant Detection. *Lab Chip* **2012**, *12*, 787–793. [CrossRef] [PubMed]
35. Jahns, S.; Bräu, M.; Meyer, B.-O.; Karrock, T.; Gutekunst, S.B.; Blohm, L.; Selhuber-Unkel, C.; Buhmann, R.; Nazirizadeh, Y.; Gerken, M. Handheld imaging photonic crystal biosensor for multiplexed, label-free protein detection. *Biomed. Opt. Express* **2015**, *6*, 3724. [CrossRef] [PubMed]
36. Jahns, S.; Gutekunst, S.B.; Selhuber-Unkel, C.; Nazirizadeh, Y.; Gerken, M. Human Blood Microfluidic Test Chip for Imaging, Label-Free Biosensor. *Microsyst. Technol.* **2016**, *22*, 1513–1518. [CrossRef]
37. Jahns, S.; Iwers, A.F.; Balke, J.; Gerken, M. Organic Optoelectronics for Lab-on-Chip Fluorescence Detection. *Tech. Mess.* **2017**, *84*, 48–51. [CrossRef]
38. Threm, D.; Gugat, J.L.; Pradana, A.; Radler, M.; Mikat, J.; Gerken, M. Self-Aligned Integration of Spin-Coated Organic Light-Emitting Diodes and Photodetectors on a Single Substrate. *IEEE Photon. Technol. Lett.* **2012**, *24*, 912–914. [CrossRef]
39. Brizzolari, A.; Cas, M.D.; Cialoni, D.; Marroni, A.; Morano, C.; Samaja, M.; Paroni, R.; Rubino, F. High-Throughput Griess Assay of Nitrite and Nitrate in Plasma and Red Blood Cells for Human Physiology Studies under Extreme Conditions. *Molecules* **2021**, *26*, 4569. [CrossRef]
40. Pai, S.C.; Yang, C.C.; Riley, J.P. Formation Kinetics of the Pink Azo Dye in the Determination of Nitrite in Natural Waters. *Anal. Chim. Acta* **1990**, *232*, 345–349. [CrossRef]
41. Wang, C.; Li, Z.; Pan, Z.; Li, D. A High-Performance Optoelectronic Sensor Device for Nitrate Nitrogen in Recirculating Aquaculture Systems. *Sensors* **2018**, *18*, 3382. [CrossRef]
42. Wu, R.; Liu, W.; Zhou, L.; Li, X.; Chen, K.; Zhang, H. Highly Efficient Green Single-Emitting Layer Phosphorescent Organic Light-Emitting Diodes with an Iridium (III) Complex as a Hole-Type Sensitizer. *J. Mater. Chem. C* **2019**, *7*, 2744–2750. [CrossRef]
43. Zhang, F.; Zhu, X.; Jiao, Z.; Liu, X.; Zhang, H. Sensitive Naked Eye Detection and Quantification Assay for Nitrite by a Fluorescence Probe in Various Water Resources. *Acta-Part A Mol. Biomol. Spectrosc.* **2018**, *200*, 275–280. [CrossRef] [PubMed]
44. Luka, G.S.; Nowak, E.; Kawchuk, J.; Hoorfar, M.; Najjaran, H. Portable Device for the Detection of Colorimetric Assays. *R. Soc. Open Sci.* **2017**, *4*, 171025. [CrossRef] [PubMed]
45. Greenway, G.; Haswell, S.; Petsul, P. Characterisation of a Micro-Total Analytical System for the Determination of Nitrite with Spectrophotometric Detection. *Anal. Chim. Acta* **1999**, *387*, 1–10. [CrossRef]
46. Sieben, V.J.; Floquet, C.F.A.; Ogilvie, I.R.G.; Mowlem, M.C.; Morgan, H. Microfluidic Colourimetric Chemical Analysis System: Application to Nitrite Detection. *Anal. Methods* **2010**, *2*, 484. [CrossRef]
47. Beaton, A.; Sieben, V.; Floquet, C.F.; Waugh, E.M.; Bey, S.A.K.; Ogilvie, I.R.; Mowlem, M.C.; Morgan, H. An Automated Microfluidic Colourimetric Sensor Applied in Situ to Determine Nitrite Concentration. *Sens. Actuators B Chem.* **2011**, *156*, 1009–1014. [CrossRef]
48. Nightingale, A.M.; Hassan, S.-U.; Warren, B.M.; Makris, K.; Evans, G.W.H.; Papadopoulou, E.; Coleman, S.; Niu, X. A Droplet Microfluidic-Based Sensor for Simultaneous in Situ Monitoring of Nitrate and Nitrite in Natural Waters. *Environ. Sci. Technol.* **2019**, *53*, 9677–9685. [CrossRef]
49. Pires, N.M.M.; Dong, T.; Yang, Z. A Fluorimetric Nitrite Biosensor with Polythienothiophene-Fullerene Thin Film Detectors for on-Site Water Monitoring. *Analyst* **2019**, *144*, 43. [CrossRef]

4.4 Extraction of Soil Solution into a Microfluidic Chip

4.4.1 Introduction

S. Böckmann, I. Titov, and M. Gerken, "Extraction of Soil Solution into a Microfluidic Chip," AgriEngineering, 2021, doi: 10.3390/agriengineering3040049.

Statement about the own contribution:

Conceptualization	Planning	Implementation	Manuscript preparation
High	High	Moderate	High

- Design and modeling of the miniaturized soil solution extraction unit
- Planning of the work and student supervision in fabrication and characterization of the system
- Morphological characterization of the aluminum oxide ceramic on an atomic force microscope (AFM) and the characterization of the hydrophobicity of the material
- Manuscript preparation and revision

4.4.2 Abstract

In this publication the fabrication and function of a microfluidic soil-solution extraction chip was demonstrated. This chip consists of a PDMS microfluidic unit, fabricated on a 25 mm × 25 mm glass substrate and a porous ceramic filter in the inlet for in situ extraction of soil solution. The filter is a hydrophilic Al_2O_3 ceramic and has an average pore size of 1 µm. For sampling of soil

water, the vacuum inside the ceramic was applied by a compact and low-power peristaltic pump. Firstly, the paper shows a detailed characterization of the ceramic using confocal laser scanning microscopy (CLSM), atomic force microscopy (AFM) and a contact angle measurement instrument. Secondly, soil solution extraction experiments were applied with different soil samples as proof-of-concept. A particular focus was placed on the soil moisture necessary for device operation, as well as on the extraction speed and volume. During the experiments the inlet of the soil extraction unit was placed inside the soil and a constant suction was applied. The soil moisture was subsequently increased by adding water to the sample. As expected the results indicate, that the amount of added water is highly dependent on water-holding capacity of the soil type, which can be referred to the capillary matric potential of soil [67]. In all experiments, soil water was extracted successfully from the soil into the microfluidic chip. The necessary level of soil moisture was determined to be approximately 13 Vol.-% for silt, 11 Vol.-% for garden soil, and 8 Vol.-% for sand. The extraction rate was observed to be within the μL/min range. The proposed soil-solution extraction unit is particularly suited to extracting water in the non-equilibrium state after watering the field or a rainfall [68].

4.4.3 Published Paper

AgriEngineering

MDPI

Article

Extraction of Soil Solution into a Microfluidic Chip

Sönke Böckmann, Igor Titov * and Martina Gerken

Integrated Systems and Photonics, Faculty of Engineering, Kiel University, 24118 Kiel, Germany; soenke.boeckmann@icloud.com (S.B.); mge@tf.uni-kiel.de (M.G.)
* Correspondence: igti@tf.uni-kiel.de

Abstract: Collecting real-time data on physical and chemical parameters of the soil is a prerequisite for resource-efficient and environmentally sustainable agriculture. For continuous in situ measurement of soil nutrients such as nitrate or phosphate, a lab-on-chip approach combined with wireless remote readout is promising. For this purpose, the soil solution, i.e., the water in the soil with nutrients, needs to be extracted into a microfluidic chip. Here, we present a soil-solution extraction unit based on combining a porous ceramic filter with a microfluidic channel with a 12 µL volume. The microfluidic chip was fabricated from polydimethylsiloxane, had a size of 1.7 cm × 1.7 cm × 0.6 cm, and was bonded to a glass substrate. A hydrophilic aluminum oxide ceramic with approximately 37 Vol.-% porosity and an average pore size of 1 µm was integrated at the inlet. Soil water was extracted successfully from three types of soil—silt, garden soil, and sand—by creating suction with a pump at the other end of the microfluidic channel. For garden soil, the extraction rate at approximately 15 Vol.-% soil moisture was 1.4 µL/min. The amount of extracted water was investigated for 30 min pump intervals for the three soil types at different moisture levels. For garden soil and sand, water extraction started at around 10 Vol.-% soil moisture. Silt showed the highest water-holding capacity, with water extraction starting at approximately 13 Vol.-%.

Keywords: sensor systems; microfluidics; agricultural engineering; soil properties; soil moisture

Citation: Böckmann, S.; Titov, I.; Gerken, M. Extraction of Soil Solution into a Microfluidic Chip. *AgriEngineering* **2021**, *3*, 783–796. https://doi.org/10.3390/agriengineering3040049

Academic Editors: Pantelis E. Barouchas, Ioannis L. Tsirogiannis, Vasileios Tzanakakis and Ioannis Anastopoulos

Received: 6 August 2021
Accepted: 9 October 2021
Published: 14 October 2021

1. Introduction

Continuous monitoring of soil parameters such as moisture, temperature, pH, or nitrate level is essential for resource-efficient and environmentally sustainable agriculture. Plants are remarkably sensitive to nutrients such as N, P, K, and Fe, which affect the root development in various ways [1]. A monitoring of the nutrients inside the soil allows for a precise nutrient application in agriculture [2]. However, overfertilization is a well-known problem resulting in the accumulation of agricultural chemicals in the groundwater. Hallberg reported in 1989 about 39 pesticides in the groundwater of 34 states or provinces of the United States, with nitrate as one of the common agricultural chemicals [3]. In the following, we first review the current state of the art in the determination of chemical soil properties, and subsequently introduce an extraction unit suitable for automated soil-solution extraction into a microfluidic system. This unit is highly suitable for integration with lab-on-a-chip systems already introduced in the literature recently and discussed below.

For the measurement of physical parameters, such as moisture and temperature, sensors for the continuous in situ measurement are available on the market; however, the analysis of chemical parameters such as the soil nutrients nitrate or phosphate is today based on soil or soil-solution sample extraction in the field and analysis in the laboratory. Singh et al. [4] provided a comprehensive review of soil-sampling methods for laboratory analysis. Weihermüller et al. reviewed methods for continuous and discontinuous extraction of soil solution based on suction from the soil [5]. Details on the correct installation of porous ceramic cups for soil-water sampling were discussed by Curley et al. [6]. It is known from these studies that biasing effects due to the sampling method must be considered [5,6].

Additional sample alteration occurs during transport and storage of samples before analysis due to the ongoing chemical and physical processes in soil samples. Therefore, efforts have been made to allow for point-of-source and portable soil-analysis systems.

Point-of-source analysis systems promise fast results on fresh, unaltered samples. Here, a microfluidic approach is particularly suitable to reduce the size of the analysis system, as well as the needed sample volume. Chen et al. [7] reported on an integrated soil water potential sensor for continuous in situ monitoring. Kim et al. [8] demonstrated a microfabricated nitrate sensor that used double-potential-step chronocoulometry. The systems by Xu et al. [9] and Kokkinis et al. [10] were based on electrophoresis of charged ions in a capillary for measurement of ion concentrations. The measurement of nitrate (NO_3^-), sulfate (SO_4^{2-}), and dihydrogen phosphate ($H_2PO_4^-$) is shown. Dudala et al. [11] reported on a microfluidic-based standalone system for multiplexed detection of nitrite, pH, and the electrical conductivity of the soil solution. Thus, methods for point-of-source analysis systems are available. However, all of the demonstrated measurements relied on the manual preparation of the sample. For example, in the approach by Dudala et al., the sample had to be prepared by mixing soil with DI water and following a filtration protocol with Whatman filter papers. Our aim is to realize a system that does not require manual sample preparation.

Based on our experience in biomedical lab-on-chip devices for multiplexed detection [12,13] and integrated optical measurement systems [14], we aimed at developing a multiplex microfluidic chip for continuous in situ soil nutrient measurements. We planned to use the established analysis methods, but for the continuous measurement, the task of automated extraction of soil solution into the microfluidic systems had to be solved. Xu et al. [9] presented a first step in this direction by attaching a ceramic capillary tube to a polyetheretherketone (PEEK) tubing and delivering the sample solution to the microfluidic chip with a vacuum pump. For a new sample, the entire tubing volume had to be refilled, in addition to the microfluidic chip, in this approach. An analysis of the necessary solution volume was not presented. In addition, no investigation was shown for different soil types. Here, we present a microfluidic chip with an integrated porous ceramic filter for in situ extraction of soil solution. To our knowledge, such a system is presented for the first time and no prior data exists on the performance of an extraction unit integrated with a microfluidic chip for different soil types. This system was devised such that as little sample solution was necessary as possible. In Section 2, we discuss the choice of porous ceramic filter, the fabrication procedure of the soil-solution extraction unit, the experimental hardware setup, and the characterization procedure for measurements with different soil samples. In Section 3, the experimental results are described. A particular focus is placed on the soil moisture necessary for device operation, as well as on the extraction speed and volume. Section 4 presents a discussion of the results, and Section 5 draws conclusions.

The extraction unit presented here is the missing link between the microfluidic analysis systems already known and the bulky automated soil solution extraction units utilized for laboratory sample extraction. It is the next step towards an automated and continuous in situ soil nutrient detection unit for smart agriculture.

2. Experimental Methods

2.1. Porous Ceramic Filter

Hydrophilic materials, such as porous ceramics, have the ability to transport a polar liquid by capillary forces due to the charged surface inside the pore matrix [15]. This effect is called wicking, and can be described by the Washburn equation [16,17]. We chose a hydrophilic aluminum oxide ceramic as a porous water-permeable filter membrane. Cui et al. [18] used a similar ceramic in a miniature tensiometer report for soil-suction monitoring in the field. Ceramics are well suited to collecting soil samples for the detection of anions (NO_3^-, SO_4^{2-}) as well. The sorption of the elements is negligible due to the inertness of the ceramic material [19,20]. Soil solution investigations for trace elements with an Al_2O_3 ceramic were reported in the past [21,22]. Additionally, Silkworth and Grigal

showed a significantly higher ion concentration by collecting the soil solution with small samplers than for those collected by larger ones [23]. Thus, the miniaturization of the soil samplers is promising.

We used a hydrophilic aluminum oxide ceramic (Keralpor 99, 99.5% Al_2O_3, Kerafol Keramische Folien GmbH & Co. KG, Eschenbach in der Oberpfalz, Germany) with a size of 3 mm × 2.5 mm × 2 mm (length × width × height). According to the datasheet, the porosity had a value of approximately 36–38 Vol.-%, an average pore size of 1 µm, and a gross density of 2.56 g/cm^3. The surface roughness was approximately 0.7 µm. In the following figures, we present the characterization data in order to show the structure of the ceramic filter. Figure 1a–c show a morphological characterization of the Al_2O_3 ceramic obtained with confocal laser scanning microscopy (CLSM) and atomic force microscopy (AFM). In Figure 1a,b the grainy structure and statistically distributed holes can be observed. Figure 1c shows a zoom-in obtained with AFM. In the image, a pore is visible in the upper right corner.

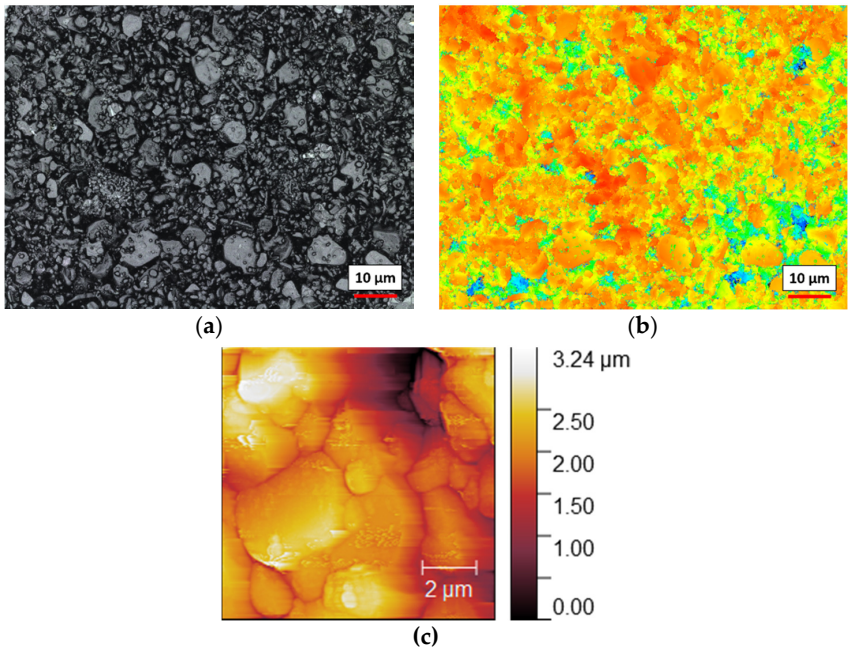

Figure 1. Morphological characterization of the Al_2O_3 porous ceramic filter: (**a**) confocal laser scanning microscopy (CLSM) images with 150× magnification show the pressed Al_2O_3 grains of different sizes; (**b**) the height profile of the same section; (**c**) atomic force microscopy (AFM) scan images of a 10 µm × 10 µm area. The zero reference was set on lowest point of the picture. A pore is visible in the upper right corner.

For characterization of the hydrophilic behavior, a 10 µL drop of water was placed on the dry Al_2O_3 ceramic. For comparison, a second drop was placed on a hydrophobic polycarbonate surface. The evolution of the drop shape was recorded with a contact-angle measurement instrument (OCA 50 AF, DataPhysics Instruments GmbH, Filderstadt, Germany). Figure 2a,b show both drops at 0 s and at 0.8 s after placement of the drop on the ceramic. The quick absorption into the ceramic was clearly observed, and the 10 µL drop disappeared within approximately 1.6 s.

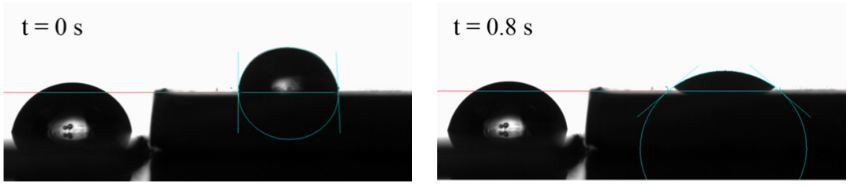

(**a**) (**b**)

Figure 2. Images of two 10 µL water drops on a hydrophobic polycarbonate (left) as a reference, and the hydrophilic Al_2O_3 ceramic for different times: (**a**) a snapshot of the first water ceramic contact (t = 0 s); (**b**) the drops after approximately 0.8 s. After approximately 1.6 s, the drop on the ceramic was fully absorbed.

From the porosity given in the datasheet and the volume of the ceramic filter, we calculated a solution volume of approximately 6 µL to fill the ceramic filter piece. In order to verify this volume, we measured the weight of the dehydrated filter (70.6 mg) and the fully saturated filter (84.3 mg) on a precision scale. This measurement had a significant systematic error, as water also wetted the surface of the ceramic, forming a puddle at the bottom. Thus, the water volume of approximately 13.7 µL obtained by weighing was an upper bound, and we believe the calculated 6 µL volume was a better estimate. This volume in the low µL range did not add significantly to the sample volume needed for the soil-solution analysis systems demonstrated so far [8–11].

2.2. Extraction Device Fabrication

The soil-solution extraction unit was fabricated with polydimethylsiloxane (PDMS) on a glass substrate. Figure 3a,c show a photograph and a schematic of the solution extraction device. The PDMS microfluidic chip was molded by using a Teflon mold as shown in Figure 3b, fabricated with a milling machine. It had a 12 mm microfluidic channel for extracted water transport with a quadratic cross section of 1 mm × 1 mm; i.e., the channel had a volume of 12 µL. The PDMS chamber was prepared by pouring the prepolymer of PDMS (SYLGARD® 184, Merck KGaA, Darmstadt, Germany) into the Teflon mold. It was hardened by baking in an oven at 90 °C for 1 h, and released after cooling down from the mold by peeling off from the master. The inlet of the fluidic was punched out with a biopsy punch (2 mm) and glued airtight with the 3 mm × 2.5 mm × 2 mm Al_2O_3 ceramic filter piece. Additionally, we drilled a port on the bottom side of the substrate and connected a silicone tube as the outlet.

As the final step, the PDMS microfluidic chip with the ceramic filter at the inlet was attached to the glass substrate by using an epoxy adhesive. For a more complex microfluidic system, the bonding is preferentially done by an oxygen plasma treatment of the PDMS surface [9].

2.3. Hardware Setup

We realized the measurement setup depicted in Figure 4 for characterizing the water extraction unit. The purpose of these experiments was to determine the necessary soil moisture level for extraction to begin and to measure the extraction speed. The tube at the bottom of the glass substrate was connected to a low-power miniature peristaltic pump (RP-QX1.2N, Ring Pump, Aquatech Co., Ltd., Osaka, Japan) to create suction. We used a Raspberry Pi 4 system and a motor driver (TB6612, Adafruit Industries) to control the peristaltic pump and read the soil-moisture sensor (SMT100, Truebner GmbH, Bad Schwartau, Germany). The SMT100 measured the volumetric water content and the temperature in the soil near the measuring surface based on time-domain reflectometry (TDR) and frequency domain reflectometry (FDR). The low-power peristaltic pump (0.36 W at 3 V) generated a maximum pump pressure of 0.5 bar (50 kPa). The extraction of soil solution was achieved by the underpressure inside the microfluidic channel while pumping.

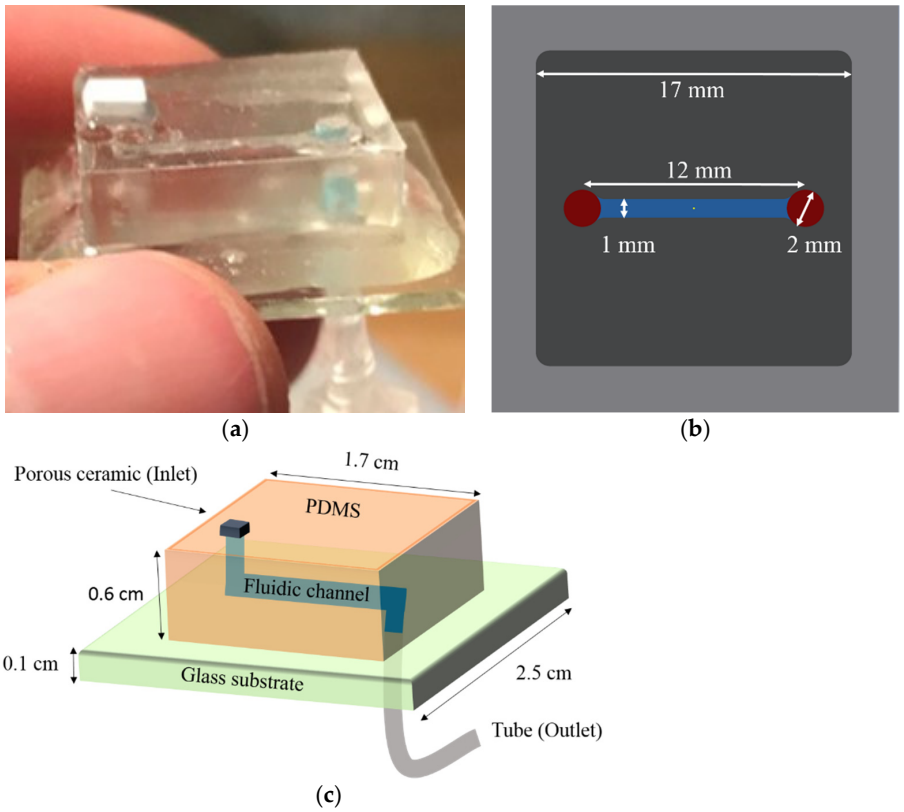

Figure 3. (**a**) Photograph of the soil-solution extraction device. (**b**) mold schematic for fabrication of the PDMS microfluidic device. The 12 mm fluidic channel had a 1 mm × 1 mm channel cross section. (**c**) Schematic view of the full water-extraction device.

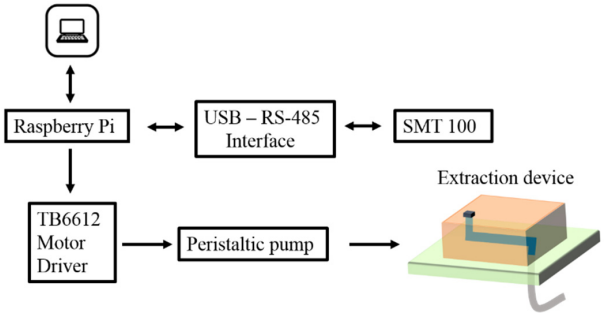

Figure 4. Hardware setup for testing the soil-solution extraction system. A miniature peristaltic pump and a reference soil-moisture sensor SMT100 were controlled by a Raspberry Pi 4 system.

2.4. Procedures for Soil-Sample Experiments

To estimate the behavior of our system, we investigated the extraction of soil solution with different types of soil. The tested soil types were silt, garden soil, and sand, chosen for their different water-holding capacities (Figure 5). The samples were collected in the field and separated (except garden soil) by wet sieving into their components, without further analysis of the soil components. Here, we examined the correlation between the soil moisture and the amount of extracted soil solution for a given pump duration.

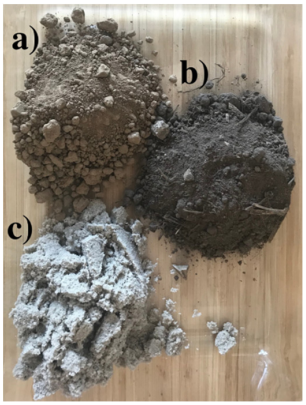

Figure 5. Tested soil types: (**a**) silt; (**b**) garden soil; (**c**) sand.

Figure 6 shows a photograph of the experimental setup with garden soil. The garden soil sample was piled up in a plastic box. The extraction device and the soil-moisture sensor SMT100 were installed adjacent to each other. Good soil contact was essential for the reference sensor and the porous ceramic of the extraction device, since larger air inclusions can lead to a lower water extraction. Thus, care should be taken in placing the sensor to avoid a larger air gap. As shown in Section 2.1, it was not problematic if the sensor was dry at the beginning, as the wicking also began for a dry ceramic filter.

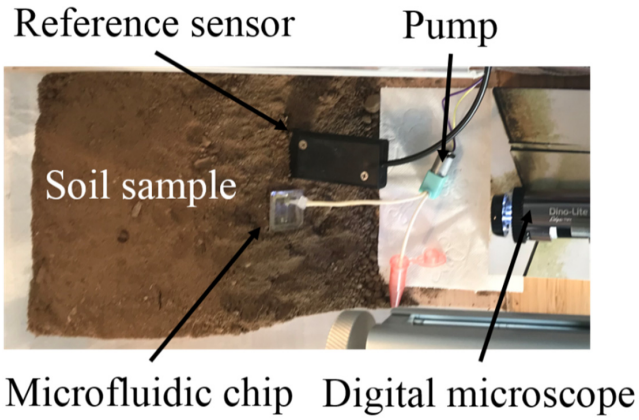

Figure 6. Characterization setup for soil-solution extraction unit. This garden soil sample was prepared in a plastic box (30 cm × 16 cm × 12 cm). The upper side of the device was pushed approximately 5 mm into the soil.

All three samples were prepared with the same volume of approximately 2500 cm^3. For reproducibility of the initial filter condition in repeated measurements, the aluminum oxide membrane was moistened at the beginning of the experiments. As discussed in Section 2.1, we could also use a dry filter, as this was filled quickly by wicking. We chose the wetting method, as the integrated filter could not be dried on a hot plate, and drying without temperature would require much more time than wetting. Furthermore, we measured the initial moisture content of the soil sample. Next, the effect of changing water content was analyzed by subsequently adding 100 mL of water on top of the soil sample with a spray bottle. After 15 min, we measured the moisture condition and activated the pump for 30 min. Hereafter, the pump was separated from the extraction device in order to transfer the extracted water to a beaker. To keep the contact condition between the soil and the microfluidic chip, we left the device inside the soil and evaluated the solution content inside the pump tube only.

The procedure of adding 100 mL of water with the spray bottle, pumping, and measuring the extracted water amount was iterated until the water-holding capacity of the soil was exceeded and the water ran out at the lowest point of the sample.

For characterization and better understanding of the system, the extraction of water into the microfluidic was filmed with a digital microscope (Dino-Lite AM7115MZTL, Bürklin GmbH & Co. KG, Oberhaching, Germany). We stress that the entire procedure of 30 min of pumping, transfer of the extracted water to a beaker, and filming with the digital microscope was only performed for extraction-unit characterization. For a field-deployed system, it would simply be required to add a pump to the microfluidic chip for suction and run the pump until the desired volume is extracted.

3. Experimental Results

3.1. Water Extraction into the Microfluidic Chip

Water was successfully extracted from all three soil types into the microfluidic chip. This demonstrated that the soil-extraction unit was functional for a sufficient moisture level. The following experiments show the beginning of the solution extraction at a 15 Vol.-% moisture level after adding 300 mL of water. Figure 7a–d show a time sequence of the extraction process into the microfluidic channel for garden soil. The 12 µL volume of the microfluidic channel was filled after approximately 8 min.

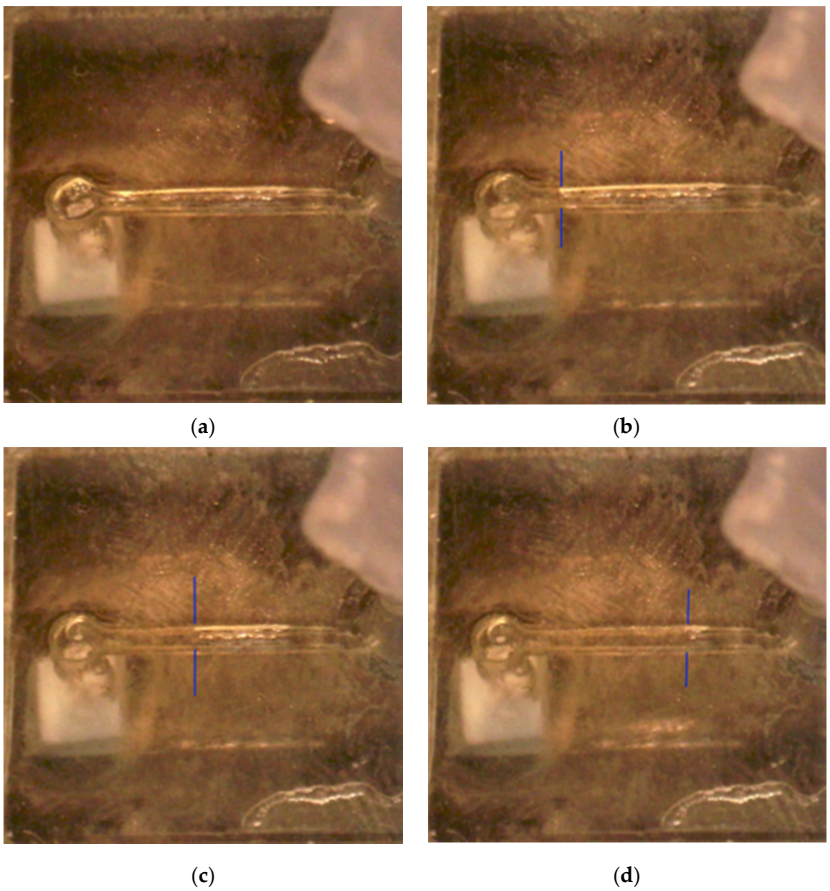

(**a**) (**b**)

(**c**) (**d**)

Figure 7. (**a**–**d**) Images of the garden soil solution extraction process after: (**a**) 0 min; (**b**) 1.5 min; (**c**) 2.5 min; and (**d**) 4.5 min. The position of the water column was barely visible, and is marked with the blue lines. The microfluidic channel was filled after approximately 8 min.

Figure 8 presents a plot of the liquid propagation inside the microfluidic device during the extraction measurement. The plot shows the filling of the 12 mm channel within 512 s. The analyzed distances were directly translated into the amount of extracted soil solution by considering the channel cross section. We observed an approximately linear filling behavior of the device with time. From the data, an extraction rate of approximately 1.4 µL/min was deduced. From these experiments, we expected an extraction volume of approximately 40 µL after the 30 min extraction interval for 300 mL of added water.

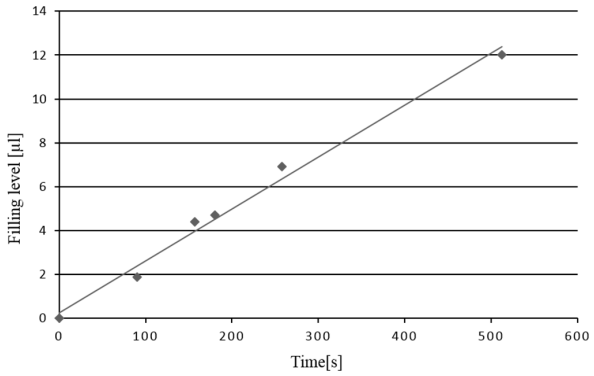

Figure 8. Evaluation of the microfluidic filling level. The data show the propagation of the soil solution over the 12 mm channel. The volume was calculated by analyzing the microscope images.

3.2. Experiments with Different Soil Types

For comparison of water extraction from different soil types, we always extracted water for 30 min and measured the amount of extracted solution in the tube as described in Section 4.2. Thus, this water volume was in addition to the channel volume. The temperature of the samples was consistently between 21 °C and 22 °C. Table 1 gives the experimental results for the extracted soil water from the three different types of soil.

Table 1. Experimental series of water extraction for different soil moisture levels in three types of soil. The moisture level was increased by adding water in steps. The volume of extracted solution for a 30 min pump period was measured. As the experiment was stopped at different amounts of added water, we do not have values for all fields.

	Sand		Garden Soil		Silt	
Added Water (mL)	**Measured Moisture (Vol.-%)**	**Extracted Solution (mL)**	**Measured Moisture (Vol.-%)**	**Extracted Solution (mL)**	**Measured Moisture (Vol.-%)**	**Extracted Solution (mL)**
0	3	0	2	0	1	0
100	5	0	5	0	1	0
200	8	0.1	11	0.1	3	0
300	10	0.1	15	0.1	9	0
400	14	0.1	19	0.17	11	0
500	18	0.1	24	0.19	13	0.1
600	22	0.15	-	-	18	0.08
700	31	0.15	-	-	23	0.1
800	-	-	-	-	28	0.15
900	-	-	-	-	33	0.19

We observed that the amount of added water resulted in different moisture conditions of the soil samples. The water-holding capacities of the soil samples were different, as expected. Therefore, the extracted solution was stagnant when initially adding water. The reason for this effect can be described by the capillary matric potential of soil [24]. The movement of soil water inside the soil matrix typically takes place from wet to drier regions. This is referred to as different matric potentials of the soil, which describes the attractive force between the particles and water inside the soil. Dryer soil regions have higher matric potential. For sampling of soil water, the forces generated by the applied vacuum inside the ceramic must be higher than the capillary matric potential of the soil. Since we kept the suction constant, the moisture had to be increased by adding water to the sample and

lowering the matric potential. The different values within the samples resulted from the texture dependency of the capillary forces inside the soil matrix. Silt showed the highest water-holding capacity. Due to the higher soil moisture tension, the moisture level was increased to approximately 13 Vol.-% after adding 500 mL of water. At this point, the extraction of water into the microfluidic device began. In contrast to silt, the extraction of the soil solution began after adding 200 mL of water to garden soil and sand at 11 Vol.-% and 8 Vol.-%, respectively.

3.3. Analysis of Measurement Variability

To investigate the measurement variability in this experimental procedure, we conducted the experiment with garden soil two more times. The garden soil was changed between the measurements. Table 2 shows the data comparison of the three measurement iterations. We observed that the initial water extraction began at different moisture conditions. As already shown in Table 1, the extraction began at 11 Vol.-% for the first run with garden soil. For the second and the third iterations, we began extracting soil water at 14 Vol.-% and 6 Vol.-%, respectively.

Table 2. Experimental series of repeated water extraction from garden soil for different soil moisture levels. The moisture level was increased by adding water in steps. The volume of extracted solution for a 30 min pump period was measured.

	1st Iteration		2nd Iteration		3rd Iteration	
Added Water (mL)	**Measured Moisture (Vol.-%)**	**Extracted Solution (mL)**	**Measured Moisture (Vol.-%)**	**Extracted Solution (mL)**	**Measured Moisture (Vol.-%)**	**Extracted Solution (mL)**
0	2	0	2	0	3	0
100	5	0	3	0	3	0
200	11	0.1	8	0	6	0.02
300	15	0.1	14	0.02	15	0.04
400	19	0.17	18	0.03	23	0.1
500	24	0.19	25	0.06	-	-

A possible reason for this divergence was the uneven distribution of water bound inside the soil, as well as air bubbles. We expect that the small microfluidic extraction unit with ceramic inlet was more sensitive to inhomogeneous water distribution, as the sampled soil volume was much smaller than for the rather large reference sensor SMT100. Additionally, the structure of the soil also had a great impact on capillary effects between the soil solution and the porous membrane. As we changed the soil between iterations and repositioned the microfluidic extraction unit, this contact was not constant between iterations.

Figure 9a shows the correlation between the added water on top of the soil sample and the measured soil moisture with the reference sensor. We plotted all three measurements with garden soil to investigate the error propagation within a measurement. The plot showed a moderate deviation. We suggest this was mainly due to the inhomogeneous water distribution inside the soil sample.

Figure 9b shows the amount of extracted soil solution after adding water. It was observed that the water extraction start points were different for the three soils, varying between 200 and 300 mL of added water. The small size of the membrane coupled with the water distribution variability inside the soil structure led to the variability in the extracted amount of water. At 400 mL of added water, the extracted water volume had the largest variability, with values between 0.03 mL and 0.17 mL.

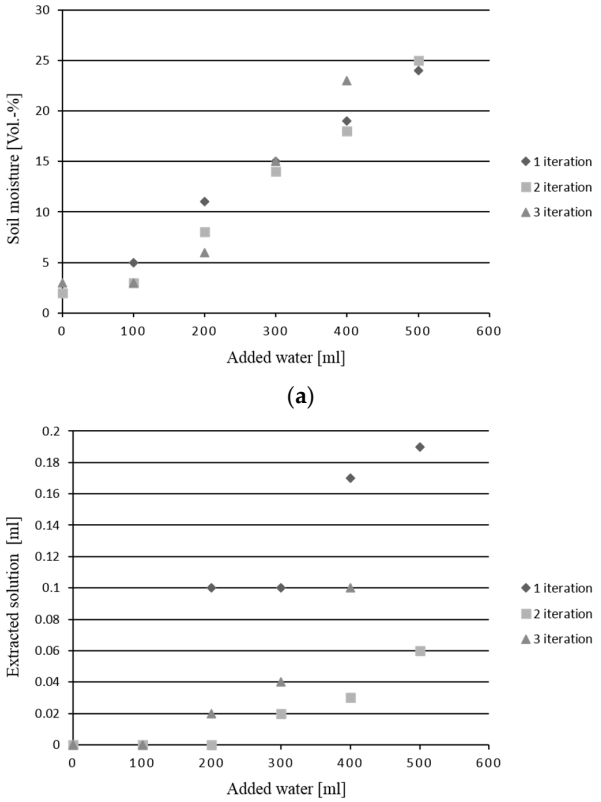

Figure 9. Evaluation of measurement variability: (**a**) soil moisture with added water; and (**b**) extracted soil solution with added water for three measurement iterations.

4. Discussion of Experimental Results

4.1. Necessary Soil-Moisture Level

In all experiments, soil water was extracted successfully from the soil into the microfluidic chip. The necessary level of soil moisture was determined to be approximately 13 Vol.-% for silt, 11 Vol.-% for garden soil, and 8 Vol.-% for sand. Therefore, the proposed soil-solution extraction unit is particularly suited to extracting water in the nonequilibrium state after watering the field or a rainfall. Since nutrients are particularly susceptible to leaching through the soil profile [25], this transfer of chemicals during rainfall is a promising circumstance for using in situ soil water samplers without applying high vacuum potentials for the suction lysimetric approach. Thus, the system becomes energy-efficient, and may be miniaturized. In-depth tests are still required to determine the temporal correlation between soil nutrients dissolved in the soil water and bound to the solid soil phase. Here, the proposed extraction unit could be used in combination with one of the microfluidic analysis systems developed by other groups to gain valuable insights into the soil dynamics by continuous in situ measurements.

4.2. Volume of Extracted Water

In the characterization experiments, extraction rates in the µL/min range were demonstrated. In microfluidic lab-on-chip systems, typically solution volumes in the µL range are used, and these volumes may be extracted within minutes. In addition, the amount of solution stored in the ceramic membrane must be exchanged for correct measurement of a given sampling time. For the characterization experiments, we moistened the ceramic filter in order to create reproducible conditions. As the ceramic filter stored approximately

6 µL, this volume had to be extracted in addition to the volume needed in the microfluidic chip. An even smaller ceramic filter may be used to reduce this volume further. In the experiments shown in Figure 2, it is visible that water extraction also began for a dry ceramic filter. Thus, it was not a fundamental problem if the filter was dry or air bubbles were in the soil. This only affected the amount of extracted water per time unit, and air inclusions had to be eliminated in the subsequent microfluidic chip.

4.3. Pump Choice for Field Deployment

For field deployment, the proposed extraction unit needs to be combined with a microfluidic analysis system and a pump. The compact and low-power (<360 mW) peristaltic pump used in the characterization experiments is one good choice, as long as the soil solution is extracted from well-watered soil. The peristaltic pump may also be integrated directly on the chip, or replaced with an even smaller actuator based on piezoelectric devices. For even further miniaturization, capillary pumping is of high interest [26]. For even lower system power levels, approaches for moving liquids inside a microfluidic system without using a pump may be considered [27,28]. Here, the possible operation time if using a porous PDMS sponge or a reinforced balloon must be compared to a battery-operated pump system. As long as the analysis system and communication system also require a battery, a miniature electric pump seems to be the best choice.

For extraction of soil solution from soil of a high matric potential, much higher suction forces are necessary, and a different approach with a stronger pump and wiring to a larger power supply is needed. Weihermüller [29] conducted silt numerical simulations using the physically based convection–dispersion equation (CDE). He showed that the amount of the extracted water increased with higher suction rates (approaching an asymptotic value of the system). Additionally, different soil samples showed, as expected, different extraction rates, with clay loam and sandy soil as the highest and the lowest, respectively. These simulations matched our results, since silt is a component of loam. Van der Ploeg and Beese made similar observations. They observed a nonlinear relation between the suction and the extracted water [30].

In our proof-of-principle experiments, we did not observe any coagulation effects. For long-term operation of the filter, fine soil particles may coagulate in the system. For cleaning of the system, approaches such as backflushing of the particles by reversing the flow direction of the peristaltic pump may be considered, and thus a pump and microfluidic system suitable for bidirectional operation is preferred for the next step of a long-term field test. In this context, it would also be interesting to investigate the influence of the best pore size in more detail. A careful balance between the pore size and the power consumption must be found for field application. The soil particle sizes range from 0.2 µm to 2 mm [31] for fine clay to very coarse sand, respectively. Higher pore sizes lead to detrimental filter quality, since more particles would enter the ceramic unit. Lower pore size would require higher suction potential at the ceramic/water interface; i.e., the setup would need a pump with higher power.

Finally, the pump cost was the dominant cost factor in our current system. The overall system cost of the pump, electronics, and microfluidics for our proof-of-principle extraction system was approximately EUR 100. Here, the pump accounted for around 70% of the costs. Thus, for a cost-efficient system, the price of the pump is an important factor, and the necessary performance parameters must be carefully evaluated in long-term experiments to reduce cost.

4.4. Susceptibility to Inhomogeneities

The repeated experiments using garden soil showed that due to the small collection volume, the microfluidic system was inherently susceptible to inhomogeneities in the soil. Additionally, it must be considered that the soil properties and moisture level vary from one area to another on a single agricultural field. Shallow regions in the field may have a much higher moisture level than elevated regions. Weihermüller depicted in his PhD thesis [29]

that the reliability of suction cups and commercially available lysimeters is increased by the deployment of numerous samplers to obtain a good average. Thus, the problem of dealing with inhomogeneities is known from larger systems, and we propose a distributed network of miniaturized sensors for spatially resolved monitoring of soil nutrients.

In addition, it has been recognized previously in the literature that the soil-solution extraction method may bias the result of the nutrient concentrations derived for the soil [5,6]. These effects were also expected for our approach, and need to be analyzed in field studies. Relative concentrations of different nutrients provide additional information. Contrary to the traditional approach of calculating the nutrient concentration for a fixed soil volume or mass, in soil-solution analysis approaches, the concentration is related to the solution volume [9,10]. Regarding the different amounts of extracted solution in the repeated experiments shown in Figure 9, it was concluded that a monitoring of the extracted water amount should be implemented to determine the necessary pump duration.

5. Conclusions

In conclusion, we demonstrated the fabrication and function of a microfluidic soil-solution extraction chip. Soil water was extracted successfully from three types of soil—silt, garden soil, and sand—with a rate in the µL/min range. This device is promising as an extraction unit for continuous sensing systems, as well as for discrete time-point sensing in agriculture. The proposed extraction unit may be combined with any of the microfluidic analysis systems proposed in the literature [8–11]. Low-power and long-range data transmission standards such as Long Range (LoRa) are particularly suitable, and the Internet of Underground Things (IoUT) is being established [32,33]. Combining the proposed low-power soil-solution extraction unit, a low-power microfluidic analysis system and a low-power communication standard brings a wireless, low-maintenance stand-alone system for chemical nutrient analysis into reach. As the next steps, this integration should be accomplished, and extensive field testing be performed.

The deployment of microfluidic systems in the agricultural field is not only limited to investigations on soil solution. Studies on environmental organisms, root bacteria, and simulating microbial ecology in soil systems were carried out in the past two decades [34–36]. Stanley et al. [37] provide a critical review on Soil-on-a-Chip or Plant-in-Chip technologies for soil organisms studies and their interactions with the environment. A merging of the two research areas promises additional insights.

Author Contributions: Conceptualization, S.B., I.T. and M.G.; data curation, S.B. and I.T.; formal analysis, I.T. and M.G.; funding acquisition, M.G.; investigation, I.T. and M.G.; methodology, S.B.; project administration, I.T. and M.G.; resources, I.T. and M.G.; supervision, I.T. and M.G.; validation, I.T. and M.G.; visualization, S.B.; writing—original draft, I.T. and M.G.; writing—review and editing, I.T. and M.G. All authors have read and agreed to the published version of the manuscript.

Funding: This work was supported in part by ZIM (Project AuToilette, ZF4558802RH8). The authors also acknowledge financial support by DFG within the funding programme Open Access Publizieren.

Institutional Review Board Statement: Not applicable.

Informed Consent Statement: Not applicable.

Acknowledgments: The authors acknowledge the Institute of Plant Nutrition and Soil Science at Kiel University for providing soil samples, and Kerafol Keramische Folien GmbH & Co. KG for the test samples of Keralpor 99.

Conflicts of Interest: The authors declare no conflict of interest.

References

1. Forde, B.; Lorenzo, H. The nutritional control of root development. In *Interactions in the Root Environment: An Integrated Approach*; Springer: Dordrecht, The Netherlands, 2002; pp. 51–68. [CrossRef]
2. Robert, P.C. Precision agriculture: A challenge for crop nutrition management. *Plant Soil* **2002**, *247*, 143–149. [CrossRef]

3. Hallberg, G.R. Pesticides pollution of groundwater in the humid United States. *Agric. Ecosyst. Environ.* **1989**, *26*, 299–367. [CrossRef]
4. Singh, G.; Kaur, G.; Williard, K.; Schoonover, J.; Kang, J. Monitoring of Water and Solute Transport in the Vadose Zone: A Review. *Vadose Zone J.* **2017**, *17*, 160058. [CrossRef]
5. Weihermüller, L.; Siemens, J.; Deurer, M.; Knoblauch, S.; Rupp, H.; Göttlein, A.; Pütz, T. In Situ Soil Water Extraction: A Review. *J. Environ. Qual.* **2007**, *36*, 1735–1748. [CrossRef]
6. Curley, E.M.; O'flynn, M.; McDonnell, K. Porous Ceramic Cups: Preparation and Installation of Samplers for Measuring Nitrate Leaching. *Int. J. Soil Sci.* **2009**, *5*, 19–25. [CrossRef]
7. Chen, Y.; Tian, Y.; Wang, X.; Wei, L.; Dong, L. Miniaturized, Field-Deployable, Continuous Soil Water Potential Sensor. *IEEE Sens. J.* **2020**, *20*, 14109–14117. [CrossRef]
8. Kim, D.; Goldberg, I.B.; Judy, J.W. Microfabricated electrochemical nitrate sensor using double-potential-step chronocoulometry. *Sens. Actuators B Chem.* **2009**, *135*, 618–624. [CrossRef]
9. Xu, Z.; Wang, X.; Weber, R.J.; Kumar, R.; Dong, L. Nutrient Sensing Using Chip Scale Electrophoresis and In Situ Soil Solution Extraction. *IEEE Sens. J.* **2017**, *17*, 4330–4339. [CrossRef]
10. Kokkinis, G.; Kriechhammer, G.; Scheidl, D.; Wilfling, B.; Smolka, M. Towards the Commercialization of a Lab-on-a-Chip Device for Soil Nutrient Measurement. In *Information and Communication Technologies in Modern Agricultural Development, Proceedings of the 8th International Conference (HAICTA 2017), Chania, Greece, 21–24 September 2017*; Springer: Cham, Switzerland, 2019; pp. 118–130.
11. Dudala, S.; Dubey, S.K.; Goel, S. Microfluidic Soil Nutrient Detection System: Integrating Nitrite, pH, and Electrical Conductivity Detection. *IEEE Sens. J.* **2020**, *20*, 4504–4511. [CrossRef]
12. Jahns, S.; Bräu, M.; Meyer, B.-O.; Karrock, T.; Gutekunst, S.B.; Blohm, L.; Selhuber-Unkel, C.; Buhmann, R.; Nazirizadeh, Y.; Gerken, M. Handheld imaging photonic crystal biosensor for multiplexed, label-free protein detection. *Biomed. Opt. Express* **2015**, *6*, 3724–3736. [CrossRef]
13. Jahns, S.; Gutekunst, S.B.; Selhuber-Unkel, C.; Nazirizadeh, Y.; Gerken, M. Human blood microfluidic test chip for imaging, label-free biosensor. *Microsyst. Technol.* **2016**, *22*, 1513–1518. [CrossRef]
14. Titov, I.; Kopke, M.; Schneidewind, N.C.; Buhl, J.; Murat, Y.; Gerken, M. OLED-OPD Matrix for Sensing on a Single Flexible Substrate. *IEEE Sens. J.* **2020**, *20*, 7540–7547. [CrossRef]
15. Joekar-Niasar, V.; Schreyer, L.; Sedighi, M.; Icardi, M.; Huyghe, J. Coupled Processes in Charged Porous Media: From Theory to Applications. *Transp. Porous Media* **2019**, *130*, 183–214. [CrossRef]
16. Li, Z.; Giese, R.F.; Oss, C.J.; Kerch, H.M.; Burdette, H.E. Wicking Technique for Determination of Pore Size in Ceramic Materials. *J. Am. Ceram. Soc.* **1994**, *77*, 2220–2222. [CrossRef]
17. Kissa, E. Wetting and Wicking. *Text. Res. J.* **1996**, *66*, 660–668. [CrossRef]
18. Suits, L.D.; Sheahan, T.C.; Cui, Y.-J.; Tang, A.M.; Mantho, A.T.; De Laure, E. Monitoring Field Soil Suction Using a Miniature Tensiometer. *Geotech. Test. J.* **2008**, *31*, 95–100. [CrossRef]
19. Spangenberg, A.; Cecchini, G.; Lamersdorf, N. Analysing the performance of a micro soil solution sampling device in a laboratory examination and a field experiment. *Plant Soil* **1997**, *196*, 59–70. [CrossRef]
20. Göttlein, A.; Hell, U.; Blasek, R. A system for microscale tensiometry and lysimetry. *Geoderma* **1996**, *69*, 147–156. [CrossRef]
21. Hädrich, F.; Stahr, K.; Zöttl, H.W. *Die Eignung von Al_2O_3-Keramik und Ni-Sinterkerzen zur Gewinnung von Bodenlösungen für die Spurenelementanalyse. Mitteilungen der Deutschen Bodenkundlichen Gesellschaft*; DBG: Bremen, Germany, 1977; No. 25-1; pp. 151–162.
22. Berger, W.; Kalbe, U. *"Saugsonden zur Untersuchung der Bodenwasserbeschaffenheit: Ein Überblick der Einsatzmöglichkeiten"*; TerraTech 11-12; Vereinigte Fachverlage GmbH: Mainz, Germany, 2004; pp. 8–12.
23. Silkworth, D.R.; Grigal, D.F. Field Comparison of Soil Solution Samplers. *Soil Sci. Soc. Am. J.* **1981**, *45*, 440–442. [CrossRef]
24. Warrick, A.W. *Soil Water Dynamics*; Oxford University Press: Oxford, UK, 2003. [CrossRef]
25. Kumar, A.; Kanwar, R.; Singh, P.; Ahuja, L. Evaluation of the root zone water quality model for predicting water and NO_3–N movement in an Iowa soil. *Soil Tillage Res.* **1999**, *50*, 223–236. [CrossRef]
26. Guo, W.; Hansson, J.; Van Der Wijngaart, W. Capillary pumping independent of the liquid surface energy and viscosity. *Microsyst. Nanoeng.* **2018**, *4*, 2. [CrossRef]
27. Thurgood, P.; Baratchi, S.; Szydzik, C.; Mitchell, A.; Khoshmanesh, K. Porous PDMS structures for the storage and release of aqueous solutions into fluidic environments. *Lab Chip* **2017**, *17*, 2517–2527. [CrossRef]
28. Thurgood, P.; Suarez, S.A.; Chen, S.; Gilliam, C.; Pirogova, E.; Jex, A.R.; Baratchi, S.; Khoshmanesh, K. Self-sufficient, low-cost microfluidic pumps utilising reinforced balloons. *Lab Chip* **2019**, *19*, 2885–2896. [CrossRef]
29. Weihermüller, L. Comparison of Different Soil Water Extraction Systems for the Prognoses of Solute Transport at the Field Scale Using Numerical Simulations, Field and Lysimeter Experiments. Ph.D. Dissertation, Rheinische Friedrich-Wilhelms-Universität, Bonn, Germany, 2005.
30. Van Der Ploeg, R.R.; Beese, F. Model Calculations for the Extraction of Soil Water by Ceramic Cups and Plates. *Soil Sci. Soc. Am. J.* **1977**, *41*, 466–470. [CrossRef]
31. Webster, R. Soil Sampling and Methods of Analysis—Edited by M.R. Carter & E.G. Gregorich. *Eur. J. Soil Sci.* **2008**, *59*, 1010–1011. [CrossRef]

32. Grunwald, A.; Schaarschmidt, M.; Westerkamp, C. LoRaWAN in a rural context: Use cases and opportunities for agricultural businesses. In Proceedings of the Mobile Communication—Technologies and Applications; 24. ITG-Symposium, Osnabrueck, Germany, 15–16 May 2019; pp. 134–139.
33. Salam, A.; Vuran, M.C.; Irmak, S. Di-Sense: In situ real-time permittivity estimation and soil moisture sensing using wireless underground communications. *Comput. Netw.* **2019**, *151*, 31–41. [CrossRef]
34. Parashar, A.; Pandey, S. Plant-in-chip: Microfluidic system for studying root growth and pathogenic interactions in Arabidopsis. *Appl. Phys. Lett.* **2011**, *98*, 263703. [CrossRef]
35. Massalha, H.; Korenblum, E.; Malitsky, S.; Shapiro, O.H.; Aharoni, A. Live imaging of root–bacteria interactions in a microfluidics setup. *Proc. Natl. Acad. Sci. USA* **2017**, *114*, 4549–4554. [CrossRef]
36. Aleklett, K.; Kiers, E.T.; Ohlsson, P.; Shimizu, T.S.; Caldas, V.E.; Hammer, E.C. Build your own soil: Exploring microfluidics to create microbial habitat structures. *ISME J.* **2018**, *12*, 312–319. [CrossRef]
37. Stanley, C.E.; Grossmann, G.; Solvas, X.C.I.; Demello, A.J. Soil-on-a-Chip: Microfluidic platforms for environmental organismal studies. *Lab Chip* **2016**, *16*, 228–241. [CrossRef]

4.5 UAV-Based Wireless Data Collection from Underground Sensor Nodes for Precision Agriculture

4.5.1 Introduction

L. Holtorf, I. Titov, F. Daschner and M. Gerken, "UAV-Based Wireless Data Collection from Underground Sensor Nodes for Precision Agriculture," AgriEngineering, 2023, doi: 10.3390/agriengineering5010022.

Statement about the own contribution:

Conceptualization	Planning	Implementation	Manuscript preparation
Moderate	High	Low	Low

- Planning and conceptualization of the project and student supervision in design, modeling and implementation of the measurement setup
- Equal contribution in data acquisition and analysis on antenna characterization and connectivity measurements between drone and sensor nodes on the Hohenschulen farm as the first author
- Partly preparation and revision of the manuscript

4.5.2 Abstract

In this publication three underground sensor nodes were designed to operate in-situ using the LoRa transmission standard to collect and forward measurement data to a ground station or a drone with a mounted LoRa receiver. The physical parameters of the soil were collected by commercial available moisture

and temperature sensors. This work shows the successful LoRa data transmission of sensor nodes buried in 30 and 60 cm depth and the characterization of signal strength (RSSI) dependency from the sensor burial depth, flying height of the drone and antenna orientation. The deployment of a drone as a gateway enables an increase of the communication range from 300 m to 1000 m, which shows a maximum readout distance of 550 m between the sensor node and the drone. The demonstrated communication setup based on LoRa transmission standard is a promising step towards a fully autonomous and compact monitoring systems of chemical soil parameters, such as nitrate, nitrite or phosphate.

4.5.3 Published Paper

AgriEngineering

MDPI

Article

UAV-Based Wireless Data Collection from Underground Sensor Nodes for Precision Agriculture

Lucas Holtorf [1], Igor Titov [1], Frank Daschner [2] and Martina Gerken [1,*]

[1] Integrated Systems and Photonics, Faculty of Engineering, Kiel University, 24118 Kiel, Germany
[2] Microwave Engineering, Faculty of Engineering, Kiel University, 24118 Kiel, Germany
* Correspondence: mge@tf.uni-kiel.de

Abstract: In precision agriculture, information technology is used to improve farm management practices. Thereby, productivity can be increased and challenges with overfertilization and water consumption can be addressed. This requires low-power and wireless underground sensor nodes for monitoring the physical, chemical and biological soil parameters at the position of the plant roots. Three ESP32-based nodes with these capabilities have been designed to measure soil moisture and temperature. A system has been developed to collect the measurement data from the sensor nodes with a drone and forward the data to a ground station, using the LoRa transmission standard. In the investigations of the deployed system, an increase in the communication range between the sensor node and the ground station, from 300 m to 1000 m by using a drone, was demonstrated. Further, the decrease in the signal strength with the increasing sensor node depth and flight height of the drone was characterized. The maximum readout distance of 550 m between the sensor node and drone was determined. From this, it was estimated that the system enables the readout of the sensor nodes distributed over an area of 470 hectares. Additionally, analysis showed that the antenna orientation at the sensor node and the drone influenced the signal strength distribution around the node due to the antenna radiation pattern. The reproducibility of the LoRa signal strength measurements was demonstrated to support the validity of the results presented. It is concluded that the system design is suitable for collecting the data of distributed sensor nodes in agriculture.

Keywords: precision agriculture; unmanned aerial vehicle (UAV); drone; LoRa; Internet of Things (IoT); Internet of Underground Things (IoUT)

Citation: Holtorf, L.; Titov, I.; Daschner, F.; Gerken, M. UAV-Based Wireless Data Collection from Underground Sensor Nodes for Precision Agriculture. *AgriEngineering* **2023**, *5*, 338–354. https://doi.org/10.3390/agriengineering5010022

Academic Editors: Muhammad Sultan, Yuguang Zhou, Redmond R. Shamshiri and Muhammad Imran

Received: 27 December 2022
Revised: 7 February 2023
Accepted: 8 February 2023
Published: 9 February 2023

1. Introduction

The world's growing population and limited natural resources increase the demand for precision agriculture. The goal is to improve farm management by using information technology in order to increase crop quality and profitability [1]. Additionally, the problems that arise with today's high yield agriculture can also be addressed. Overfertilization results in health hazards, pollution, reduced product quality and a loss of soil fertility [2]. The extensive, uncontrolled irrigation of cropland leads to the deterioration of water sources, salt build-up on fields and soil erosion [3].

The development of precise and cost effective sensing solutions is recognized as one of the key challenges for increasing the adoption of precision agriculture [1]. Monitoring soil parameters, such as moisture, temperature, pH, nitrate or nitrite, is crucial for efficient plant growth and root development [4]. This allows for the precise control of the nutrient content to enhance productivity [5]. Weather, management practices, different soil types and local topology can cause significant variations in the parameters of interest, even within a single agricultural field and over short timespans [6]. Traditional practices, such as in-situ measurements conducted by an appropriate operator or offsite laboratory analysis of soil samples, are not suitable for the spatial and temporal measurement densities required. Thus,

the use of distributed, independently operating sensor nodes with in-situ measurement capabilities is desired [7].

As the manual operation of wired sensor nodes deployed on large agricultural fields is both impractical and expensive, low-power and long-range data transmission standards, such as Long Range (LoRa), have been established for the transmission of sensor data [8,9]. The sensor nodes should not obstruct the normal work in the field, which introduces the need for wireless underground sensor nodes. Burying sensor nodes in the soil helps to protect them from extreme weather conditions and farm equipment [7]. A drawback is that the achievable communication distance is significantly reduced, because the soil introduces variable high path losses [10]. Researchers at the University of Applied Sciences in Osnabrück have proposed a system for data readout from a sensor buried 60 cm in the ground at a receiving station 350 m away using LoRa communication [8].

Typically, the distances in agriculture are significantly larger than 350 m. Thus, a drone can be a solution for the data collection of sensor nodes distributed in large areas without the need to install additional infrastructure. The deployment of unmanned aerial vehicles (UAVs) in the context of precision agriculture is becoming a valuable tool for farmers and researchers. Barbedo provides a comprehensive review on the use of UAVs for monitoring and assessing plant stresses [11]. Barnetson et al. measured plant pasture biomass and quality with a UAV [12]. Bukowiecki et al. used an UAV with an integrated camera for the estimation of the green area index (GAI) of winter wheat to calibrate the Sentinel-2 data for crop monitoring and yield prediction [13]. Fan et al. discuss plant classification based on drone data [14]. Quino et al. introduced drones in combination with RFID tags for taking a plant inventory [15]. The numerical fluid dynamics simulation by Marturano et al. investigates the air flow around a drone, which is relevant for the placement of sensors on drones [16].

The potential of combing drones with LoRa communication for data collection has recently been proposed in the literature. Behjati et al. demonstrated a system that used drones with an attached LoRaWAN® gateway to collect the data from water quality sensors and livestock monitoring equipment on a farm [17]. The authors investigated the packet loss performance of the LoRa connection, taking into account the different spreading factors and drone speeds. Additionally, they optimized the flight path to maximize the flight range of the fixed-wing vertical takeoff drone. The forwarding of the sensor data from the gateway to a server was conducted using LTE. Park et al. demonstrated a system for collecting environmental sensor data on a tree farm via LoRa using a drone with an attached LoRaWAN® gateway [18]. They successfully applied a proposed client-server communication scheme, but encountered some issues with the gateway in low temperature conditions and limitations of the flight time of the drone due to the additional weight.

Other groups have worked on different subproblems of the approach to collect sensor data with drones. Caruso et al. derived an analytical model for data acquisition with a drone and LoRa from a large regular grid of sensor nodes, as would be found in agriculture [19]. The model allowed for the determination of the optimal spacing of the sensor nodes, the time a sensor needs to be in range of a sensor node and the required velocity of the drone to optimize the probability of successful data collection.

Furthermore, Zhang et al. improved the UAV data collection efficiency of distributed sensor nodes [20]. They developed an algorithm to organize sensor nodes that are close to each other into clusters, with a cluster head that transmits the sensor data of the whole cluster to the drone. A genetic algorithm was then used to minimize the flight path of the UAV between the clusters. Additionally, an adaptive scheme for changing the transmission data rate based on the received signal strength and the signal to noise ratio was reported.

Pan et al. proposed a dynamic UAV speed control scheme in order to adapt to different sensor device densities [20,21]. Based on an analytical model of the connection situation, the number of successful sensor node connections per second was maximized.

Zorbas and O'Flynn worked on the problem of LoRa transmission packet collision when many sensor nodes are located in a specific area. Their protocol allowed for the data collection of 80 nodes in a 1500 m × 1500 m area without packet collisions [22].

In this paper, a system was investigated to collect the data from buried sensor nodes and forward that data to a ground station by using the LoRa transmission standard and a UAV. When operating such a system, a challenge is that it has to be designed in such a way that the data collection is secured while the minimizing battery consumption of the sensor nodes and taking into account the limited flight time of the drone. The necessary optimization of the readout scheme requires knowledge about the different influences on the LoRa transmission quality when the underground sensor node communicates with an aboveground UAV.

To the best of the authors' knowledge, there have not been many published experimental demonstrations on this topic. A similar setup using the NB-IoT standard has been analyzed in simulations by Castellanos et al. The authors demonstrated that an UAV could collect the data within 50 s from 2000 sensors buried in a grid with 10 m spacing under a 20 hectare potato field. Additionally, the impact of soil moisture on the number of successfully served sensor nodes due to changing damping has been shown [23].

Experimental work has recently been published by two other groups. Cariou et al. buried a sensor node at a depth of 15 cm and demonstrated the data collection capability of their system for flight heights of 20 m to 60 m and distances up to 150 m [24]. Hossain et al. developed a similar system and conducted measurements of the received signal strength of the LoRa packages close to the point where the node was buried [25]. A detailed comparison between the system architectures and methods used and the approach described here is given in Section 4.

The general setup (see Figure 1a) consists of a sensor node buried in a field that transmits a series of measurements upon the request of the repeater drone, using the LoRa transmission standard. The repeater drone receives the data and forwards it immediately to the user ground station. Low power sensor nodes were implemented and a protocol for their energy efficient operation was developed. In several experiments, different aspects of the system described were analyzed:

- Dependency of received LoRa signal strength on flight height of the drone and on the burial depth of the sensor node.
- Demonstration of the range extension capability.
- Determination of the maximum distance between the sensor node and drone with the setup.
- Investigation of the effect of the antenna placement inside the sensor node on the received LoRa signal strength.
- Investigation of the repeatability of the signal strength over distance measurements.

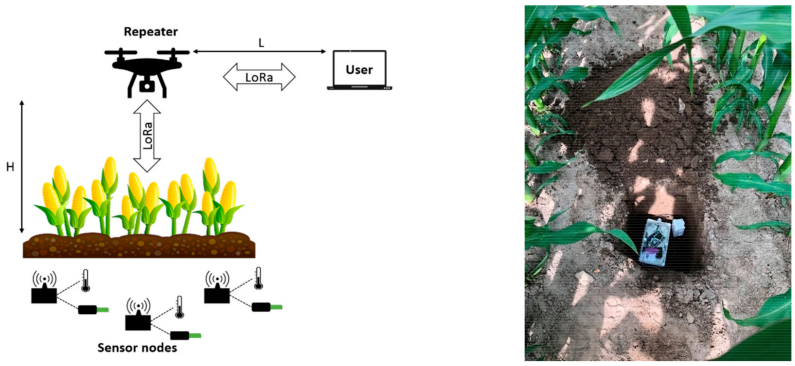

(a) (b)

Figure 1. *Cont.*

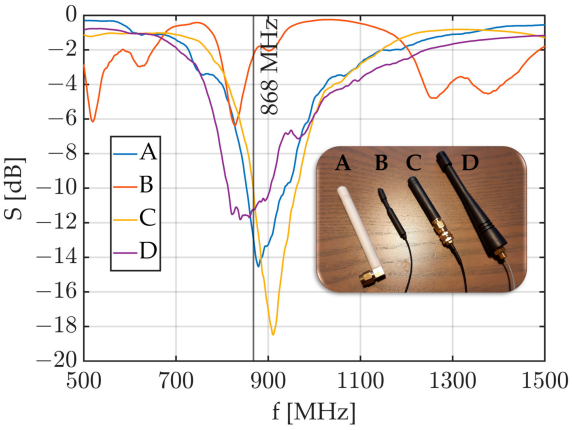

(**c**) (**d**)

Figure 1. (**a**) Schematic of the investigated communication setup. (**b**) Picture of a sensor node deployed in a maize field before closing the hole with soil. (**c**) Picture of the drone with attached component housing. (**d**) Characterization of different antennas in the range around the 868 MHz LoRa frequency with the scattering parameter S.

This paper is organized as follows. Section 2 presents the materials and methods. Section 3 contains the experimental results. The system design and the results are compared side-by-side with those of the relevant literature in Section 4 (discussion). Finally, the conclusions are presented in Section 5. Some of these results have recently been published as a conference contribution [26].

2. Materials and Methods

2.1. Materials

Three test sensor nodes, based on the ESP32 boards with a LoRa communication chip operating at 868 MHz, were used (WiFi LoRa 32 V2, Heltec Automation Technology, Chengdu, Sichuan, China). Figure 1d shows the characterization of the different antennas for the LoRa communication. The incorporated antenna from Heltec (Antenna "B") showed an unsatisfactory performance at the desired communication frequency of 868 MHz. For the further experiments, we used the antennas marked as "A" and "C", due to their superior performance around 868 MHz and small antenna size. The spreading factor (SF) was set to 10 to balance between the required power and time required for data transmission and the achievable range. The bandwidth (BW) was set to 125 kHz and the maximum available output power of 20 dBm was used. Those parameters where chosen which favored longer communication ranges over data rates and transmission power consumption.

A sensor node operates as follows to minimize power consumption. The ESP32 stays in deep sleep mode and wakes up at regular intervals for 5 s to obtain the data from the connected sensors and to listen for data requests from the drone. When it receives a request, it transmits the data stored since the last request and then goes back to sleep. The Heltec board has a rather high deep sleep current, of approximately 1 mA [27]. Therefore, the overall power consumption is determined by the deep sleep power, by the power required while waiting for a request from the drone and by the ratio between the time spent in deep sleep mode vs. time spent waiting for a request. It was decided to favor the transmission range over transmission power consumption because it was assumed that the amount of data collected and the frequency of drone readouts would be low. In the experiments, a wakeup interval of 5 s was chosen to acquire more data about the transmission quality. This interval would need to be increased when operating the system for longer timespans.

Each sensor node is powered by a 3.6 V lithium thionyl chloride (Li/SOCL2) battery (SL-2780, Tadiran Batteries, Kiryat Ekron, Israel), due to the high energy capacity of 19 Ah

and long lifetime (up to 10 years). In the experiments, a capacitive moisture and temperature sensor (Adafruit STEMMA Soil Sensor, Adafruit Industries LLC, New York, NY, USA) was connected. An IP68 enclosure protects the components from the ingress of water and dust.

The drone used to investigate the LoRa repeater function was the DJI Phantom 3 Advanced (DJI Technology, Shenzhen, China) (Figure 1c). DJI states a maximum flight time of approximately 23 min [28], but in the experiments, flight times of only approximately 15 min were achieved. A Heltec WiFi LoRa 32 V2 board with antenna "A" was attached to provide LoRa connectivity. It was powered by a 1100 mAh LiPo battery pack. The position of the drone was tracked by the onboard inertial measurement unit (IMU) and an additional NEO-6M GPS module connected to the Heltec board.

In order to acquire the data over LoRa and record it, a ground station consisting of a readout laptop and connected Arduino Uno with a Dragino LoRa Shield (SX1276 Shield-868, Dragino Technology, Shenzhen, China), was used. This module is also based on Semtech's SX1276 LoRa transceiver chip. The received LoRa packages were loaded onto the laptop over a USB serial interface and saved to a CSV file with a Python script. The post-collection analysis of the data was also conducted in Python.

The SX1276 chip provides information about the received signal strength indication (RSSI). This value can be used to evaluate the signal attenuation and was the main parameter used for interpreting the following experiments. Therefore, the RSSI of both LoRa communication paths (sensor to drone and drone to ground station) was acquired. The RSSI of the transmission between the sensor node and the drone was transmitted to the ground station, together with the GPS data from the NEO-6M module and the sensor data.

2.2. Methods

In order to analyze the different aspects of the usage of a drone as a repeater for LoRa communication, a series of experiments were conducted on the Experimental Farm Hohenschulen of Kiel University.

2.2.1. Investigation of Flight Height and Burial Depth Dependency

In the first series of experiments, the LoRa signal attenuation of the communication between the sensor node and drone was investigated, with the drone hovering at an increasing flight level H directly above the sensor node (Figure 2). There were two measurement series with sensor node depth D of 30 cm and 60 cm. The RSSI was recorded every 5 m until a 40 m height level was reached.

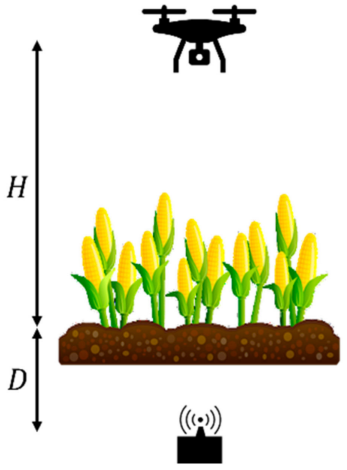

Figure 2. Schematic of the experimental setup used for investigating the dependency of the received signal strength at the drone on flight height H and burial depth D.

2.2.2. Demonstration of the Range Extension Capability

In a subsequent experiment, the communication range extension capability of the described system was investigated. Hence, the communication range L was compared for two different situations: direct sensor node to ground station communication (S1) and intermediate signal repetition at the drone (S2) (Figure 3).

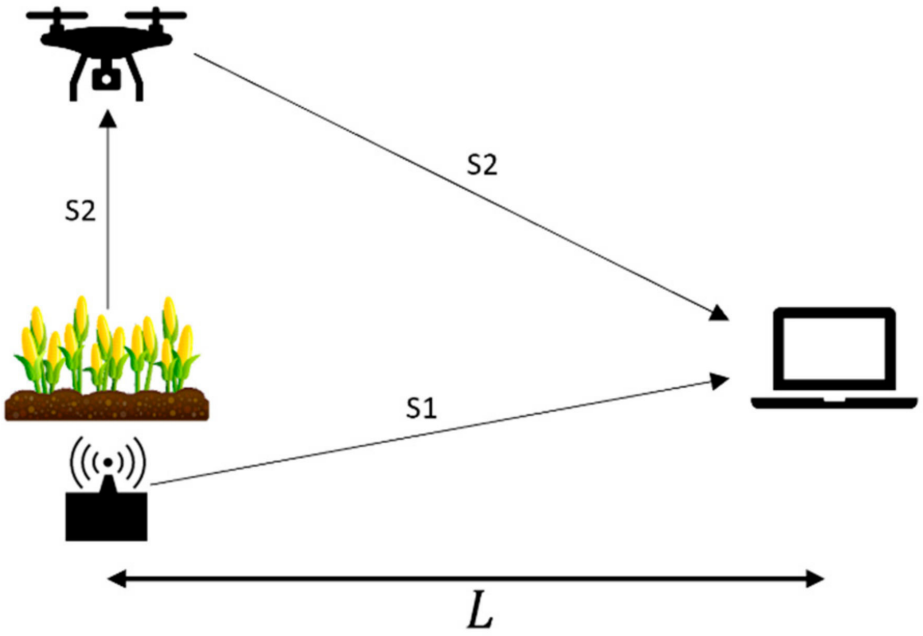

Figure 3. Schematic of the experimental setup used for demonstrating the extended range of the data collection system design. S1 shows the direct sensor node to ground station communication path and S2 the path with intermediate signal repetition at the drone.

Firstly, the system was configured so that the sensor node, buried at a depth of 30 cm, communicated directly with the ground station, bypassing the drone. The distance between the sensor node and ground station was increased while measuring the RSSI and the GPS position. Secondly, the experiment was conducted by using the drone as a repeater. The drone hovered 30 m above the sensor node and then, again, recorded the RSSI and GPS position every 50 m while the ground station was moved away.

2.2.3. Investigation of the Communication Range between Sensor Node and Drone

When applying the described system in a real-world scenario, a drone would not hover above each sensor node but would conduct the data collection from a certain distance. In order to maximize the area in which the sensor nodes can be deployed and read out, the range R for the communication between a sensor node and the drone has to be determined (Figure 4). For this purpose, a sensor node was buried at a depth of 30 cm and the communication was started with the drone hovering above the sensor node. The drone was then flown away at a constant height of 30 m while recording both its GPS position and the RSSI of the packages received at the drone from the sensor node.

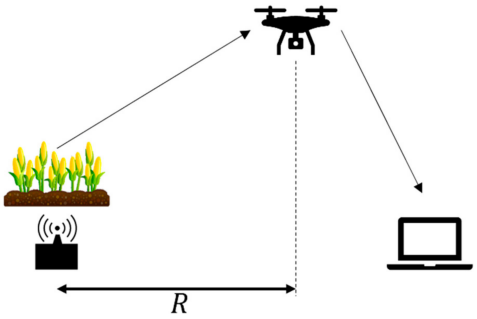

Figure 4. Schematic of the experimental setup used for the determination of the communication range between sensor node and drone.

2.2.4. Investigation of the Antenna Radiation Pattern

Commercially available antennas for LoRa communication are usually helical antennas. The radiation pattern has a toroidal shape and is symmetric around the z-axis of the antenna (Figure 5b). When using compact enclosures for the sensor nodes, the antennas must be oriented horizontally (Figure 5a). Consequently, the radiation pattern above the ground is not symmetric around the point where the drone is buried.

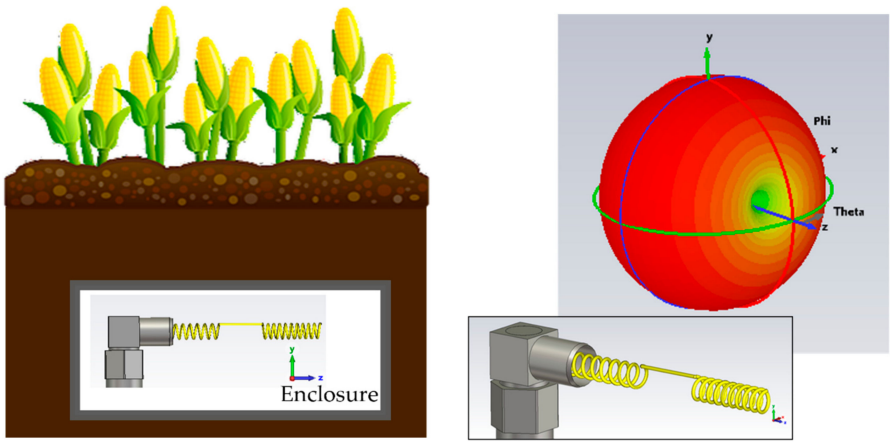

(**a**) (**b**)

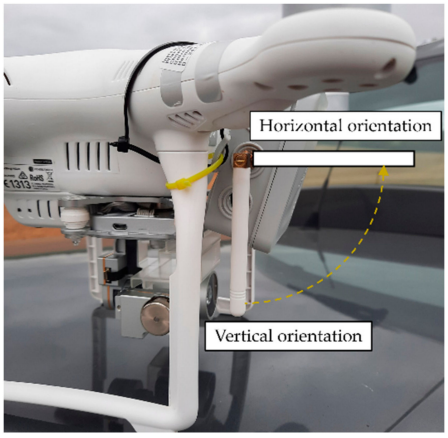

(**c**)

Figure 5. (**a**) Schematic of the antenna orientation (z axis) underground in the hardware enclosure. (**b**) Antenna radiation (**c**) Schematic of the antenna orientations investigated.

How this affects the RSSI of the data packages sent from the node to the drone was investigated. To achieve this, the sensor node was buried in a depth of 30 cm, with the antenna z-axis oriented in a known direction in the ground plane. Then, the drone was flown at a constant height of 30 m and with varying positions around the point at which the sensor node was buried. During flight, the sensor data was continuously read out and the GPS coordinates of the drone were acquired each time a package from the sensor node arrived. This enabled the correlation of the RSSI with the position of the drone. The antenna on the drone was oriented with the helix z-axis pointing downwards (Figure 5c) and, therefore, its radiation pattern is symmetric, minimizing distortions caused by the drone orientation.

2.2.5. Investigation of Reproducibility

The interpretation of the described experiments requires the reproducibility of the measurement data. In order to verify this, a sensor node was buried at a depth of 30 cm and three flights were carried out with the same path, directly passing above the sensor node at a constant height of 25 m (Figure 6). Each flight was started directly above the sensor node and then the drone was flown away to a defined distance (flight phase P1). Afterwards, it was steered back along the same path, passing over the sensor node, and then flown away again from the sensor node to a turning point (P2). From that point, the drone was flown back to the sensor node (P3). During flight, the data packages were continuously read out from the sensor node. Additionally, the chosen trajectory allows the analysis of how the RSSI changes when flying over the sensor node during data collection.

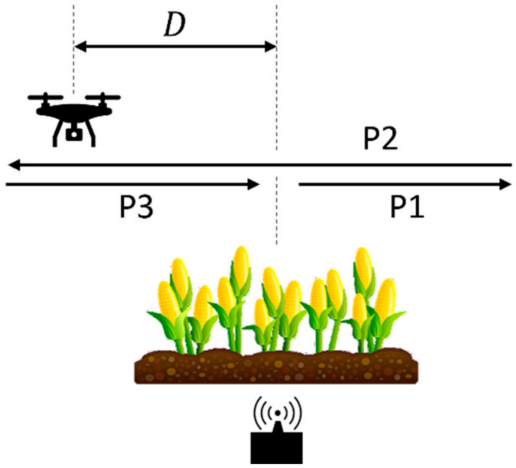

Figure 6. Schematic of the experimental setup and the different flight phases.

3. Results

3.1. Investigation of Flight Height and Burial Depth Dependency

The RSSI for a sensor node depth D of 30 cm was −63 dBm at a drone height of 5 m and −77 dBm at a height of 40 m, as shown in Figure 7. For a sensor node depth D of 60 cm the values were −64 dBm and −81 dBm, respectively, at drone heights of 5 m and 40 m. During the experiments, a loss of LoRa packages was observed at an RSSI of approximately −120 dBm. From this data, a repeater flight level of 130 m was estimated as possible for a sensor node buried at 60 cm depth. In a second set of experiments, it was found that the attenuation for flying the drone at a constant height to different distances L was in a similar range, with ~0.3 dB/m. This experiment was conducted on 23 November 2020.

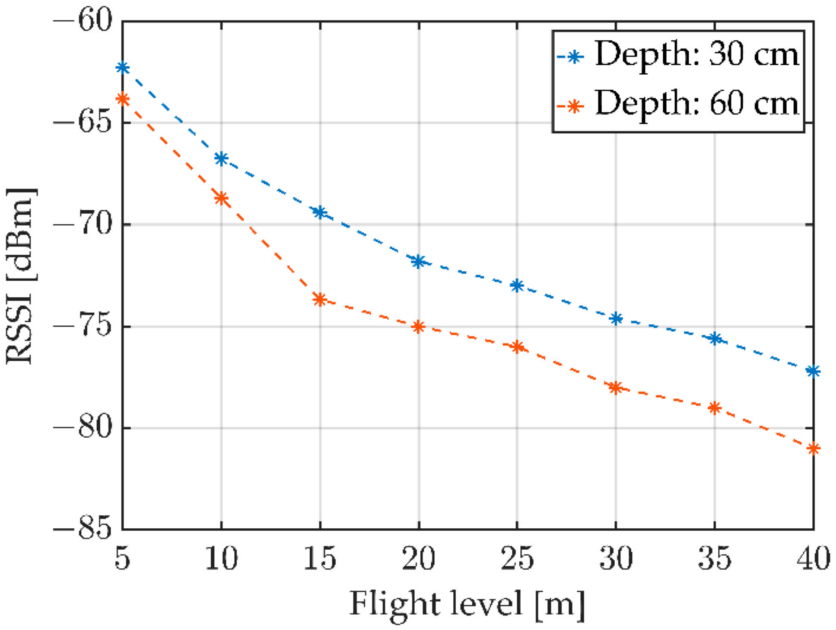

Figure 7. Comparison of the relationship between flight level and RSSI for the two sensor node depths of 30 cm and 60 cm.

3.2. Demonstration of the Range Extension Capability

Figure 8a shows a satellite image of the paths away from the sensor node for both parts of the experiment. The positions at which the last packages with sensor data were received are marked. The graph depicting the RSSI over distance (Figure 8b) shows that the LoRa packages were received up to L = 316 m (blue) for the case without using a drone. When using the drone to receive and transmit the data, the last package was received at a distance of L = 1000 m (orange). Thus, the communication range is enhanced by at least three times with the drone as a repeater. The height profile of the path between the sensor node and ground station (Figure 8c) particularly shows the advantage of the system. It can be seen that, for direct communication between node and ground station, the signal is lost after crossing the top of a hill, as the line of sight (LoS) is lost. By using the drone, a LoS can be ensured even in landscape with hills and other obstacles that might obstruct the signal. This experiment was conducted on 6 August 2021.

3.3. Investigation of the Communication Range between Sensor Node and Drone

The RSSI measurement results of the experiment can be seen in Figure 9a. The RSSI decreases with the increasing distance until the last data package is received at a distance of R = 550 m. Consequently, the drone can be used as a data collector for sensor nodes within a R_{max} = 550 m range.

From this data, it is possible to estimate the maximum area A_{max} on which the deployed sensor nodes can be read (Figure 9b). Assuming an average flying velocity of 18 km/h and a flight time of 15 min, a maximum flight distance of the drone S_{max} = 4500 m can be calculated. This allows for the determination of the length L, considering the given flightpath with minimal overlap (Figure 9b):

$$L = \frac{1}{2}(S_{max} - 4R_{max}) = 1150 \text{ m}. \quad (1)$$

Following this, the maximum area

$$A_{max} = 4R_{max}L + (4 + \pi)R_{max}^2 = 4.69 \text{ km}^2 \quad (2)$$

is calculated. Thus, utilizing a drone for sensor readout enables an area of approximately 470 hectares to be scanned within only 15 min. The data can be transmitted online to the user within a certain range (in this setup approximately 1 km) or by storage and the subsequent transmission of the data packages upon return to the base. This experiment was conducted on the 31 May 2022.

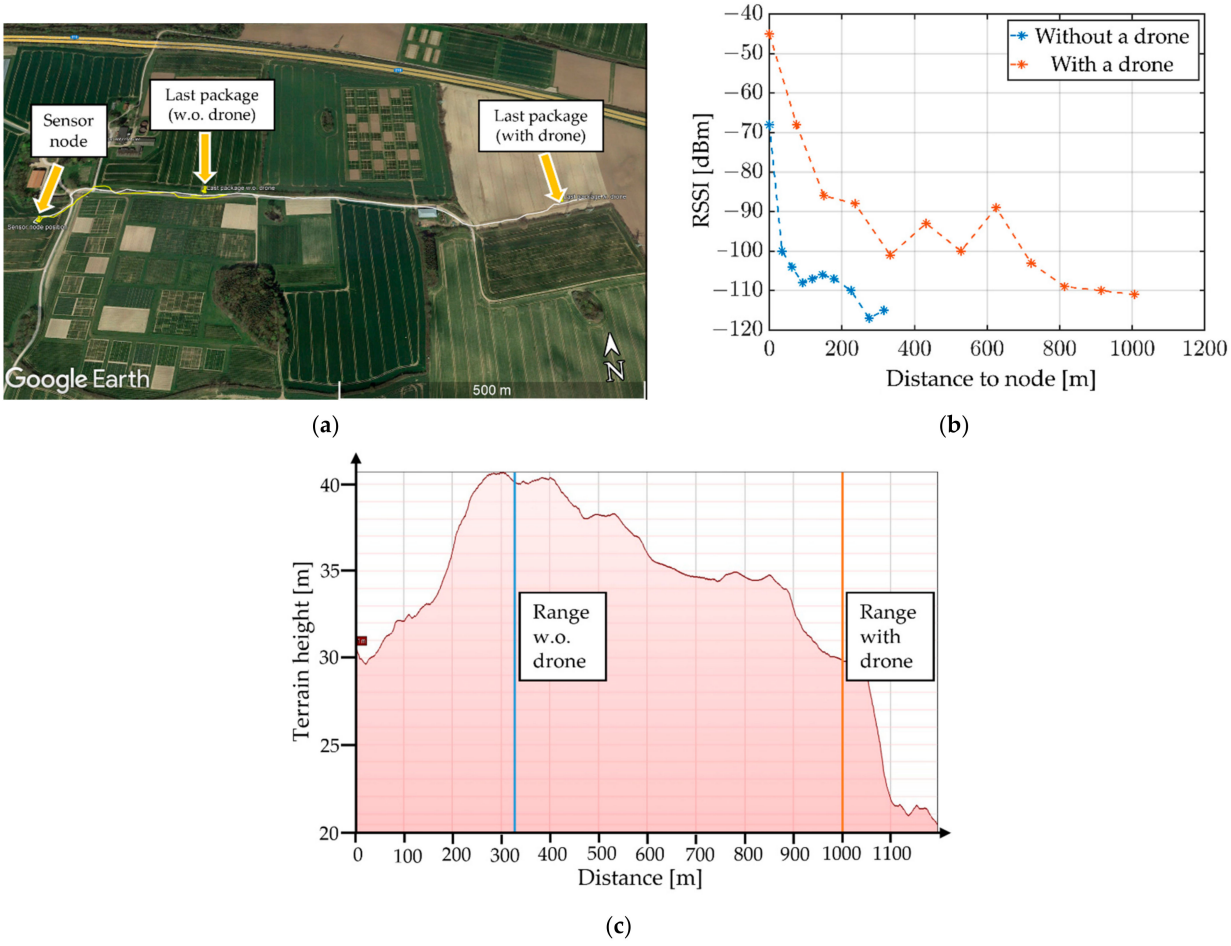

Figure 8. (**a**) Satellite view of the travelled path away from the sensor node (Map data: Google, Landsat/Copernicus) (**b**) Comparison of the RSSI of the packages received by the ground station with and without a drone as repeater. Sensor node depth is 30 cm. Drone is hovered 30 m above the sensor node as a repeater. (**c**) Height profile of the traveled path (Map data: Google, Landsat/Copernicus).

3.4. Investigation of the Antenna Radiation Pattern

The results of this experiment are visualized as point clouds (Figure 10). Each colored dot corresponds to the position of the drone when it received a package with the given RSSI. Figure 10a shows the point cloud for the vertical antenna orientation. The RSSI of the packages is higher at the perpendicular point to the antenna orientation than the inline point. This supports the hypothesis that the antenna orientation of the sensor node influences the RSSI of the transmitted packages. This fact can be important when optimizing flight paths for data collection, as the RSSI of data transmission not only depends on the distance between the sensor node and drone, but also on the sensor node orientation.

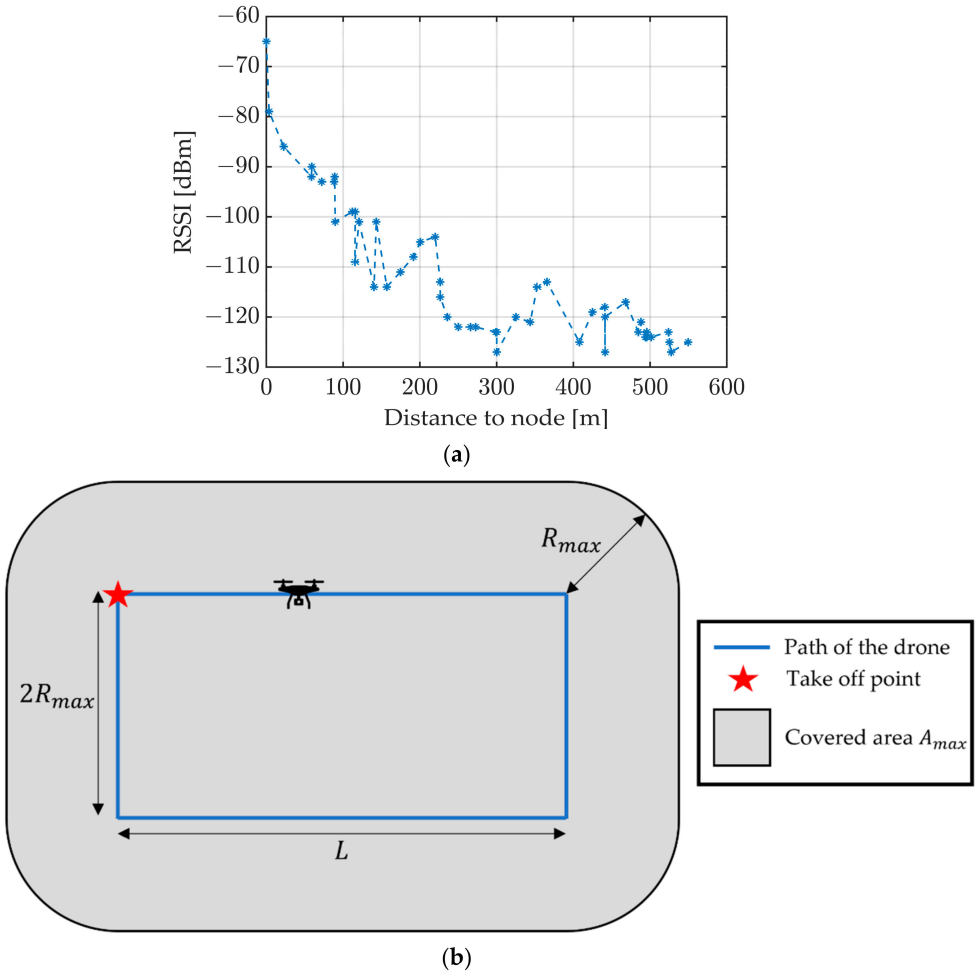

Figure 9. (**a**) Reduction in the RSSI with the increasing distance between the sensor node and drone. The sensor node depth was 30 cm. The drone had a constant flight height of 30 m. (**b**) Schematic of the assumed flight configuration for calculating the maximum covered area A_{max} = 470 ha.

In addition, the antenna orientation on the drone was changed from a vertical to a horizontal orientation (Figure 10b). This creates an additional dependency of the RSSI on the yaw angle of the drone, as the symmetry of the radiation pattern of the drone's antenna is lost. Therefore, the RSSI is less predictable; therefore, for practical applications, a vertical orientation of the antenna is to be preferred over a horizontal orientation. This experiment was conducted on 7 July 2022.

3.5. Investigation of Reproducibility

Firstly, the change in the RSSI over the pathway of a single flight was evaluated (see schematic in Figure 6). When flying away in phase P1, the RSSI decreased with distance D from the sensor node and increased again when turning around to fly phase P2 (Figure 11). After passing over the sensor node, the RSSI decreased, then in P3, it increased again until arriving back over the sensor node. The main observation is that the RSSI is lower when flying away from the sensor node than when flying towards it. It is believed that the reason for this is probably due to the radiation pattern of the antenna. For this experiment, the antenna was mounted with the z-axis facing downwards; thus, the radiation pattern (Figure 5b) is symmetric around the yaw axis of the drone, but not around the pitch axis. When flying towards the sensor node, the node lies closer to the xy-plane of the antenna

radiation pattern, where the maximum energy of the incoming signal is received by the drone's antenna. When flying away, the signal from the sensor node comes from an angle, where less energy of the incoming signal is converted from electromagnetic waves to an electric signal by the antenna, therefore the RSSI is lower.

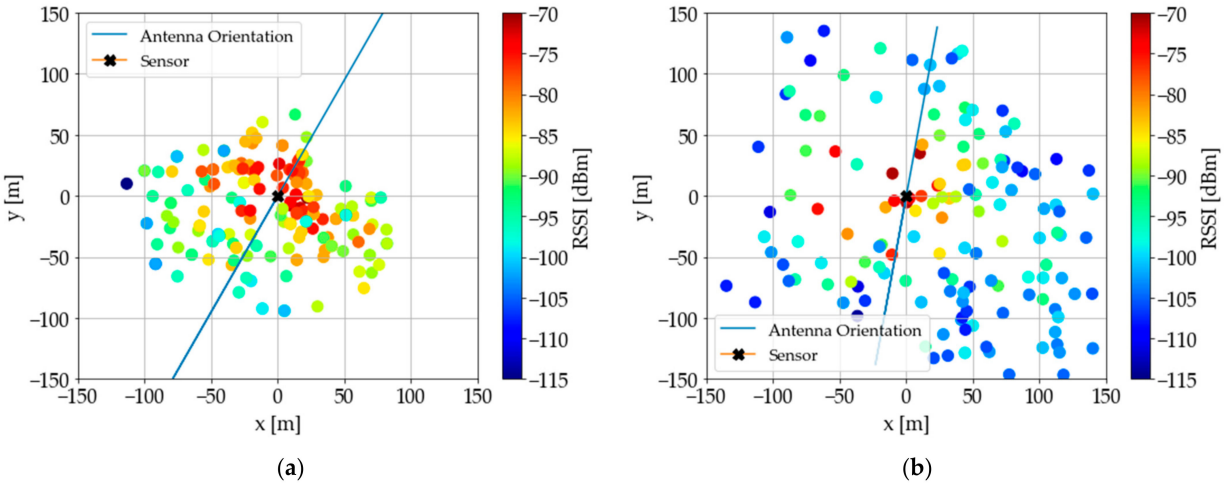

Figure 10. (**a**) Visualization of the experimental results for vertical antenna orientation on the drone as a point cloud. Each point corresponds to the position relative to the sensor node that a package was received and is colored to show the RSSI value of the transmission. Additionally, a line is placed along the orientation of the antenna of the sensor node. Sensor node depth was 30 cm. Drone had a constant flight height of 30 m. (**b**) Experimental results for horizontal antenna orientation on the drone.

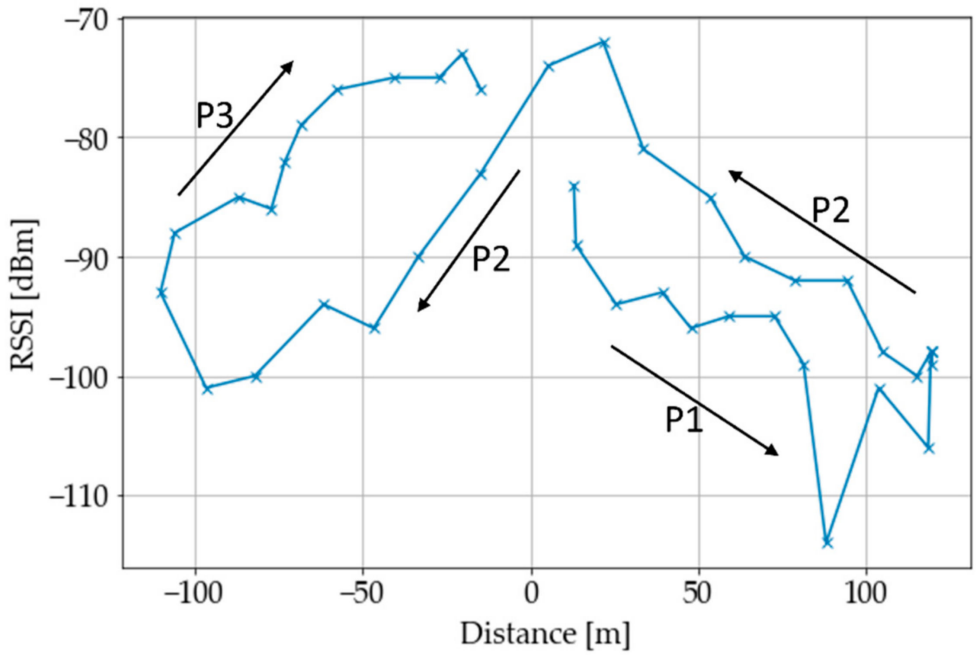

Figure 11. RSSI over distance D diagram of the third overflight to explain the behavior.

Secondly, the change in the RSSI over distance was compared between the three flights. During P1, the RSSI values differ, at a maximum of 10 dB for similar distances from the sensor node, and the qualitative development of the RSSI is comparable (Figure 12a). The

same is true for the second flight phase (Figure 12b), where the maximum difference is also 10 dBm, but for most distances the difference is smaller, at approximately 5 dB. For the third flight phase, the differences are mostly 4 dB, and when close to the sensor node, the difference goes up to approximately 10 dB (Figure 12c).

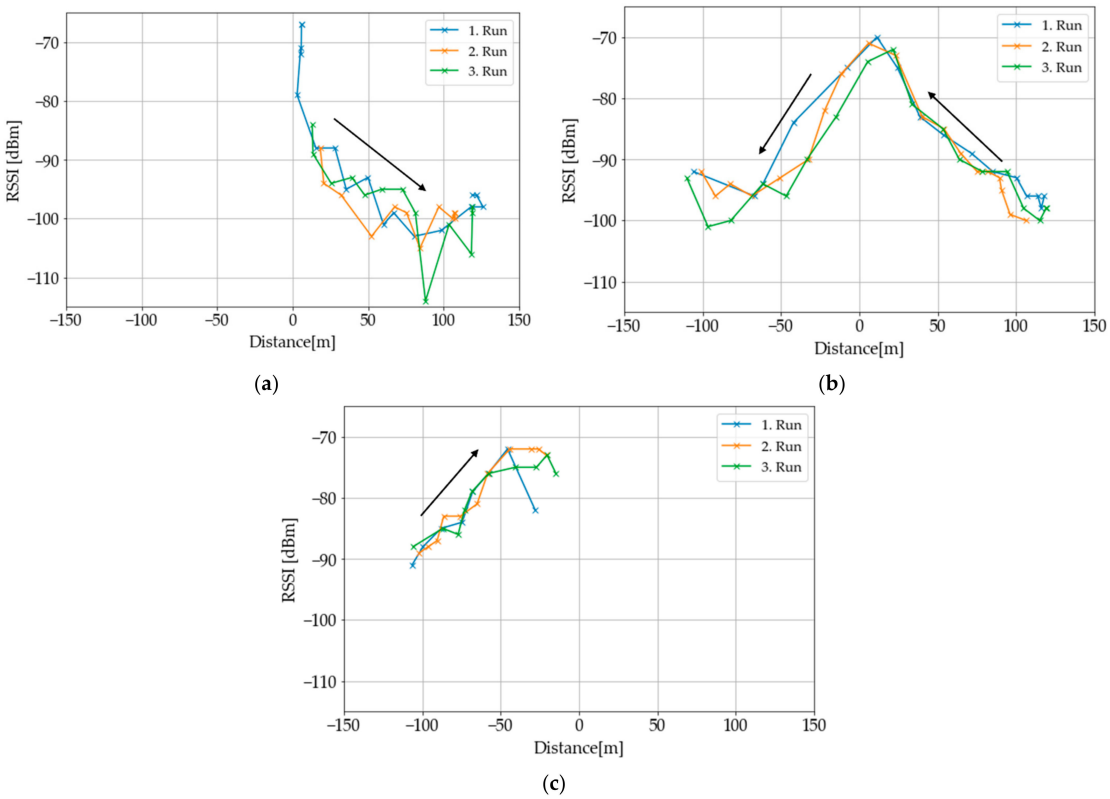

Figure 12. RSSI over distance diagram of the three flights, divided into the different flight phases for better clarity. The arrows show the direction of time evolution. Sensor node depth is 30 cm. Drone has a constant flight height of 25 m. (**a**) Phase 1. (**b**) Phase 2. (**c**) Phase 3.

The differences can be caused by errors in the reproduction of the desired flight path. These errors are most significant close to the sensor node because, here, small deviations in the flight path can lead to comparatively high deviations in the RSSI value. Additionally, the GPS positioning is also only accurate to a few meters, particularly the NEO6M GPS module as it only uses between six and eight satellites. The RSSI also depends on the pitch angle of the drone, as described before. The pitch angle also determines the speed of the drone. Therefore, speed differences between the flights can cause differences in the RSSI measurements. The large RSSI differences at the turning points of the drone are likely to be explained by this, because the speed and orientation changes at these points are difficult to reproduce between different flights. This experiment was conducted on the 29 August 2022.

4. Discussion

In this section, the system setup, methods and results are compared to the work of Cariou et al. [24] and Hossain et al. [25], because they share the same approach of collecting data from underground sensor nodes by using an UAV and the LoRa transmission technology.

The system setup of Cariou et al. consisted of a sensor node that was designed to be buried in the ground for several months. It awakened regularly from the sleep mode to transmit data from a soil moisture sensor, on request, to a collector node attached to a drone

via LoRa. This transmission used an SF of 7, a BW of 125 kHz and a transmission power (TxP) of 14 dBm. The collector node saved the data frames on an SD card and transmitted them over ZigBee to a network gateway when in close proximity.

The setup of Hossain et al. used a sensor node consisting of a Raspberry Pi for control, an RFM95 for LoRa connectivity and a soil moisture sensor. The sensor node was powered from above ground by a 12 V car battery and was not optimized for low power operation. Data packages were sent continuously to a LoRaWAN gateway attached to the drone, configured with SF 7, BW 125 kHz and a TxP of 20 dBm. The gateway also stored the data until the drone landed.

The SF, BW, and TxP for the LoRa transmissions of both groups were configured for higher data rates and lower transmission ranges between sensor node and drone. SF 10, BW 125 kHz, and TxP 20 dBm were used, which has to be considered when comparing the RSSI values and achieved transmission ranges. Another difference was the way the data from the drone was further processed after being received. Both Cariou et al. and Hossain et al. used an approach in which the data was collected and was only accessible to the user at the end of the flight. The data packages were transmitted online to the user with LoRa. This allowed for the diagnoses of problems during flight and access the data without delay. However, this also reduced the data rate further as the drone LoRa module could not collect new data packages from other nodes while retransmitting old packages to the ground station. Another approach was the direct upload of the data to the cloud via a 4G internet connection, as demonstrated in [17,29]. This obviously requires the local availability of a 4G connection.

In their experiments, Cariou et al. first measured the RSSI in a range of distances (0 to 150 m) from the UAV to the buried sensor node (15 cm deep) and for heights of 20/40/60 m. Their results are comparable to the results in Sections 3.1 and 3.3, which considered a 30 m flight height and 30 cm node depth. Their data showed that for high enough lateral distances, the RSSI is higher for higher flight heights. Secondly, they conducted an overflight experiment over the buried sensor node at different UAV speeds to show that the system was able to collect 100 packages from the node, independent of the speed. Their results showed RSSI measurements that are comparable to the results in Section 3.5, but the authors did not further investigate or explain this behavior. The authors further optimized the path for the data collection of 25 buried sensor nodes.

Hossain et al. measured the RSSI with a receiver gateway attached to a wooden pole with increasing height (0.3 to 2 m) and increasing lateral distance (0 to 5 m) relative to the sensor node (30 cm node depth), both for cross- and co-polarization between the sensor node and gateway antenna. The results were also compared with numerical simulations. Furthermore, the authors measured the packet loss for distances between the node and drone of up to 82 m, again comparing cross- and co-polarization. Additionally, they conducted trajectory flights at four heights, from 0.91 m to 3.66 m around the sensor node, covering a rectangle spanning -24 to 24 m and -27.4 m to 24 m. During flight, they again measured the RSSI for cross- and co-polarization. This experiment, although methodically similar to Section 2.2.4, considered a smaller lateral range scale and smaller flight heights. From the results, the authors concluded that the RSSI was largely independent of the polarization. The RSSI measurements are mostly complementary to the work of Cariou et al. [24] and the work described here as they focused on a scale closer to the buried sensor node.

Overall, this work shows similarities to both these other works when the methods and the results are considered. A common point of interest is the RSSI distribution around the sensor node, as described before, but different length scales were investigated. Furthermore, an attempt was made to estimate the maximum coverable area for the system setup. A particular new emphasis of this work is the impact of the orientation of the antenna at the sensor node and at the drone. Additionally, experiments on using a LoRa link from drone to ground station are presented.

Comparing the chosen system setups and methods, it can be observed that there are different assumptions about the sensor node density and the overall amount of data that needs to be collected. Cariou et al. and Hossain et al. considered smaller length scales in their experiments and configured the LoRa communication more for higher data rates than for communication distances. This is suitable for higher sensor node densities or if large amounts of data need to be transmitted at each connection. The system described here was designed more towards covering a greater area with lower sensor node density and lower amounts of data for each transmission.

5. Conclusions

In conclusion, a setup for communication with an underground network of LoRa sensor nodes has been demonstrated using a drone to collect the data. A much larger area can be covered than previously, without the need for the installation of additional ground-based hardware. The maximum communication ranges between an underground sensor node and drone and the dependency of the received signal strength on the flight height and burial depth for the setup was experimentally determined. The evaluation of the antenna orientation of the sensor node and the overflight experiment hinted at other possibilities for drone flight path optimization. In addition, the reproducibility of the RSSI measurements for different distances between the sensor node and drone was also demonstrated.

The long-term goal is a fully autonomous data collecting system for several sensor nodes based on a drone. The sensor nodes were operated in the soil and demonstrated successful connection for up to 49 days. Currently, sensors for physical and chemical soil parameters are integrated into the sensor nodes for the relevant data collection. For this purpose, a microfluidic unit for the extraction of soil water has been developed [30], as well as a compact sensor chip based on organic optoelectronic devices for nitrite and nitrate determination [31]. To enable the data collection for a larger number of sensor nodes, a more sophisticated communication protocol must be implemented to avoid package collisions. Additionally, adapting the spreading factor and the bandwidth according to the respective distances and sensor node densities is important to maximize the area coverage and collection performance of the system. This can be further improved by optimizing the drone path between sensor nodes. Regarding the system setup, it is still to be determined whether LoRa is the optimal way to transmit the data from the drone to the ground station. Possibly, a transmission directly over LTE to a cloud is advantageous to point-to-point LoRa, particularly for situations where high data rates are required. Another important aspect is the optimization of the sensor node antenna to the ground-to-air transmission situation.

Author Contributions: Conceptualization, L.H., I.T., F.D. and M.G.; methodology, L.H., I.T., F.D. and M.G.; software, L.H.; validation, L.H. and I.T.; formal analysis, L.H., I.T. and M.G.; investigation, L.H. and I.T.; resources, M.G.; data curation, L.H. and I.T.; writing—original draft preparation, L.H., I.T. and M.G.; writing—review and editing, L.H., I.T., F.D. and M.G.; visualization, L.H., I.T. and F.D.; supervision, I.T. and M.G.; project administration, M.G.; funding acquisition, M.G. All authors have read and agreed to the published version of the manuscript.

Funding: This project received funding from the European Regional Development Fund (EFRE) by the European Union (OPTOCHIP, LPW-E/1.2.2/1303).

Data Availability Statement: Data underlying the results presented in this paper are not publicly available at this time but may be obtained from the authors upon reasonable request.

Acknowledgments: The authors thank the Institute of Crop Science and Plant Breeding for providing the drone and for farm access at the Experimental Farm Hohenschulen.

Conflicts of Interest: The authors declare no conflict of interest.

References

1. Robert, P.C. Precision agriculture: A challenge for crop nutrition management. *Plant Soil* **2002**, *247*, 143–149. [CrossRef]
2. Shiva, V. *The Violence of the Green Revolution: Third World Agriculture, Ecology and Politics*; Zed Books: London, UK, 1991; ISBN 9780862329655.
3. Hillel, D.; Braimoh, A.K.; Vlek, P.L.G. *Soil Degradation Under Irrigation*; Springer: Dordrecht, The Netherlands, 2008.
4. Bardhan, K.; York, L.M.; Hasanuzzaman, M.; Parekh, V.; Jena, S.; Pandya, M.N. Can smart nutrient applications optimize the plant's hidden half to improve drought resistance? *Physiol. Plant.* **2021**, *172*, 1007–1015. [CrossRef]
5. Forde, B.; Lorenzo, H. The nutritional control of root development. *Plant Soil* **2002**, *232*, 51–68. [CrossRef]
6. Gebbers, R.; Adamchuk, V.I. Precision agriculture and food security. *Science* **2010**, *327*, 828–831. [CrossRef] [PubMed]
7. Vuran, M.C.; Salam, A.; Wong, R.; Irmak, S. Internet of underground things: Sensing and communications on the field for precision agriculture. In Proceedings of the 2018 IEEE 4th World Forum on Internet of Things (WF-IoT), Singapore, 5–8 February 2018. [CrossRef]
8. Grunwald, A.; Schaarschmidt, M.; Westerkamp, C. LoRaWAN in a rural context: Use cases and opportunities for agricultural businesses. In Proceedings of the Mobile Communication-Technologies and Applications; 24. ITG-Symposium, Osnabrueck, Germany, 15–16 May 2019; pp. 1–6.
9. Salam, A.; Vuran, M.C.; Irmak, S. Di-Sense: In situ real-time permittivity estimation and soil moisture sensing using wireless underground communications. *Comput. Netw.* **2019**, *151*, 31–41. [CrossRef]
10. Wohwe Sambo, D.; Forster, A.; Yenke, B.O.; Sarr, I.; Gueye, B.; Dayang, P. Wireless Underground Sensor Networks Path Loss Model for Precision Agriculture (WUSN-PLM). *IEEE Sens. J.* **2020**, *20*, 5298–5313. [CrossRef]
11. Barbedo, J. A Review on the Use of Unmanned Aerial Vehicles and Imaging Sensors for Monitoring and Assessing Plant Stresses. *Drones* **2019**, *3*, 40. [CrossRef]
12. Barnetson, J.; Phinn, S.; Scarth, P. Estimating Plant Pasture Biomass and Quality from UAV Imaging across Queensland's Rangelands. *AgriEngineering* **2020**, *2*, 523–543. [CrossRef]
13. Bukowiecki, J.; Rose, T.; Kage, H. Sentinel-2 Data for Precision Agriculture?-A UAV-Based Assessment. *Sensors* **2021**, *21*, 2861. [CrossRef]
14. Fan, D.; Su, X.; Weng, B.; Wang, T.; Yang, F. Research Progress on Remote Sensing Classification Methods for Farmland Vegetation. *AgriEngineering* **2021**, *3*, 971–989. [CrossRef]
15. Quino, J.; Maja, J.M.; Robbins, J.; Fernandez, R.T.; Owen, J.S.; Chappell, M. RFID and Drones: The Next Generation of Plant Inventory. *AgriEngineering* **2021**, *3*, 168–181. [CrossRef]
16. Marturano, F.; Martellucci, L.; Chierici, A.; Malizia, A.; Di Giovanni, D.; d'Errico, F.; Gaudio, P.; Ciparisse, J.-F. Numerical Fluid Dynamics Simulation for Drones' Chemical Detection. *Drones* **2021**, *5*, 69. [CrossRef]
17. Behjati, M.; Mohd Noh, A.B.; Alobaidy, H.A.H.; Zulkifley, M.A.; Nordin, R.; Abdullah, N.F. LoRa Communications as an Enabler for Internet of Drones towards Large-Scale Livestock Monitoring in Rural Farms. *Sensors* **2021**, *21*, 5044. [CrossRef]
18. Park, S.; Yun, S.; Kim, H.; Kwon, R.; Ganser, J.; Anthony, S. Forestry Monitoring System Using LoRa and Drone. In Proceedings of the 8th International Conference on Web Intelligence, Mining and Semantics, Novi Sad, Serbia, 25–27 June 2018. [CrossRef]
19. Caruso, A.; Chessa, S.; Escolar, S.; Barba, J.; Lopez, J.C. Collection of Data With Drones in Precision Agriculture: Analytical Model and LoRa Case Study. *IEEE Internet Things J.* **2021**, *8*, 16692–16704. [CrossRef]
20. Zhang, Z.; Zhou, C.; Sheng, L.; Cao, S. Optimization Schemes for UAV Data Collection with LoRa 2.4 GHz Technology in Remote Areas without Infrastructure. *Drones* **2022**, *6*, 173. [CrossRef]
21. Pan, Q.; Wen, X.; Lu, Z.; Li, L.; Jing, W. Dynamic Speed Control of Unmanned Aerial Vehicles for Data Collection under Internet of Things. *Sensors* **2018**, *18*, 3951. [CrossRef] [PubMed]
22. Zorbas, D.; O'Flynn, B. Collision-Free Sensor Data Collection using LoRaWAN and Drones. In Proceedings of the 2018 Global Information Infrastructure and Networking Symposium (GIIS), Thessaloniki, Greece, 23–25 October 2018; IEEE: Piscataway, NJ, USA, 2018.
23. Castellanos, G.; Deruyck, M.; Martens, L.; Joseph, W. System Assessment of WUSN Using NB-IoT UAV-Aided Networks in Potato Crops. *IEEE Access* **2020**, *8*, 56823–56836. [CrossRef]
24. Cariou, C.; Moiroux-Arvis, L.; Pinet, F.; Chanet, J.-P. Data Collection from Buried Sensor Nodes by Means of an Unmanned Aerial Vehicle. *Sensors* **2022**, *22*, 5926. [CrossRef]
25. Hossain, F.F.; Messenger, R.; Captain, G.L.; Ekin, S.; Jacob, J.D.; Taghvaeian, S.; O'Hara, J.F. Soil Moisture Monitoring Through UAS-Assisted Internet of Things LoRaWAN Wireless Underground Sensors. *IEEE Access* **2022**, *10*, 102107–102118. [CrossRef]
26. Titov, I.; Holtorf, L.; Daschner, F.; Gerken, M. Drone as LoRa® Repeater for Readout of Low-power Sensor Nodes in Precision Agriculture. In Proceedings of the EASS 2022; 11th GMM-Symposium, Erfurt, Germany, 5–6 July 2022; pp. 1–3.
27. Heltec Automation Technology Co., Ltd. WiFi LoRa 32 (V2): LoRa Node Development Kit. Available online: https://resource.heltec.cn/download/Manual%20Old/WiFi%20Lora32Manual.pdf (accessed on 15 January 2023).
28. DJI Technology Co., Ltd. Phantom 3 Advanced: User Manual V1.8. Available online: https://dl.djicdn.com/downloads/phantom_3/en/Phantom_3_Advanced_User_Manual_en_v1.8_160719.pdf (accessed on 15 January 2023).
29. Almalki, F.A.; Soufiene, B.O.; Alsamhi, S.H.; Sakli, H. A Low-Cost Platform for Environmental Smart Farming Monitoring System Based on IoT and UAVs. *Sustainability* **2021**, *13*, 5908. [CrossRef]

30. Böckmann, S.; Titov, I.; Gerken, M. Extraction of Soil Solution into a Microfluidic Chip. *AgriEngineering* **2021**, *3*, 783–796. [CrossRef]
31. Titov, I.; Köpke, M.; Gerken, M. Monolithic Integrated OLED–OPD Unit for Point-of-Need Nitrate Sensing. In *Optical Sensors and Sensing Congress 2022 (AIS, LACSEA, Sensors, ES), Proceedings of the Optical Sensors and Sensing Congress 2022 (AIS, LACSEA, Sensors, ES), Vancouver, BC, Canada, 11 July 2022*; Optica Publishing Group, Ed.; Optica Publishing Group: Washington, DC, USA, 2022.

Chapter 5

Conclusion and Proposed Future Research

This chapter contains the conclusion of the PhD thesis summarizing the key findings of investigations with the monolithic integrated OLED-OPD chip and gives an outlook of possible future research activities to increase the system efficiency and to integrate the system into a monitoring sensor for chemical soil parameters.

5.1 Thesis Summary and Conclusions

In summary, this dissertation shows an extensive study of the system design, modeling, characterization and deployment of a miniaturized monolithic integrated optoelectronic sensor unit with 8 OLED and 8 OPD pixel pairs in the context of different applications. The work includes an estimation of the system efficiency utilizing ray tracing simulations in the COMSOL Multiphysics Software, investigating crucial boundary conditions for an efficient detection of an analyte. The proposed sensing unit contains OLED and OPD devices with an individual pixel size of $0.5\,\mathrm{mm} \times 0.5\,\mathrm{mm}$ fabricated on a $12.5\,\mathrm{mm} \times 12.5\,\mathrm{mm}$ glass substrate. All optoelectronic elements were thoroughly electrically and optically characterized after fabrication. This sensing platform was successfully applied in a biomedical application utilizing a blue-emitting FIrPic-OLED and a DMQA:DCV3T-OPD to detect a fluorescence signal of specific biomarkers. In environmental and agricultural applications, the OLED was changed to a TCTA:$Ir(mppy)_3$-OLED to detect nitrite and nitrate.

The deployment in the biomedical context was experimentally verified by

the detection of fluorescence-labeled capture ssDNA and the subsequent quenching of the fluorescence signal by adding a quencher-labeled complementary ssDNA in solution. The biomedical assay was provided by Altona Diagnostics GmbH as the project partner. In the second step fluorescence-labeled ssDNA was covalently coupled on a glass surface, which was intended to act as sample capture molecule. However, the fluorescence of surface-bound biomarkers with the OLED-OPD chip could not be detected, hence a detailed investigation of the limiting factors in the current system was performed based on further characterization experiments and ray tracing simulations. The simulation results show that the highest light loss factors are due the wide emission angle of the OLED (approximately 97.3%) (assumed a Lambertian emission pattern) and the spherical losses of the fluorescence emission of the biomarkers (approximately 97%). The highest experimental identified loss factor is the high light transmission rate of the fluorophores (approximately 97%). Furthermore it was shown that the fabrication of microfluidic structures with black (absorptive) PDMS is promising for stray light suppression. Nevertheless, the detection was demonstrated to be within reach and several improvements were proposed for future research. This optoelectronic sensor has the potential to enable compact and low-cost fluorescence POC devices for decentralized multiplex biomedical testing.

Additionally, this sensing platform was also deployed in environmental and agricultural applications to detect nitrite and nitrate. In this colorimetric approach, the popular Griess reaction was utilized to form a nitrite concentration dependent amount of azo dye, which absorbs light around 540 nm. The device was used in the reflectometry approach and shows a low limit of detection of $46\,\mu g\,L^{-1}$ ($1.0\,\mu mol\,L^{-1}$) and a linearity of 99%. To push the technology towards an optical microfluidic analysis system for in-situ chemical detection of nutrients in soil solution, a soil solution extraction unit was developed. Here, a porous aluminum oxide filter was applied in the inlet and a low-power peristaltic pump at the outlet of the microfluidic unit to create vacuum inside the chamber and extract soil water for further investigation. This device presents the missing link between the optoelectronic sensing unit and microfluidic analysis systems. Furthermore, an ESP32-based LoRa communication setup was developed in a student project under the supervision during this dissertation to create an underground sensor network and investigate the communication ranges. The development of the sensing platform, the microfluidic soil solution

extraction unit, and the communication hardware serves as the fundamental step towards the integration of all system elements to a compact soil parameter monitoring unit, which will gain a high value for resource-efficient and environmentally sustainable smart agriculture.

5.2 Proposed Improvements

The integration of organic optoelectronic devices is a powerful approach pushing the device sizes towards highly compact and low-power POC systems for biomedical applications, as well as for nutrients sensing in environmental and agricultural applications. The thermal evaporation technique enables a wide variety of geometrical shapes, sizes and the fabrication on rigid or flexible substrates with permanently aligned devices. Thus, this chip holds the potential for highly integrated multiplex sensing as well as the implementation of sensing redundancy. Taking this step towards an in-plane integrated OLED-OPD sensing platform enables also the potential for parallel mass fabrication, increasing the commercial viability. In particular, the fabrication on flexible substrates is highly promising for roll-to-roll fabrication [35].
To improve the sensing performance of the decentralized EHV testing unit, tuning the OLED stacks is a promising next step towards a stable blue emitting FIrPic-OLED for more efficient excitation of the dye-labeled biomarkers. Adopting a double emission layer to form a bi-layer device with FIrPic:CBP and FIrPic:TPBi may increase the illumination of the spot [69]. Additionally, reducing the distance between the OLED and the OPD from 0.9 mm to 0.1 mm (assuming that the biomarker spot is immobilized above the OPD) would increase the OLED excitation irradiance on the fluorescence spot by a factor of approximately 1.3. Furthermore, it is worth to change the geometry of the sensing unit such that the OPD is placed with minimum distance to the fluorescence spots. For this purpose, the OLED-OPD unit should be fabricated on a PET foil as proposed in the second publication. Considering a substrate thickness of 200 µm instead of the initially applied 1 mm glass substrate, the simulated efficiency of fluorescence detection could be improved from $\eta_{Det} = 1.8\%$ to $\eta'_{Det} = 22.8\%$. However, this step deserves a careful consideration as reducing the substrate thickness will lead to a decrease of OLED irradiation on the fluorescence spot. An optimum ratio between the substrate thickness and the OLED-OPD distance has to be evaluated.
For quantification of nitrite concentrations with the modified organic mate-

rials of the OLED-OPD chip further improvements shall be investigated to improve the current LOD. As a next step, tuning of the organic stacks may yield an improvement of system performance. The analyte consumption may be reduced by integrating the organic chip with a microfluidic unit. For PON applications it is crucial to integrate the device with a portable and battery-powered system.

The soil solution extraction unit and the proposed LoRa communication sensor unit constitute the missing link between optical microfluidic analysis systems and in-situ chemical monitoring of nutrients in soil solution. This work may act as the next step towards an automated and continuous in situ soil nutrient detection unit for smart agriculture. Nowadays bulky automated soil solution extraction units utilized for laboratory sample extraction shall be replaced with automated extraction units for continuous nutrients monitoring in soil or aquaculture environments. This technology may serve as a fundamental step towards a sensing platform in agriculture for soil nutrients monitoring, which is a promising tool to face the issues emerging from the ever growing population. Ensuring sustenance for all while making agriculture resource-efficient and environmentally sustainable is the most desirable goal to be reached within the next decades and requires new technological solutions.

Bibliography

[1] U.N., "World population prospects: Highlights 2019," *Department of Economic and Social Affairs, Population Division*, 2019.

[2] M. Elumalai, *DNA biosensor based on optical detection for environmental control*. PhD thesis, Universidade de Vigo, 2021.

[3] I. Titov, N. Rutschke, F. A. Kraft, M. Köpke, E. Nebling, and M. Gerken, "Detection of fluorescence-labeled DNA with in-plane organic optoelectronic devices," *Biomedical Optics Express*, vol. 13, p. 6300, dec 2022.

[4] C. J. Thieulent, E. S. Hue, C. I. Fortier, P. Dallemagne, S. Zientara, H. Munier-Lehmann, A. Hans, G. D. Fortier, P. H. Pitel, P. O. Vidalain, and S. L. Pronost, "Screening and evaluation of antiviral compounds against Equid alpha-herpesviruses using an impedance-based cellular assay," *Virology*, vol. 526, no. October 2018, pp. 105–116, 2019.

[5] R. F. Follett and J. L. Hatfield, "Nitrogen in the environment: sources, problems, and management.," *The Scientific World Journal*, vol. 1 Suppl 2, pp. 920–926, 2001.

[6] M. Parvizishad, A. Dalvand, A. H. Mahvi, and F. Goodarzi, "A Review of Adverse Effects and Benefits of Nitrate and Nitrite in Drinking Water and Food on Human Health," *Health Scope*, vol. 6, no. 3, 2017.

[7] Z. Xu, X. Wang, R. J. Weber, R. Kumar, and L. Dong, "Nutrient sensing using chip scale electrophoresis and In Situ soil solution extraction," *IEEE Sensors Journal*, vol. 17, no. 14, pp. 4330–4339, 2017.

[8] G. Kokkinis, G. Kriechhammer, D. Scheidl, B. Wilfling, and M. Smolka, "Towards the Commercialization of a Lab-on-a-Chip Device for Soil Nutrient Measurement," *Information and Communication Technologies in Modern Agricultural Development*, pp. 118–130, 2019.

[9] I. Titov, M. Köpke, and M. Gerken, "Monolithic Integrated OLED-OPD Unit for Point-of-Need Nitrate Sensing," *Optical Sensors and Sensing Congress 2022*, vol. 1, p. EW1G.1, 2022.

[10] I. Titov, M. Köpke, and M. Gerken, "Monolithic Integrated OLED-OPD Unit for Point-of-Need Nitrite Sensing," *Sensors*, vol. 22, p. 910, jan 2022.

[11] D. Dey and T. Goswami, "Optical Biosensors: A Revolution Towards Quantum Nanoscale Electronics Device Fabrication," *Journal of Biomedicine and Biotechnology*, vol. 2011, pp. 1–7, 2011.

[12] D. Soukarié, V. Ecochard, and L. Salomé, "DNA-based nanobiosensors for monitoring of water quality," *International Journal of Hygiene and Environmental Health*, vol. 226, p. 113485, may 2020.

[13] C. Chen and J. Wang, "Optical biosensors: an exhaustive and comprehensive review," *The Analyst*, vol. 145, no. 5, pp. 1605–1628, 2020.

[14] S. B. VanEngelenburg and A. E. Palmer, "Fluorescent biosensors of protein function," *Current Opinion in Chemical Biology*, vol. 12, pp. 60–65, feb 2008.

[15] E. P. Kartalov, J. F. Zhong, A. Scherer, S. R. Quake, C. R. Taylor, and W. French Anderson, "High-throughput multi-antigen microfluidic fluorescence immunoassays," *BioTechniques*, vol. 40, pp. 85–90, jan 2006.

[16] G. Orellana, "Luminescent optical sensors," *Analytical and Bioanalytical Chemistry*, vol. 379, pp. 344–346, jun 2004.

[17] J. R. Lakowicz, *Principles of Fluorescence Spectroscopy*. Boston, MA: Springer US, 2006.

[18] T. J. Lambert, "FPbase: a community-editable fluorescent protein database," *Nature Methods*, vol. 16, pp. 277–278, apr 2019.

[19] C. Lian, K. Yoshida, C. Nogues, and I. D. W. Samuel, "Organic Light Emitting Diode Based Fluorescence Sensing System for DNA Detection," *Advanced Materials Technologies*, vol. 7, p. 2100806, may 2022.

[20] V. Nock, *Control and Measurement of Oxygen in Microfluidic Bioreactors*. PhD thesis, University of Canterbury, 2009.

[21] C. McDonagh, P. Bowe, K. Mongey, and B. D. MacCraith, "Characterisation of porosity and sensor response times of sol-gel-derived thin films for oxygen sensor applications," *Journal of Non-Crystalline Solids*, vol. 306, no. 2, pp. 138–148, 2002.

[22] J. Estella, D. Wencel, J. P. Moore, M. Sourdaine, and C. McDonagh, "Fabrication and performance evaluation of highly sensitive hybrid sol-gel-derived oxygen sensor films based on a fluorinated precursor," *Analytica Chimica Acta*, vol. 666, no. 1-2, pp. 83–90, 2010.

[23] Y. Wang, J. Y. Shyy, and S. Chien, "Fluorescence proteins, live-cell imaging, and mechanobiology: Seeing is believing," *Annual Review of Biomedical Engineering*, vol. 10, no. August 2014, pp. 1–38, 2008.

[24] B. Valeur, *Molecular Fluorescence*. Wiley, dec 2001.

[25] D. F. Swinehart, "The Beer-Lambert Law," *Journal of Chemical Education*, vol. 39, p. 333, jul 1962.

[26] U. Obahiagbon, *Modeling, Design, Fabrication, and Characterization of a Highly Sensitive Fluorescence-based Detection Platform for Point-of-Care Applications*. PhD thesis, Arizona State University, 2018.

[27] N. Adarsh, M. Shanmugasundaram, and D. Ramaiah, "Efficient Reaction Based Colorimetric Probe for Sensitive Detection, Quantification, and On-Site Analysis of Nitrite Ions in Natural Water Resources," *Analytical Chemistry*, vol. 85, pp. 10008–10012, nov 2013.

[28] Y.-l. Liu, N. Kang, X.-b. Ke, D. Wang, L. Ren, and H.-j. Wang, "A fluorescent nanoprobe based on metal-enhanced fluorescence combined with Förster resonance energy transfer for the trace detection of nitrite ions," *RSC Advances*, vol. 6, no. 33, pp. 27395–27403, 2016.

[29] A. Antczak-Chrobot, P. Bąk, and M. Wojtczak, "The use of ionic chromatography in determining the contamination of sugar by-products by nitrite and nitrate," *Food Chemistry*, vol. 240, pp. 648–654, feb 2018.

[30] J. F. Tan, A. Anastasi, and S. Chandra, "Electrochemical detection of nitrate, nitrite and ammonium for on-site water quality monitoring," *Current Opinion in Electrochemistry*, vol. 32, p. 100926, apr 2022.

[31] G. Li, Y. Xia, Y. Tian, Y. Wu, J. Liu, Q. He, and D. Chen, "Review: Recent Developments on Graphene-Based Electrochemical Sensors toward Nitrite," *Journal of The Electrochemical Society*, vol. 166, pp. B881–B895, jul 2019.

[32] J. Dutt and J. Davis, "Current strategies in nitrite detection and their application to field analysisThe opinions expressed in the following article are entirely those of the authors and do not necessarily represent the views of The Royal Society of Chemistry, the Editor or th," *Journal of Environmental Monitoring*, vol. 4, pp. 465–471, may 2002.

[33] P. H. Petsul, G. M. Greenway, and S. J. Haswell, "The development of an on-chip micro-flow injection analysis of nitrate with a cadmium reductor," *Analytica Chimica Acta*, vol. 428, no. 2, pp. 155–161, 2001.

[34] C. W. Tang and S. A. VanSlyke, "Organic electroluminescent diodes," *Applied Physics Letters*, vol. 51, pp. 913–915, sep 1987.

[35] Y. Murat, K. Petersons, D. Lanka, L. Lindvold, L. Yde, J. Stensborg, and M. Gerken, "All solution-processed ITO free flexible organic light-emitting diodes," *Materials Advances*, vol. 1, no. 8, pp. 2755–2762, 2020.

[36] A. K. Bansal, S. Hou, O. Kulyk, E. M. Bowman, and I. D. Samuel, "Wearable Organic Optoelectronic Sensors for Medicine," *Advanced Materials*, vol. 27, no. 46, pp. 7638–7644, 2015.

[37] T. Yokota, P. Zalar, M. Kaltenbrunner, H. Jinno, N. Matsuhisa, H. Kitanosako, Y. Tachibana, W. Yukita, M. Koizumi, and T. Someya, "Ultraflexible organic photonic skin," *Science Advances*, vol. 2, no. 4, pp. 1–9, 2016.

[38] H. Lee, E. Kim, Y. Lee, H. Kim, J. Lee, M. Kim, H. J. Yoo, and S. Yoo, "Toward all-day wearable health monitoring: An ultralow-power, reflective organic pulse oximetry sensing patch," *Science Advances*, vol. 4, no. 11, pp. 1–9, 2018.

[39] Y. Khan, D. Han, A. Pierre, J. Ting, X. Wang, C. M. Lochner, G. Bovo, N. Yaacobi-Gross, C. Newsome, R. Wilson, and A. C. Arias, "A flexible organic reflectance oximeter array," *Proceedings of the National Academy of Sciences of the United States of America*, vol. 115, no. 47, pp. E11015–E11024, 2018.

[40] E. L. Ratcliff, P. A. Veneman, A. Simmonds, B. Zacher, D. Huebner, S. S. Saavedra, and N. R. Armstrong, "A Planar, Chip-Based, Dual-Beam Refractometer Using an Integrated Organic Light-Emitting Diode (OLED) Light Source and Organic Photovoltaic (OPV) Detectors," *Analytical Chemistry*, vol. 82, pp. 2734–2742, apr 2010.

[41] C. M. Lochner, Y. Khan, A. Pierre, and A. C. Arias, "All-organic optoelectronic sensor for pulse oximetry," *Nature Communications*, vol. 5, p. 5745, dec 2014.

[42] A. Pais, A. Banerjee, D. Klotzkin, and I. Papautsky, "High-sensitivity, disposable lab-on-a-chip with thin-film organic electronics for fluorescence detection," *Lab on a Chip*, vol. 8, no. 5, p. 794, 2008.

[43] G. Williams, C. Backhouse, and H. Aziz, "Integration of Organic Light Emitting Diodes and Organic Photodetectors for Lab-on-a-Chip Bio-Detection Systems," *Electronics*, vol. 3, pp. 43–75, feb 2014.

[44] E. Manna, T. Xiao, J. Shinar, and R. Shinar, "Organic Photodetectors in Analytical Applications," *Electronics*, vol. 4, pp. 688–722, sep 2015.

[45] F. Lefèvre, A. Chalifour, L. Yu, V. Chodavarapu, P. Juneau, and R. Izquierdo, "Algal fluorescence sensor integrated into a microfluidic chip for water pollutant detection," *Lab Chip*, vol. 12, no. 4, pp. 787–793, 2012.

[46] W. J. Finkenzeller, "The OLED Emitter Ir(btp)2(acac) - Photophysical Properities of the Triplet State Studied by Highly-Resolving Spectroscopy," *Dissertation*, pp. 1–184, 2008.

[47] M. A. Baldo, M. E. Thompson, and S. R. Forrest, "High-efficiency fluorescent organic light-emitting devices using a phosphorescent sensitizer," *Nature*, vol. 403, pp. 750–753, feb 2000.

[48] T. Mori, H. Fujikawa, S. Tokito, and Y. Taga, "Electronic structure of 8-hydroxyquinoline aluminum/LiF/Al interface for organic electroluminescent device studied by ultraviolet photoelectron spectroscopy," *Applied Physics Letters*, vol. 73, pp. 2763–2765, nov 1998.

[49] A. Pradana, *UV nanoimprint lithography for fabrication of 1-D photonic crystal slabs and their application in OLEDs*. PhD thesis, Kiel University, 2014.

[50] S. Z. Hassan, H. J. Cheon, C. Choi, S. Yoon, M. Kang, J. Cho, Y. H. Jang, S.-K. Kwon, D. S. Chung, and Y.-H. Kim, "Molecular Engineering of a Donor/Acceptor Polymer To Realize Single Band Absorption toward a Red-Selective Thin-Film Organic Photodiode," *ACS Applied Materials & Interfaces*, vol. 11, pp. 28106–28114, aug 2019.

[51] S. Sahu and A. J. Pal, "Donor/acceptor type photodetectors: Role of substitution in acceptor material," *Journal of Applied Physics*, vol. 99, jun 2006.

[52] B. Pradhan, A. Bandyopadhyay, and A. J. Pal, "Molecular level control of donor/acceptor heterostructuresin organic photovoltaic devices," *Applied Physics Letters*, vol. 85, pp. 663–665, jul 2004.

[53] V. Pecunia, *Organic Narrowband Photodetectors*. IOP Publishing, dec 2019.

[54] W. J. Tropf, "Temperature-dependent refractive index models for BaF2, CaF2, MgF2, SrF2, LiF, NaF, KCl, ZnS, and ZnSe," *Optical Engineering*, vol. 34, p. 1369, may 1995.

[55] S. Jahns, *Mobile Biosensorik auf Basis optischer Wellenleiter*. PhD thesis, Kiel University, 2016.

[56] L. Landau and E. Lifshitz, "The classical theory of fields," *Butterworth Heinemann*, 1975.

[57] COMSOL, *Ray Optics Users Guide*. COMSOL AB, 2018.

[58] T. Mayr, T. Abel, E. Kraker, S. Koestler, A. Haase, C. Konrad, M. Tscherner, and B. Lamprecht, "An optical sensor array on a flexible substrate with integrated organic opto-electric devices," *Procedia Engineering*, vol. 5, pp. 1005–1008, 2010.

[59] R. Liu, T. Xiao, W. Cui, J. Shinar, and R. Shinar, "Multiple approaches for enhancing all-organic electronics photoluminescent sensors: Simultaneous oxygen and pH monitoring," *Analytica Chimica Acta*, vol. 778, pp. 70–78, 2013.

[60] C. Lian, D. Young, R. E. Randall, and I. D. W. Samuel, "Organic Light-Emitting Diode Based Fluorescence-Linked Immunosorbent Assay for SARS-CoV-2 Antibody Detection," *Biosensors*, vol. 12, p. 1125, dec 2022.

[61] M. Czugala, C. Fay, N. E. O'Connor, B. Corcoran, F. Benito-Lopez, and D. Diamond, "Portable integrated microfluidic analytical platform for the monitoring and detection of nitrite," *Talanta*, vol. 116, pp. 997–1004, 2013.

[62] A. M. Nightingale, S.-u. Hassan, B. M. Warren, K. Makris, G. W. H. Evans, E. Papadopoulou, S. Coleman, and X. Niu, "A Droplet Microfluidic-Based Sensor for Simultaneous in Situ Monitoring of Nitrate and Nitrite in Natural Waters," *Environmental Science & Technology*, vol. 53, pp. 9677–9685, aug 2019.

[63] I. Titov, M. Köpke, N. C. Schneidewind, J. Buhl, Y. Murat, and M. Gerken, "OLED-OPD Matrix for Sensing on a Single Flexible Substrate," *IEEE Sensors Journal*, vol. 20, pp. 7540–7547, jul 2020.

[64] S. Balslev, A. M. Jorgensen, B. Bilenberg, K. B. Mogensen, D. Snakenborg, O. Geschke, J. P. Kutter, and A. Kristensen, "Lab-on-a-chip with integrated optical transducers," *Lab Chip*, vol. 6, no. 2, pp. 213–217, 2006.

[65] A. Llobera, S. Demming, R. Wilke, and S. Büttgenbach, "Multiple internal reflection poly(dimethylsiloxane) systems for optical sensing," *Lab on a Chip*, vol. 7, no. 11, p. 1560, 2007.

[66] I. Titov, M. Köpke, and M. Gerken, "Monolithic Integrated OLED-OPD Unit for Point-of-Need Nitrate Sensing," *Optical Sensors and Sensing Congress 2022 (AIS, LACSEA, Sensors, ES)*, vol. 1, p. EW1G.1, 2022.

[67] A. W. Warrick, *Soil Water Dynamics*. Oxford University Press, feb 2003.

[68] S. Böckmann, I. Titov, and M. Gerken, "Extraction of Soil Solution into a Microfluidic Chip," *AgriEngineering*, 2021.

[69] Z. Liu, M. G. Helander, Z. Wang, and Z. Lu, "Band alignment at anode/organic interfaces for highly efficient simplified blue-emitting organic light-emitting diodes," *Journal of Physical Chemistry C*, vol. 114, no. 39, pp. 16746–16749, 2010.